The 5th UK & RI Postgraduate Conference in Biomedical Engineering & Medical Physics

12-14 July 2009
University of Oxford

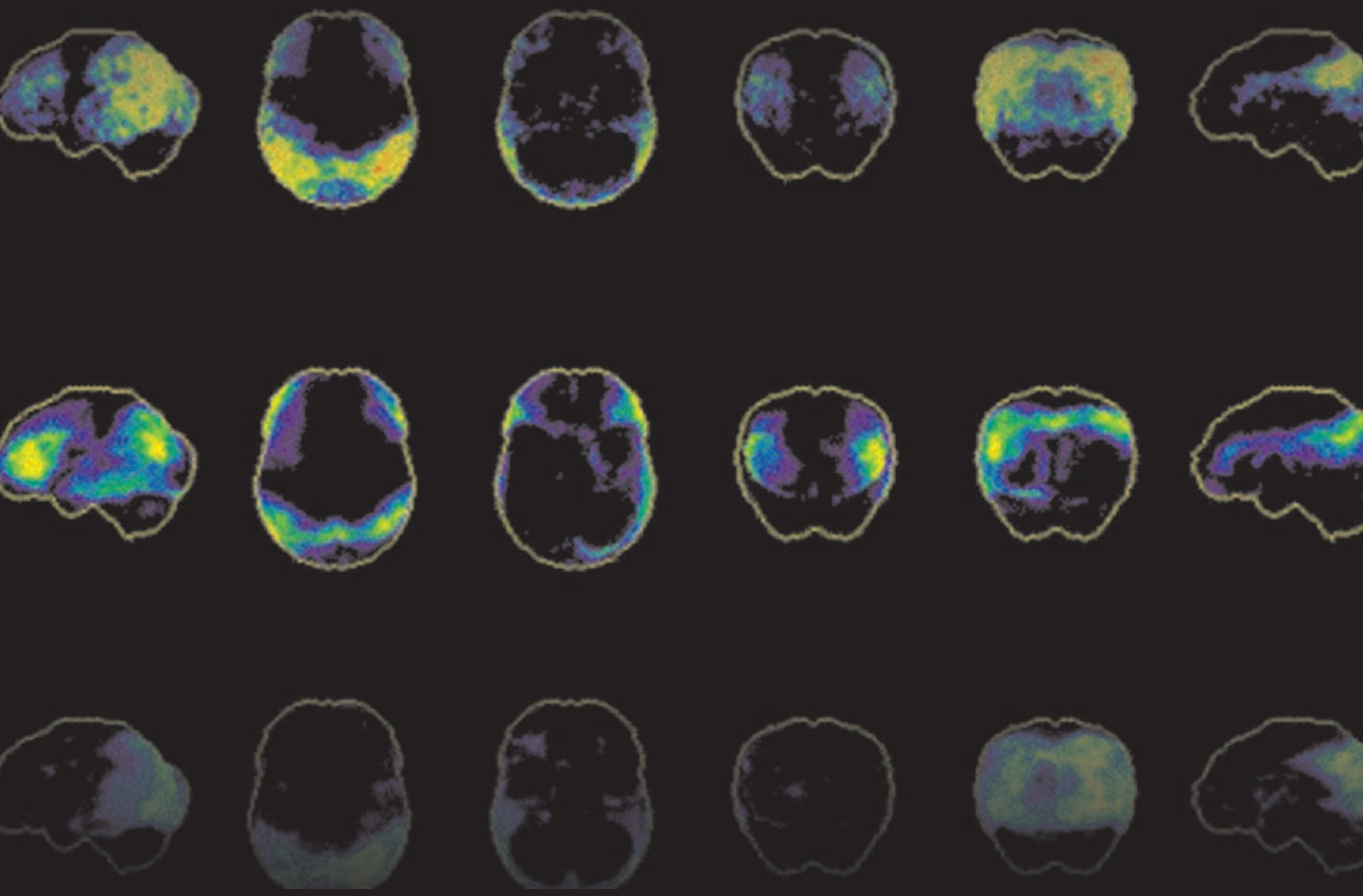

PGBIOMED
biomedical engineers for tomorrow

IEEE
UNIVERSITY OF Southampton
Professional Engineering Publishing
IET
UNIVERSITY OF OXFORD

THIS PAGE INTENTIONALLY LEFT BLANK

Proceedings of the

5th UK & Republic of Ireland Postgraduate Conference in Biomedical Engineering and Medical Physics

PGBIOMED09

12 – 14 July 2009

University of Oxford

Editors: Christopher J. James, Charmaine Demanuele and Aida Jimenez-Gonzalez

ORGANISING COMMITTEE

Dr Christopher J. James
IEEE EMBS UK & RI Chapter Chair
Institute of Sound & Vibration Research
University of Southampton

Charmaine Demanuele
EMBS UK & RI Student Club Chair
Institute of Sound & Vibration Research
University of Southampton

Dr David Clifton
Department of Engineering Science
University of Oxford

David Wong
Webmaster
Department of Engineering Science
University of Oxford

Aida Jimenez-Gonzalez
Institute of Sound & Vibration Research
University of Southampton
Universidad Autonoma Metropolitana-Iztapalapa

Edited by Christopher J. James, Charmaine Demanuele and Aida Jimenez-Gonzalez

FOREWORD

Welcome to PGBIOMED 2009, the 5th postgraduate biomedical engineering and medical physics event in the UK and Republic of Ireland. Building on past success we are very happy to be organising another similar event again this year. The fundamental scope of this meeting is to allow us, postgraduate students, to meet, exchange ideas and learn more about the fields of biomedical engineering, medical physics and other related areas of knowledge. We acknowledge that as students, it is important to be aware of other work being undertaken in this rapidly expanding area of research, and to interact with tomorrow's leading specialists. This is made possible by the wide range of subjects represented in the papers submitted for the conference this year, which are being presented by students from different universities within the UK and RI. As a conference organised *for the students by the students*, we aim to provide a relaxed and friendly environment for you to present in. This year we are within the august surroundings of Magdalen College, Oxford. We hope that this venue inspires as well as provides us all with a good opportunity to interact and enjoy these few days together.

We are very pleased to welcome Prof Ron Summers from the University of Loughborough and Dr Richard Scott from Sherwood Forest Hospitals NHS Foundation Trust, each of whom will give an invited presentation. Both have a wide experience in biomedical engineering and medical physics and will bring practical insights into the work they have undertaken.

Presenting research work and ideas is crucial for students both during university life and beyond. Dr Christopher James from the University of Southampton is also running a seminar filled with useful tips on this important aspect of disseminating our work.

We are very grateful to all our sponsors for their generosity: Professional Engineering Publishing, the IEEE EMBS UK and RI chapter and IEEE EMBS, the IET Healthcare Professional Network and personal donations from Prof Lionel Tarassenko, Oxford and Dr Christopher James, Southampton. The help and support given by the reviewers was also essential and is also acknowledged. I am grateful to the committee who has worked tirelessly to make this event enjoyable by all concerned.

Thanks also to the University of Southampton and the University of Oxford in their support of our team and in giving us the encouragement for this event to happen.

I hope that you will enjoy this conference and find it a useful, refreshing and inspiring experience.

Charmaine Demanuele
IEEE UKRI EMBS Student Club Chair

GUEST SPEAKER

Prof. Ron Summers: From Disruption to Innovation
University of Loghborough

Disruptive technologies are those that enter the market that have, over time, an opportunity to displace the technologies of the market leaders. The criterion used usually is by cost, even though performance of the disruptive technology might not be as good as those that exist. Emerging health technologies that have the potential to be disruptive will be identified, and as an example applications of XML-mediated open source software will be used as a case study. Messages taken from the disruptive process will be discussed in terms of its impact and value on the innovation cycle.

Ron Summers is Professor of Information Engineering at Loughborough University where he is Executive Director of the Systems Programmes within the Department of Electronic and Electrical Engineering. He is a past-Vice President (two terms) of the IEEE Engineering in Medicine and Biology Society, and immediate Past-President of the Institute of Measurement and Control.

Ron is a Director of two spin-out companies that deliver solutions to the health technologies market; although it is his experience with his company that has failed that enables him to provide anecdotes for his talk in this event. Learning from failure has been most instructive. One good thing to emerge from the sad experience is the creation of many small companies, formed by ex-colleagues coming together in a self-organised way to deliver products and services for numerous sectors.

GUEST SPEAKER

Dr Richard Scott: “Engineering Health” – A career in the Modern NHS Sherwood Forest Hospitals NHS Foundation Trust

Biomedical Engineers have, and will continue, to make significant contributions to the health of the population through research and design activities associated with medical devices. Additionally, as the complexity and quantity of medical devices increase in the evolving healthcare setting, Engineers can play a crucial role in risk minimisation and optimisation of patient safety by ensuring the effective management of these devices. Indeed, the current Department of Health project “Modernising Scientific Careers” is aimed at reframing the training and career structure for Engineers working in the National Health Service, (NHS). With reference to his own career the speaker will give an overview of the modern NHS and Engineering careers in it, together with an introduction to work underway with Modernising Scientific Careers.Specifically, a research project assessing the mechanics of the respiratory system will be described, together with a range of typical activities an Engineer may contribute to in a Medical Physics Service. The principles behind the management of medical devices in the NHS will be explained, as an example of a professional area the Engineer may choose to specialise in. Finally, examples will be given of the role of the Engineer in contributing to management activities within a Hospital setting. The aim is to give an insight into the work of the “Clinical Engineer” and potential career progression within the Health Service. Throughout the talk there will be practical tips on personal and professional development to aid career advancement.

Having taken a first degree in Electronic Engineering, which included an industrial placement in the Division of Anaesthesia at the Clinical Research Centre, Harrow, Richard started work in 1984 as an Electronics Design Engineer in the Medical Physics Department at the Royal United Hospital, Bath. Richard subsequently gained a Masters Degree in Medical Electronics & Physics and undertook a part-time PhD researching into the mechanics of the respiratory system whilst working through the ranks of the Medical Physics profession. In 1995 Richard moved to his current post at King’s Mill Hospital, Nottinghamshire as a Consultant Medical Physicist and Head of the Medical Equipment Management Department. Richard’s expertise is in biomedical signal processing, medical devices and their management and he is involved in the development of national and international standards for medical devices. Working in a busy District General Hospital Richard has considerable experience of the NHS and its management.

An active member of the IET, he is past chair of the Healthcare Technologies Professional Network and a current member of the Executive Team. Registered with the Health Professions Council as a Clinical Scientist Richard is keen to see the Medical Physics & Clinical Engineering profession continue to develop and is currently an advisor to NHS East Midlands and contributing to the Department of Health Modernising Scientific Careers programme.

CONTENTS

Page No. Platform Session 1.1

Poster Session 1

Platform Session 1.2

Platform Session 1.3

Platform Session 2.1

Platform Session 2.2

Poster Session 2

Platform Session 2.3

LIST OF AUTHORS

PERSONALISED AMBIENT MONITORING: WIRELESS CAMERAS FOR ACTIVITY DETECTION

J.D. Amor and C.J. James[1]

[1]Signal Processing and Control Group, ISVR, University of Southampton, Southampton, UK
ja@isvr.soton.ac.uk,

Abstract – A wireless network camera is being used in the PAM project to monitor activity in the home environment. Images are processed to extract 'blobs' of activity in the scene, which are then checked for intersection with areas of interest. We describe the hardware set-up and the processing algorithms used and present some preliminary results.

I. INTRODUCTION

Bipolar disorder (BD) is a severe mental disorder characterised by recurring episodes of mania and depression. It is estimated that BD affects between 0.4–1.6% of the population [1]. Many BD sufferers monitor their condition, keeping records of their activity, to identify the onset of an affective episode so that they can take steps to lessen and counteract the severity of the episode [2].

The Personalised Ambient Monitoring (PAM) project aims to develop a system to help patients self-monitor their condition and to predict their mental health trajectory. Using a network of personalised, discreet sensors the patient's activity and behavioural patterns will be detected. These will be used to derive a 'normal' pattern of behaviour, which will be monitored for changes that indicate the onset of an affective episode.

Both the patient and their home environment will be monitored. There is difficulty however, in effectively monitoring some rooms in a patient's home, such as a kitchen, where there are many areas of interest (AOIs) that need to be monitored. The traditional approach to monitoring each AOI would involve a number of different sensors each tailored to a specific task and each requiring separate wired or wireless communication links; the system becomes very complicated very quickly.

An alternative solution is to use a wireless camera, with a wide-angle lens, to take images of the room and to process these images to extract activity in the AOIs and it is this approach that is being taken with the PAM project. This paper discusses the hardware set-up and processing algorithms that have been developed so far. Some preliminary results are also presented.

II. METHOD

A . Hardware Set-up

The camera being used for the PAM project is an Edimax IC-1520DPg with a 179° horizontal and 129° vertical field of view [3]. The camera is mounted as high in the room as possible to get a birds-eye view as this minimises the problems involved in objects passing in front of the camera and causing false activity to be registered.

The camera is connected through a secured *ad-hoc* wireless link to a base-station PC and uploads a snapshot of the room every 10 seconds.

B. Image Processing

The images that are provided by the camera are processed in sequence to extract areas of movement from the background in the scene. The idea is to render an image into 'blobs', which are a black and white representation of the scene with the white blobs showing areas of activity. Before the images are processed, AOIs are defined so that activity can be correctly identified. The image processing follows the following steps:

1. Background estimation with a temporal median of several images.
2. Background subtraction / change detection using either the Wronskian change detector or an in-house developed algorithm.
3. Activity detection within pre-defined areas of interest.

The image processing algorithms are used to detect things in an image that are different to the background image that has been derived from the preceding sequence.

The Wronskian change detection model (WM) is based on the idea of linear independence [4]. Each pixel in the image is represented as a vector comprised of itself and its neighbouring pixels. If two corresponding vectors from two separate images are linearly dependent then there has been no physical change in the scene.

The in-house (IH) algorithm is based on a simple pixel difference. Two images are differenced and where a difference is recorded a physical change in the scene is assumed to

have taken place. The resultant image is median filtered to remove speckle noise and then Gaussian filtered to blur the image and produce strong blob responses where activity has occurred.
Activity detection is performed by examining each AOI. If a sufficient number of pixels in an AOI are white (i.e. indicate a change in the scene) then an activity is recorded.

III. RESULTS

Figure 1 shows a living room in which the camera has been mounted in one corner of the room. AOIs have been marked in the image over the sofa, the patio door and a chair.
Figure 2(a) shows the result of applying the WM algorithm to the image sequence and figure 2(b) shows the result of applying the IH algorithm. The author has been clearly been identified in both images and would cause an event to be registered in the AOI set on the sofa. The IH algorithm is significantly less noisy, in terms of speckle noise, than the WM due to the filtering applied after the image differencing.

Figure 1. A camera image before processing with some AOIs marked in red.

(a) (b)

Figure 2. The same image after processing with the WM algorithm (a) and the IH algorithm (b). The presence of the author has been clearly detected by both algorithms.

Figure 3 shows a section of the image sequence where the author sits down in an empty room. The IH processed blob images are also shown. The sequence shows that the author is successfully extracted from the background in a sequence of images.

Figure 3. Five frames of the original image sequence, showing the empty room followed by the authors presence, and the blobbed images achieved with the IH algorithm.

IV. DISCUSSION

The results shown above show that changes can be detected in an image and that this detection can be used to identify activity in areas of interest in the image. Two image processing algorithms have been tested, the WM and the IH. Both algorithms successfully extract activity in AOIs but differ in their responses to lighting changes. A lighting change in the scene, either global (e.g. ambient light change) or local (e.g. reflections) can cause false changes to be registered. The IH algorithm is particularly susceptible to this; since it is based on simple pixel differences any change in light will be registered as changes in the scene. The filtering applied to the image goes some way towards eliminating this noise but does not achieve prefect results. The WM is significantly better in terms of lighting noise reduction as each pixel is considered in relation to its neighbours. This leads to less lighting induced noise but can cause the resultant blobs to be less coherent, as seen in figure 2 (a).

V. CONCLUSION

The camera and blob detection image analysis approach is still a work in progress. Promising results have been achieved so far and the approach seems to be viable as a way of monitoring a complex environment. Further improvements to the image processing algorithms are required before the approach can be fully integrated into the PAM system.

REFERENCES

[1] American Psychiatric Association. *DSM-IV-TR - Diagnostic and Statistical Manual of Mental Disorders*. American Psychiatric Publishing, Inc., Washington, DC, 4th - text revision edition, 2000.
[2] Sarah J. Russell and Jan L. Browne. *Staying well with bipolar disorder*. Aust N Z J Psychiatry, 39(3):187–193, March 2005.
[3] Edimax IC-1520DPg Digital Pan / Tilt Wireless Network Camera, last accessed on 13/03/2009 at: http://www.edimax.co.uk/en/produce_detail.php?pd_id=236&pl1_id=1&pl2_id=7
[4] Durucan, E., and Ebrahimi T., *Change Detection and Background Extraction by Linear Algebra*, in Proceedings of the IEEE, 89(10):1368–1381, October 2001.

COMPUTATIONAL MODELS OF THE EFFECT OF DEEP BRAIN STIMULATION ON NEURONAL STRUCTURES

N. Yousif [1], N. Purswani [2], X. Liu[1-3]

[1] Department of Clinical Neuroscience, Imperial College London, London, W6 8RP, U.K.
[2] Department of Bioengineering, Imperial College London, London, SW7 2AZ, U.K.
[3]The Movement Disorders and Neurostimulation Unit, Charing Cross Hospital, London, W6 8RF, U.K.

n.yousif@imperial.ac.uk

Abstract - Deep brain stimulation (DBS) has become an increasingly used clinical therapy for several neurological conditions. However, it is currently impossible to directly measure the distribution of the stimulus in the patient's brain surrounding the implanted electrode. Computational models in the form of finite element models coupled to axon cable models have proved useful for visualizing stimulation effects. The use of such unconnected axon models, however, relies on the assumption that the excitation of fibres is the functional effect of DBS. We propose that quantifying the region of tissue activated (RTA) using whole neuron models can provide further clues about the mechanism of DBS.

I. INTRODUCTION

Deep brain stimulation involves inducing local changes in the activity of the surrounding neurons via extracellular stimulation using electrical pulses, by the surgical insertion of an electrical pacemaker into a target region of the patient's brain. It is a reversible neuromodulatory technique, commonly used to treat movement disorders. This study focuses on DBS for the treatment of Parkinson's disease (PD).

High frequency stimulation of the subthalamic nucleus (STN) has been proven to offer therapeutic effects by reducing tremor and associated involuntary contractions in PD patients [1]. The mechanism behind DBS is not well understood, although there are several hypotheses. For example, some studies suggest that DBS silences the pathological activity of STN neurons and this contributes to the therapeutic benefits observed [2]. There are also hypotheses regarding the pathological interaction between different neural targets within the basal ganglia [3].

Computational studies also address this question, but so far base their assumptions on calculating the RTA by observing the activity of unconnected axon models [4]. We propose a different approach to calculate the RTA utilising neuronal models that are more consistent with the anatomy of the target region.

II. METHODS

We used results from a finite element electric field model [5-7] which provided the extracellular potential as a stimulus for a range of multicompartment models, starting with myelinated axons [4] and followed by the subthalamic projection neurons of increasing complexity [8].

Multicompartment models of neurons were created utilising the NEURON simulation environment [9].

A. Multicompartment model of a mammalian axon

Axons have been shown to be the most excitable elements during DBS, and several studies have simplified neurons to consider only the axonal elements [4].

For the first part of the study, an existing model of an axon with 21 compartments was created and 100 of these axons were placed in a configuration similar to the one shown below (Figure 1B).

A

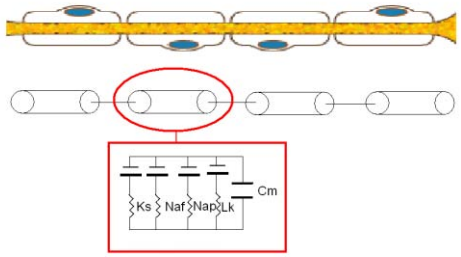

B

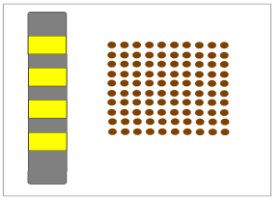

Figure 1: A. An illustration of an axon and a simplified multicompartment equivalent circuit. Each section is modelled as a set of cylinders. Each cylinder contains conductances that define the properties of the neuron model at that particular point.
B. A representation of 100 axons in a 10x10 mesh placed perpendicular to the DBS stimulation electrode (left)

B. Multicompartment model of a subthalamic projection neuron

The STN is the region of the brain most commonly stimulated during treatment of PD [1-2]. The arrangement (Figure 1B) was also used for the case of a population of 100 STN projection neurons and observed dynamic behaviour was approximated and included in the models [8]. The morphology of the projection neurons in this model was simplified to reduce the required computation, details of the model can be found in [10].

III. RESULTS AND DISCUSSION

Both models were implemented in the arrangement shown in Figure 1B, and the region of tissue activated was quantified. The contour plots in figure 2 represent the RTA by showing the number of action potentials fired by the neurons as a function of distance from the stimulating electrode (x-axis) and along the electrode (y-axis).

A

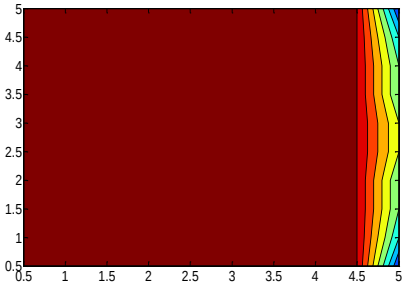

B

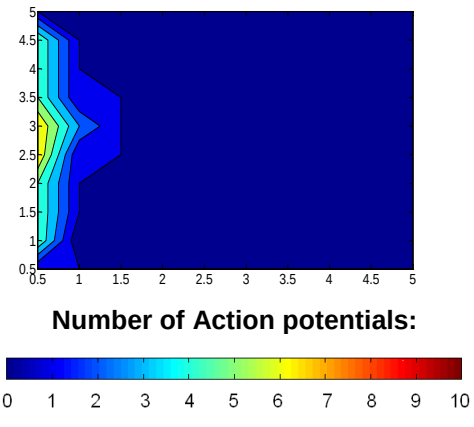

Figure 2: Contour plots to illustrate the number of action potentials fired by the neuronal elements after high frequency stimulation for 100ms (The stimulus obtained from finite element model). The horizontal and vertical axes represent the distance (mm) from the stimulation electrode.
A. Number of action potentials fired by model axons
B. Number of action potentials fired by model STN neurons.

The results show that under the same stimulation conditions (monopolar and cathodic at 1V, 100Hz, 500µs pulse width), axonal elements produce action potentials in a 1:1 ratio with the stimulus pulses (10 action potentials in 100ms) up to 5mm away from the electrode.

In the case of the STN neurons, we can see that at distances greater than 1.5mm from the electrode the model neurons do not fire at all. None of the STN neurons fired at the stimulus frequency, and the maximum number of action potentials was 6 in 100ms. Consequently, the RTA is smaller.

These results indicate that the therapeutic action of DBS cannot be explained wholly by the effect on axonal firing.

IV. CONCLUSION

In agreement with previous work [3-4], the prediction of the RTA using cable models of unconnected axons and defining activation as generating action potentials in a 1:1 ratio with the stimulus frequency, provides a convenient way of comparing stimulation parameters. However, the responses of the subthalamic projection neurons, with more complex morphologies and membrane dynamics provide more detailed information about the possible mechanisms underlying the observed improvement in patients' symptoms.

Further work on the subthalamic models will include the addition of synaptic connections between neurons and the inclusion of more detailed morphologies and ion channels.

REFERENCES

[1] Benabid AL, Chabardes S , *Deep brain stimulation of the subthalamic nucleus for the treatment of Parkinson's disease*. Lancet Neurol 2009 Jan;8(1):67-81.

[2] Magariños-Ascone C, Pazo JH, Macadar O, Buño W, *High-frequency stimulation of the subthalamic nucleus silences subthalamic neurons: a possible cellular mechanism in Parkinson's disease*. Neuroscience. 2002;115(4):1109-17.

[3] McIntyre C.C, Warren M. Grill, et al, *Cellular Effects of Deep Brain Stimulation: Model Based Analysis of Activation and Inhibition.* J Neurophysiol 91: 1457-1469, 2004

[4] Butson, C.R, and McIntyre C.C, *Tissue and electrode capacitance reduce neural activation volumes during deep brain stimulation*. Clinical Neurophysiology 2005 1-11

[5] Yousif, N et al., *The perielectrode space is a significant element of the electrode-brain interface in deep brain stimulation: A computational study*. Brain Res Bull. 2007 October 19; 74(5): 361–368.

[6] Yousif, N, Bayford R, Wang S, Liu X, *Quantifying the effects of the electrode-brain interface on the crossing electric currents in deep brain recording and stimulation.*Neuroscience 2008 152(3):683-91

[7] Yousif N, Bayford R, Wang S, Liu X, *The influence of reactivity of the electrode-brain interface on the crossing electric currents in deep brain recording and stimulation.* Neuroscience 2008 152(3):597-606

[8] Gillies, A, Willshaw,D, *Membrane Channel Interactions Underlying Rat Subthalamic Projection Neuron Rhythmic and Bursting Activity.* J Neurophysiol 95: 2352-2365, 2006.

[9] Carnevale and Hines, NEURON yale: http://www.neuron.yale.edu/neuron/

[10] Gillies, A, *The role of the subthalamic nucleus in the basal ganglia*, PhD thesis Ch6-7. 1995, University of Edinburgh.

ERP CLASSIFICATION USING EMPIRICAL MODE DECOMPOSITION

N. Williams[1], I. Daly[2], S. J. Nasuto[2], D. Saddy[1], K. Warwick[2]

[1] School of Psychology and Clinical Language Sciences, University of Reading, Reading, UK
[2]CIRG, School of Systems Engineering, University of Reading, Reading, UK

sir07nw@reading.ac.uk,

Abstract – Empirical Mode Decomposition (EMD) is applied to the problem of ERP classification for BCI. Artificial ERPs are created using a Neural Mass model assuming the additive model of ERP generation at different SNRs. Features are extracted from an EMD-based reconstruction and a Support Vector machine is applied to classify the ERPs. The classification method produced classification accuracies significantly better than chance for SNRs between 0 dB and -20 dB. Further, the EMD-based method produced significantly better classification than the conventional averaging method for SNR of -5 dB, -10 dB and -15 dB.

I. INTRODUCTION

Event Related Potentials (ERPs) are changes in electro-potentials across the scalp closely correlated to the occurrence of specific events [1]. They are commonly used in many areas of Neuroscience research [1] and Brain Computer Interfacing (BCIs) .

BCIs provide an alternative means for control of a computer by bypassing the peripheral nervous system. Unlike traditional methods of computer control, a BCI allows the user to control a computer via electroencephalographic signals .

Accurate classification of ERPs is of key importance in goal orientated BCI research (a control paradigm where the user is presented with only a discrete set of options [2]) and other areas of Neuroscience [1]. To accurately detect ERPs it is necessary to extract features that best describe ERPs in the Electroencephalogram (EEG).

The ERP is embedded in background EEG of high variance resulting in Signal-to-Noise Ratio (SNR) between 0 dB and -20 dB [7], making ERP detection non-trivial.

We test performance of a classification method based on Empirical Mode Decomposition (EMD) at different SNRs. Section II introduces EMD, section III details procedures used to compare EMD-based classification with one based on conventional averaging. Section IV presents the results of this investigation before a discussion of the meaning of these results in section V.

II. EMPIRICAL MODE DECOMPOSITION

EMD decomposes a signal into a set of Intrinsic Mode Functions (IMFs) and a residual component. It is an adaptive method in that it decomposes a time series according to time scales intrinsic to the data [5].

An IMF satisfies the following two criteria:

i. Number of extrema and number of zero-crossings differ at most by one – eliminates riding waves

ii. The mean of the upper and lower envelopes equals zero – ensures that instantaneous frequency will not have unwanted fluctuations due to asymmetric waveforms

The IMF identified according to these criteria is subtracted from the original signal and the process is repeated on the residual until an IMF cannot be found in the residual [5].

III. METHODS

Since we wanted to investigate performance of the EMD-based method at different SNRs, a Neural Mass model is constructed to generate artificial EEG signals with a realistic power spectrum [3].

Using the simulated data, ERPs are created assuming the additive model of ERP generation [6] whereby ERPs arise from an additive signal component evoked by the stimulus.

$$X_t = S_t + E_t, \quad t = 1,...,N$$

where X_t is the single-trial EEG containing ERP, S_t is the background EEG generated from the Neural Mass model and E_t is our additive ERP component.

The additive component is chosen to resemble a P300, a standard ERP elicited by a rare stimulus in an oddball paradigm. Thus, it is a curve approximated by a Gaussian function centred at 300ms [4]. A gain is used to scale the amplitude of this additive component and thus generate ERPs at different SNRs. A typical example of an ERP generated in this way is shown in Figure I.

Figure I
Typical artificial ERP at SNR of -5dB (1,000Hz sampling)

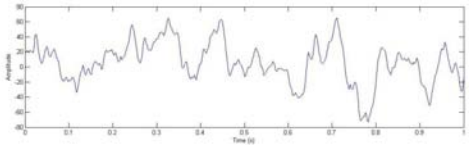

To train and test the classifier, two datasets are created, each with 1000 trials, half of which contain the ERP component.

Following the goal orientated BCI paradigm, groups of 2 trials corresponding to 'ERP present' and 2 trials corresponding to 'ERP absent' conditions are averaged. Thus the data sets now contain 500 averages of which 250 contain ERPs and 250 are averages of background EEG.

To these averaged trials EMD is applied. Based on manual inspection, two IMFs containing the lowest frequencies and the residual are chosen to be summed to obtain a reconstruction, from which features are extracted.

The EMD-based reconstructions are compared to the averages of 2 raw EEG trials.

Smoothed amplitude features [2] are taken from each averaged trial both with and without EMD applied. Averaged amplitude is calculated from the trials across times 150ms to 250ms, 250ms to 350ms and 350ms to 450ms. Thus each trial can be described by three features.

A Support Vector Machine (SVM) [2] is trained on these features in the training set. The classification performance is tested on the verification set and presented as a function of the SNR.

IV. RESULTS

As observed in Table 1, statistically significant accuracies ($P < 0.001$) are achieved for SNRs from 0 dB to -20dB with both EMD-based method and conventional averaging method, compared to chance ($p=0.5$). As per standard BCI paradigm, the cumulative binomial distribution gives likelihood of a given percentage of correct classifications. Further, the EMD-based method outperforms the conventional averaging method by a statistically significant margin at -5 dB ($P<0.001$), -10 dB ($P<0.001$) and -15 dB ($P<0.05$).

TABLE I
Classification accuracies as a function of SNR

SNR (dB)	With EMD	Without EMD	P-value of difference
0	0.99(P<0.001)	0.99(P<0.001)	P=0.19
-5	0.94(P<0.001)	0.91(P<0.001)	P<0.001
-10	0.82(P<0.001)	0.78(P<0.001)	P<0.001
-15	0.7(P<0.001)	0.66(P<0.001)	P<0.05
-20	0.61(P<0.001)	0.58(P<0.001)	P=0.07

V. DISCUSSION

The classification accuracies achieved by the EMD-based method is significantly better than the conventional averaging method at SNRs of – 5dB, -10 dB and -15 dB. Thus, EMD allows for noise reduction of the average of 2 trials, making the features more sensitive to presence of an ERP component. Also, the results suggest the P300 component was confined to the two IMFs with the lowest frequencies and the residual.

The ability of EMD to distinguish between the presence and absence of an ERP is of direct significance to goal orientated BCIs. Applications of which are operated by accurately detecting the P300 component.

In our analysis, the trials containing an ERP component were generated assuming the additive model. The last two IMFs and residual were chosen for reconstruction based on manual inspection. This is a potential weakness of our method. However, inspection of the average of EMD-denoised trials were found to closely resemble average of raw trials, suggesting that this method was reducing background EEG and retaining ERP. Future work will look at selecting IMFs for automatic reconstruction. We will also be exploring alternative features for classification and the possibility of single-trial classification.

VI. CONCLUSION

The ability of EMD to detect the presence of an ERP is demonstrated. The accuracy of the classification was significantly better than obtained by conventional averaging. Thus, the EMD-based approach represents a potential alternative to classification of ERPs in general and for application to P300 detection in BCI applications in particular.

REFERENCES

[1] Rugg, M.D., Coles, M.G.H., "Electrophysiology of mind. Event-related potentials and cognition", 2002, "Oxford Psychology series"

[2] Lotte,F, Congedo,M, L´ecuyer, A., Lamarche, F., Arnaldi, B., "A review of classification algorithms for EEG-based brain–computer interfaces", Journal of Neural Engineering, V4, 2, 2007

[3] David,O., Friston, K.J.,"A neural mass model for MEG/EEG: coupling and neuronal dynamics", NeuroImage, V20, 1743-1755, 2003

[4] Graimann, B., "P300", http://www.bci-info.tugraz.at/Members/graimann/definitions/P300, Accessed on: 11/02/2009, Written: 2005

[5] Huang, N. E., Shen, Z., Long, S. R., et al., "The empirical mode decomposition and the Hilbert spectrum for nonlinear and non-stationary time series analysis," *Proceedings of the Royal Society of London* , vol. 454, no. 1971, pp. 903–995, 1998.

[6] Ankoor S. Shah et. al., "Neural dynamics and the fundamental mechanisms of event-related brain potentials", Cerebral cortex, V14, 476-483, 2004

[7] Rubin, D. D. B. D., Baselli, G., Inbar, G. F. and Cerutti, S., "An adaptive neuro-fuzzy method for estimating single-trial movement-related potentials," *Biol. Cybern.*, vol. 113, pp. 63–75, 2002.

ON THE ANALYSIS OF FOETAL HEART SOUND MORPHOLOGY AFTER DE-NOISING THE ABDOMINAL PHONOGRAM

A. Jiménez-González[1,2] and C. J. James[1]

[1]Institute of Sound and Vibration Research, University of Southampton, Southampton, UK
[2]Electrical Engineering Department, Universidad Autónoma Metropolitana-Iztapalapa, México City, México

aj11v07@soton.ac.uk

Abstract - This work extracted time and frequency information of foetal heart sounds after de-noising the abdominal phonogram. In this preliminary analysis, in two of three subjects, distinctive and consistent morphologies were detected from averaged values of heart sounds S1 and S2. However, the FFT spectra of S1 and S2 were completely overlapped. Further time-frequency analysis on more subjects will provide more specific features that might be correlated with foetal heart function and, consequently, foetal well-being.

I. INTRODUCTION

Monitoring foetal heart activity is an effective tool for detecting foetal well-being. It can be non-invasively achieved by placing a passive sensor on the maternal abdomen to record the foetal heart sounds (FHS) [1]. From the noisy recorded signal (called the abdominal phonogram), after a de-noising procedure by single-channel Independent Component Analysis (SCICA), it is possible to extract the FHS (S1 and S2) [2]. Next, by performing further analysis of S1 and S2, it is suitable to obtain their time and frequency features, which reflect the status of the foetal heart valves during the heart cycle. This work preliminary explored the morphology and frequency spectrum as the features to be obtained from S1 and S2 (extracted from de-noised abdominal phonograms) to study the foetal heart valves.

II. METHODS

For this work, three abdominal phonograms (sampled at 500 Hz and 3-5 minutes in length) were used. The signals were processed as follows:

A. Adaptive de-noising

Each abdominal phonogram was de-noised by using an implementation of Single-Channel ICA (SCICA) that takes into account the rich temporal structure of the signal. In this way, SCICA performed a data dependent analysis to learn zero-phase filter banks that were suitable to adaptively de-noise the abdominal phonogram in order to extract the FHS [2].

B. Foetal heart sound analysis

To look for the morphology and frequency spectrum of the FHS, averaged values of S1 (aS1) and S2 (aS2) were calculated over time. To do this, the de-noised signal was segmented in overlapped blocks of data; each block was 10 s long (containing about 25 FHS), and 50 % overlapped. From each block (whenever possible), every S1 and S2 was manually selected and cut using a fixed window. The window, containing the entire heart sound (either S1 or S2), was centred on its maximum peak. Next, the cut heart sounds were averaged to calculate aS1 and aS2. This procedure was repeated for every block in the de-noised signal and, as a result, for every subject, a number of aS1s and aS2s, along with their corresponding FFT spectra, were obtained.

III. RESULTS

Figure 1 depicts the time and frequency FHS features obtained from subjects 1 and 3 after de-noising the abdominal phonogram. The noisy abdominal phonogram is shown in the first row. The second row depicts the de-noised signal containing two S1-S2 couples, along with the window used to extract each heart sound. The third and fourth rows illustrate, respectively, couples of aS1s and aS2s extracted from non-consecutive blocks. Such blocks, picked up earlier and close to the end of the de-noised signal, were distant from each other by at least 100 s.

From the abdominal phonograms, in both time and frequency domains, high levels of noise are visible, which makes it very hard to distinguish the FHS. After the SCICA de-noising procedure, the resulting signal clearly shows the main FHS – S1 and S2 – whose combined frequency spectra range from 15 to 50 Hz [2].

Regarding the morphology of S1 and S2, these preliminary results show that, respectively, two distinctive morphologies persisted over time and, apparently, over subjects. Also, as for the adult case, S1 lasts longer than S2. The spectra of both FHS consistently showed a large peak between 30 and 40 Hz and, in some blocks of data, a second peak close to 45 Hz was also present. Furthermore, the bandwidth of S2 seems to be wider than the bandwidth of S1.

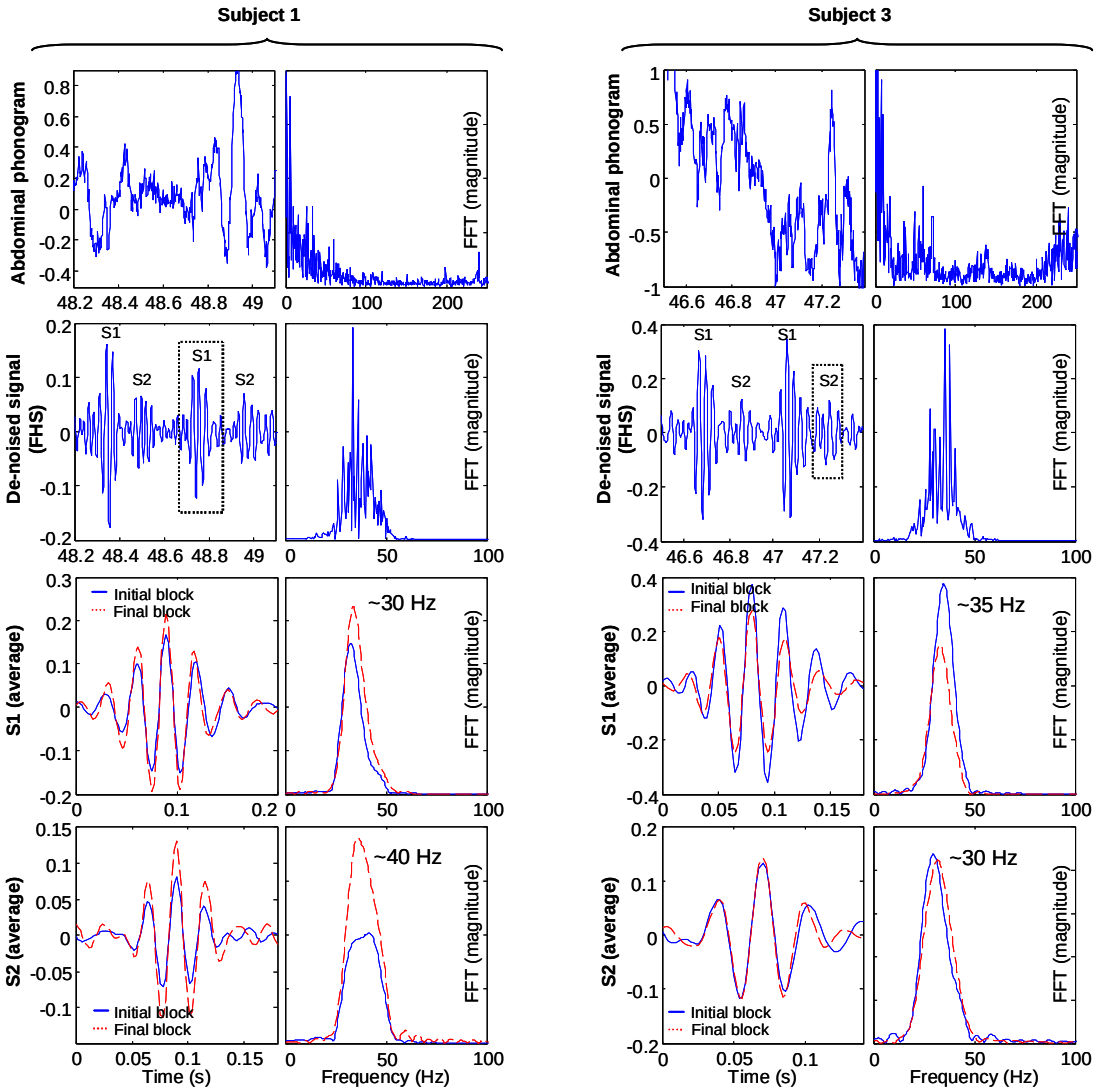

Figure 1. Morphology and frequency spectrum of foetal heart sounds from two subjects (left and right). From top to bottom: the noisy abdominal phonogram, the de-noised signal showing the FHS, a couple of averaged S1s, and a couple of averaged S2s.

IV. DISCUSSION AND CONCLUSION

This work has been focused on the analysis of FHS after de-noising the abdominal phonogram using SCICA. Using blocks of data to obtain averaged values of S1 and S2, this preliminary analysis seems to show not only distinctive but also consistent temporal morphologies in two of three subjects. In the frequency domain, however, although the spectra of both FHS are band-limited, they completely overlap, which makes it difficult to establish any difference between S1 and S2. Further time-frequency analysis (from a more complete data bank) should clarify whether (a) unambiguous features of S1 and S2 can be extracted, (b) the peaks in the spectra and the activity of heart valves (Tricuspid and Mitral for S1, and Aortic and Pulmonary for S2) can be correlated and, consequently, (c) specific patterns of S1 and S2 can be identified and correlated with foetal heart function and, consequently, foetal well-being (this further work is under way).

Acknowledgments

A. Jiménez González thanks CONACyT for sponsoring her PhD studies.

REFERENCES

[1] D.G. Talbert, W.L. Davies, F. Johnson, N. Abraham, N. Colley and D.P. Southall, “Wide bandwidth fetal phonography using a sensor matched to the compliance of the mother’s abdominal wall”, IEEE Trans Biom Eng, vol. 33(2), 1986, pp. 175-181.

[2] A. Jimenez-Gonzalez and C.J. James, “Source separation of foetal heart sounds and maternal activity from single-channel phonograms: a temporal independent component analysis approach”, Computers in Cardiology, vol. 35, 2008, pp. 949-952.

NEW METHODS IN ACOUSTIC STANDING WAVE OSCILLATOR DESIGN

A. D. Karenowska[1†], C. -C. Coussios[2] and J. F. Gregg[1]
[1]Department of Condensed Matter Physics, Clarendon Laboratory, University of Oxford, Oxford, UK,
[2]Institute of Biomedical Engineering, Department of Engineering Science, University of Oxford, UK

[†]corresponding author, a.karenowska@physics.ox.ac.uk,

Abstract – In this paper we describe a new type of controller for acoustic oscillators. Acoustic oscillators are used to generate ultrasound standing waves for numerous applications, including acoustic levitation and particle filtration. Our inventive positive-feedback, mode-selectable oscillator control scheme has three defining features: self-oscillating and self-tracking behaviour and a specially designed regulating non-linearity in the positive-feedback path to control the amplitude of acoustic oscillation. In particular, the fast auto-compensating characteristics of the instrumentation make it a candidate technology for the realization of levitators and separators applicable to dynamic biochemical and biomedical fluidic systems prone to rapidly changing acoustic properties.

I. INTRODUCTION

Small particles in suspension in the presence of an acoustic standing wave experience a force – the 'acoustic radiation force' – which causes them to migrate either towards or away from nodes in the pressure field [1]. The direction of migration is dependent on the acoustic contrast between the particulate matter and the suspending medium [2]. The effect is exploited for a range of particle separation, levitation and manipulation applications in a group of systems known as acoustic standing wave resonators. At the core of these devices is a standing wave cavity in conjunction with a sound source. Functionality is dependent on the maintenance of a standing pressure wave in the cavity, which may be filled with a liquid, gaseous or solid medium. The cavity typically features a family of acoustic resonances or 'resonant modes'. The frequencies corresponding to these modes are determined by a combination of the frequency response of the system sound source, the geometrical boundary conditions imposed by the cavity, and the acoustic properties of the cavity medium.

The overwhelming majority of acoustic resonator technologies reported to date are essentially negative-feedback 'driven' oscillators, operating at or around a single pre-defined frequency. In such schemes, the acoustic structure is driven via an external frequency source which is tuned to the frequency of the required operating mode. Open-loop manual tuning systems are relatively widespread, whilst more complex closed-loop systems use phase-sensitive-detection or related techniques [3-4]. Difficulties with all of these tuning methods are encountered if the acoustic properties of the standing wave cavity are subject to rapid change, and none offer modal selectivity – i.e. the ability to operate the cavity at more than one modal frequency.

This paper describes a new type of oscillator instrumentation which addresses the requirement for a more sophisticated, yet robust resonator platform technology [5]. The inventive positive-feedback controlled, mode-selectable scheme has three defining features: self-oscillating and self-tracking behaviour, and a specially designed regulating non-linearity in the positive-feedback path to control the amplitude of acoustic oscillation.

II. TECHNICAL INFORMATION

Methods

The positive-feedback acoustic oscillator controller (Fig. 1, top), incorporates three key components, an input amplifier, a phase compensator, and a specially developed 'optimal non-linear amplitude control element' (oN-LACE). The input amplifier has a frequency-dependent electronic transfer function providing both gain and modal selectivity. The phase compensator is used to adjust the total phase shift around the oscillator control loop. The oN-LACE is a fast-acting non-linear analogue regulator circuit, key to fast, stable, closed-loop operation. The controller processes an input signal from the resonant acoustic structure (Fig. 1, bottom) via an acoustic receiver, and provides a regulated drive to the system sound source.

An experimental acoustic oscillator was constructed for the purposes of evaluation. A planar acoustic source was manufactured using a Lead Zirconium Titanate ceramic element of 45 kHz nominal centre frequency housed in a purpose-designed transmit assembly (Fig. 1). The source was mounted on the side wall of a purpose-built, water-filled tank so as to face a stainless steel acoustic reflector. The length l of the standing wave cavity provided by the intervening space could be adjusted by moving the reflector (Fig. 1). A hydrophone receiver provided the interface between the resonant acoustic structure and an optimized version of the experimental positive-feedback controller.

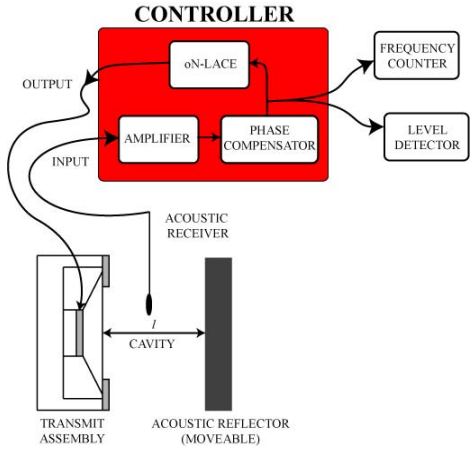

FIG. 1. The experimental acoustic structure: a sound source and a reflector are separated by a cavity of length *l* in the direction of acoustic propagation. In operation, a plane standing wave is supported in the cavity. The acoustic receiver (hydrophone) provides an input signal to the controller. The controller includes an amplifier, phase compensator, and optimal non-linear amplitude control element or 'oN-LACE'. The operating frequency of the oscillator is co-incident with the frequency of a selected resonant mode of the acoustic structure. As well as a frequency signal, an output proportional to the amplitude of acoustic oscillation in the cavity is available from the controller, represented by the 'level detector' above.

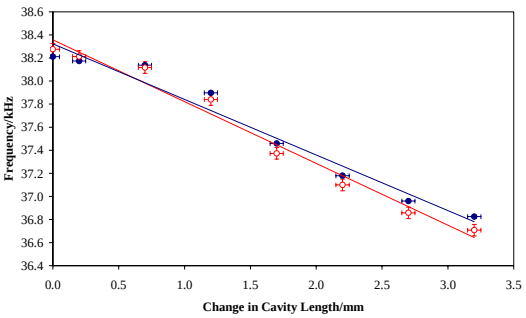

FIG. 2. Controlled system operating frequency (blue closed circle) and actual acoustic structure resonance frequency (red open circle) as a function of changing cavity length. There is good agreement between the two trends indicating that changes in the operating frequency of the auto-oscillatory system can be correlated with the changing acoustic properties of the cavity.

Results

At fixed cavity length, amplitude and frequency stable (within ±2Hz in 38kHz) auto-oscillation of the experimental oscillator was established at frequencies corresponding to different resonant modes of the acoustic structure. Three separate mode switching techniques were validated: repositioning of the hydrophone receiver, phase compensator adjustment, and modification of the frequency response of the controller amplifier.

Tracking performance was assessed by comparing the oscillator's frequency of auto-oscillation with the frequency of the corresponding resonant acoustic cavity mode. With the experimental control system operational, the phase compensator setting and hydrophone position were adjusted so as to establish a two-wavelength standing pressure wave in the acoustic structure. A frequency counter measured the operating frequency of the controlled loop. The reflector position was then adjusted to vary the cavity length *l*, and the new operating frequency of the system noted. Next, the control system was disconnected, and a variable frequency oscillator coupled to the sound source. For the values of cavity length *l* recorded in the previous part of the experiment, the true two-wavelength resonance frequency of the structure was determined by varying the driving frequency until the standing wave ratio in the cavity was maximized. A frequency tracking error of less than 1% over the measured range was achieved (Fig. 2).

Discussion

Though further development and optimization remains to be carried out, preliminary results indicate that in certain key applications (including the acoustic separation and levitation of time-varying biological or biochemical systems), the inventive self-oscillating instrumentation may provide an advantageous alternative to conventional acoustic resonator control technologies.

III. CONCLUSION

In summary, we have described the exciting potential of a new type of acoustic oscillator as a robust platform technology for a range of sophisticated, mode-selectable standing wave devices. The auto-tracking instrumentation may prove a valuable tool in tackling contemporary challenges in biochemical, biological and biomedical culture preparation, manipulation and filtration [6].

REFERENCES

[1] L. V. King, *On the acoustic radiation pressure on spheres*, Proc. R. Soc. London Ser. A, 147, 1934, pp. 212-240.

[2] K. Yosioka and Y. Kawasima, *Acoustic radiation pressure on a compressible sphere*, Acustica, 5, 1955, pp. 167-173.

[3] L. J. Thomas, *Marginal oscillator for acoustic monitoring of curing of plastics*, US Patent 4758803, 1988.

[4] K. Baxter, R. E. Apfel and P. L. Marston, *Versatile resonance tracking circuit for acoustic levitation experiments*, Rev. Sci. Instrum., 49(2), 1978, pp. 224-226.

[5] A. D. Karenowska, J. F. Gregg and C.-C. Coussios, *Acoustic Oscillator*, Patent Appl. No GB0900745.1, 2009.

[6] T. Laurell, F. Petersson and A. Nilsson, *Chip integrated strategies for acoustic separation and manipulation of cells and particles*, Chem. Soc. Rev., 36, 2007, pp. 492-506.

CONTINUOUS MEASUREMENT OF RESPIRATION RATE USING THE PHOTOPLETHYSMOGRAM AND THE ELECTROCARDIOGRAM

Syed Ahmar Shah, Susannah Fleming, Christina Orphanidou and Lionel Tarassenko

Institute of Biomedical Engineering, Department of Engineering Science, University of Oxford, Oxford, UK

syed.shah@eng.ox.ac.uk, susannah@robots.ox.ac.uk, christina.orphanidou@eng.ox.ac.uk, lionel@robots.ox.ac.uk

Abstract – This paper shows that it is possible to measure breathing rate automatically on a continuous basis in clinical settings using only the electrocardiogram (ECG) and photoplethysmogram (PPG), thus eliminating the need for any extra hardware. We verified this by testing on data from a single patient that consisted of ECG, PPG and a reference respiratory signal.

I. INTRODUCTION

Respiratory rate is an important parameter in patient monitoring. For example, a sudden change in respiratory rate can be caused by conditions such as airway obstruction or injury to the abdomen or pleural cavity [1]. Furthermore, an increased breathing rate is also an important clinical predictor of respiratory infections as well as more serious complications such as sepsis [2]. Continuous monitoring of breathing rate is therefore undertaken in many clinical settings including emergency departments, operating theatres, and intensive care units.

A number of methods including nasal thermistry (NT), capnography, inductance plethysmography, and electrical impedance plethysmography exist for the continuous monitoring of breathing rate. However, all of these methods require the use of extra hardware attached to the patients that can be difficult and inconvenient in many clinical settings.

The electrocardiogram (ECG) and photoplethysmogram (PPG) are, however, routinely measured in clinical settings. The ECG is a time-varying signal that measures the electrical activity of the heart via electrodes attached to the chest. The PPG is also a time-varying signal that is measured by a pulse oximeter, using a small, non-invasive finger probe, and provides information on blood oxygen saturation level and heart rate. The principle of pulse oximetry is based on the absorption of light by the pulsatile flow of arterial blood at two different wavelengths.

Both the ECG and PPG waveforms contain periodic peaks that occur in time with the heart rate. Respiration modulates the heart rate, a phenomenon known as respiratory sinus arrhythmia. In the work described in this paper, breathing rate is extracted from the heart rate variability information present in the ECG and PPG, and the results are compared with a reference breathing signal derived from NT.

II. METHODS

The data used in this work consists of a 60 minutes of continuous recording of ECG, PPG and NT signals from a single healthy subject. This data is part of a database that was collected by the Signal Processing and Neural Networks research group at Oxford University in 2002 [3].

A. Extraction of Reference Breathing Signal

Breaths in the NT signal (the reference breathing waveform) were identified using a peak detection algorithm and verified by visual inspection. A sliding window of 60 seconds with a 50 second overlap was used. For each window, an average breathing rate (the reference breathing rate) based on the identified breaths was calculated.

B. Extraction of time series from ECG and PPG

The R-wave peaks in the ECG were obtained using the Hamilton-Tompkins algorithm [4]. The RR time series was then obtained with each RR interval value taken to be at the corresponding first peak in the RR interval.

For the PPG, a salient point (termed the P point) corresponding to the highest positive slope was chosen. This point occurs once every cycle in the PPG waveform. The algorithm consisted of 2-point differentiation followed by thresholding to identify the peaks in the differentiated signal and locate the P-point in every cycle. The final stage of the algorithm was an error check to ignore any false peaks detected due to the presence of a dicrotic

notch, a secondary smaller peak typical of a PPG waveform.

Figure 1 shows a 40 second segment of PPG with the salient points detected by the algorithm shown as circles. From these points, the PP-time series is obtained.

Both the PP and the RR time series obtained were then interpolated using cubic-spline interpolation and resampled at 4 Hz.

C. Extraction of breathing rate from the PP-time series and the RR-time series

Both the PP and the RR time series contain significant DC and low frequency contents. Furthermore, the large occasional high amplitude peaks due to movement artefacts also contribute to the low frequency content of the signal. Instead of using a high-pass filter in an attempt to eliminate these, a different approach of normalizing the envelope of the signal was adopted. The algorithm detects all the peaks and troughs in the signal in order to estimate the envelope of the signal and then normalizes the amplitude of the signal to a value of 1.0.

Once the RR and the PP time series are normalized, an autoregressive (AR) model based frequency spectrum estimation, proposed earlier in [5], is performed using a 60 second sliding window with a 50 second overlap.

D. Results

Figure 2 shows the breathing rate obtained from the ECG, PPG and the reference breathing signal on the same figure. The results show that both the PPG based breathing rate and the ECG based breathing rate follow the reference breathing rate closely.

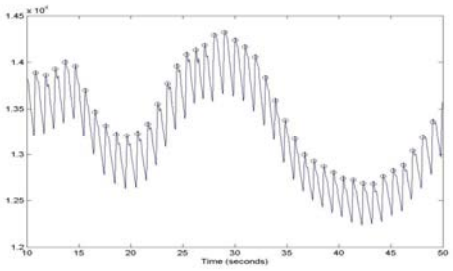

FIGURE 1: SALIENT POINT DETECTION IN PPG

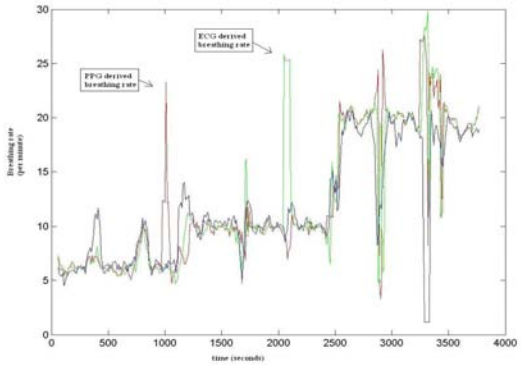

FIGURE 2: REFERENCE BREATHING SIGNAL (BLUE), PPG-DERIVED BREATHING RATE (RED) AND ECG-DERIVED BREATHING RATE (GREEN)

Furthermore, when there are errors in the estimates of the ECG-based breathing rate and the PPG-based breathing rate, these often occur at different times indicating that the errors are uncorrelated.

III. CONCLUSION

It is possible to automatically monitor breathing rate in different clinical settings without any need to attach any extra hardware. Furthermore, the errors in breathing rate extracted from the PPG and ECG are not necessarily correlated and therefore, it might be possible to combine information from the two sources to achieve greater accuracy.

REFERENCES

[1] P.A. Leonard, J. G. Douglas, et al. “A fully automated algorithm for the determination of respiratory rate from the photoplethysmogram”, Journal of Clinical Monitoring and Computing, volume 20 (1), 2006, pp.33–36

[2] S. G. Fleming, L. Tarassenko, et al. “Non-invasive measurement of respiratory rate in children using the photoplethysmogram” submitted to *30th Annual International Conference of the IEEE Engineering in Medicine and Biology Society*.

[3] C.L. Mason, “Signal Processing Methods for non-invasive respiration monitoring”, Dphil Thesis, Department of Engineering Science, University of Oxford, UK, 2002.

[4] P. S. Hamilton, W. J. Tompkins, “Quantitative investigation of QRS detection rules using the MIT/BIH arrhythmia database”, IEEE transactions on biomedical engineering, Volume BME-33 (12), Dec 1986, pp. 1157-1165

[5] S.G. Fleming, L. Tarassenko, “A comparison of signal processing techniques for the extraction of breathing rate from the photoplethysmogram”,International Journal of Biomedical Sciences, Volume 2 (4), 2007, pp. 232-236

CLASSIFICATION OF COLON IMAGES USING THE MAGNITUDE OF ORIENTATION DOMINANCE

Andreas Varnavas[1*], Ana Ignjatovic[2], Anil A. Bharath[1], James E. East[2], Brian P. Saunders[2], Jeffrey Ng[1], David Burling[3]

[1]Department of Bioengineering, Imperial College London, [2]Wolfson Unit for Endoscopy, St Mark's Hospital, London, [3]Department of Academic Radiology, St Mark's Hospital, London

*andreas.varnavas04@imperial.ac.uk

Abstract – We present a method for the discrimination of adenomatous and hyperplastic polyps in colonoscopy images, exploiting differences in the strength of the vascularity of their surface. The orientation dominance is proposed for the description of vascularity and suitable features are constructed, applying first order statistics on its magnitude. Using a linear classifier, our classification scheme produces a correct classification rate of 80.6% (sensitivity:81.58%, specificity:79.17%).

I. INTRODUCTION

Colonoscopy is the main clinical method used for the inspection of a person's bowel. During colonoscopy the endoscopist inserts a long flexible viewing tube (colonoscope) through the patient's anus and inspects the entire colon and rectum for presence of polyps. Polyps are divided into two main categories: adenomas, which are precursors to cancer, and hyperplastic, which are benign. Thus, upon the detection of a polyp, the endoscopist has to assess its nature and decide whether to proceed with the removal (adenomas) or leave in situ (hyperplastic polyps). Currently the default is to remove all polyps, whether an adenoma or not, but this blanket approach is costly and poses increased risks for patients.

An image processing algorithm, which exploits the visual characteristics of the polyp to classify it into one of the two categories, can be very useful, as it can support the endoscopist in the decision making process. Methods proposed so far for the desired classification construct features applying first and second order statistics on the image (colour) intensities [1] and on the DCT, DFT [2] and wavelet coefficients [3]. We propose here the use of the magnitude of orientation dominance [4] for the construction of features which depict the density of vascularity of the polyps' surface.

Vascularity is routinely used by expert colonoscopists for the visual characterization of a polyp, due to the more prominent existence of microvessels in the surface of adenomas. Narrow band imaging (NBI), a novel 'blue light' endoscopic technology improves contrast of these microvessels. As such, automated quantification of microvessels seen with NBI and its use in the feature construction process is of great interest [5].

II. THE COMPUTER AIDED CLASSIFICATION SCHEME

A. Feature Construction: Use of orientation dominance

Vessels appear in NBI as dark lines in the surface of the polyp and make its texture being locally oriented along one direction. In order to quantify the strength and the direction of this orientation, we construct the orientation dominance complex field, using the wavelet filtering technique proposed in [4]. In brief, an isotropic lowpass filter and a set of four oriented bandpass complex analysis filters, with orientations at angles $\varphi_k = 0, \pi/4, \pi/2, 3\pi/4$, are used for decomposition at a given scale. Thus, the orientation dominance at scale l is computed as:

$$\boldsymbol{O}^{(l)}(m,n) = \frac{\sum_{k=1}^{4} \left| \boldsymbol{f}_k^{(l)}(m,n) \right| e^{j2\varphi_k}}{p + \sqrt{\sum_{k=1}^{4} \left| \boldsymbol{f}_k^{(l)}(m,n) \right|^2}} \qquad (1)$$

where m, n are the image coordinates, $\boldsymbol{f}_k^{(l)}$ is the output of the k^{th} orientated filter at scale l and p is a normalization parameter set at 1% of the maximum value in the original image.

Computing the orientation dominance field for an image of a polyp according to Eq.(1) means that we first have to select the scale at which filtering will take place. This is related to the distance of the polyp relative to the camera. Since this information is not available, we choose to select the scale that best describes the strength of orientation dominance. Thus, for each image, the orientation dominance field is first computed for scales one, two and three. Then, we keep the magnitude of each vector and apply a low pass filter to eliminate abrupt changes. Finally, we keep for further analysis the (scalar) field with the largest mean value.

FIGURE I
STATISTICS OF MAGNITUDE OF ORIENTATION DOMINANCE

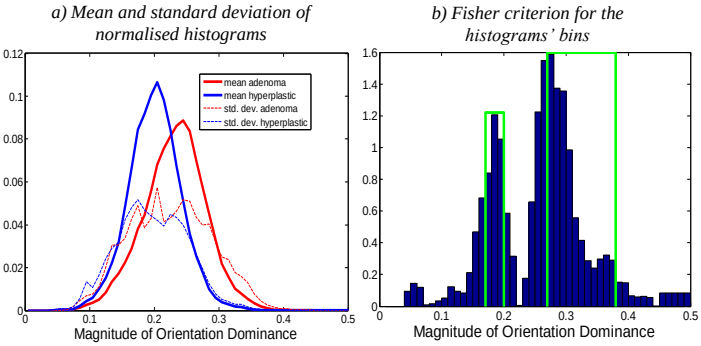

As mentioned earlier, adenomatous and hyperplastic polyps differ in terms of the vascularity observed in their surface. In general, the vascularity of adenomas is stronger and denser comparing to the one of hyperplastic polyps. To quantify these differences we compute the histogram of the magnitude of orientation dominance for

each polyp (selecting the scale as described above) and normalise it with the number of pixels in its surface. Then the mean histogram and the corresponding standard deviations of its bins are computed over the available images of each type of polyp, i.e. 38 adenomas and 24 hyperplastic polyps (see Figure I(a)). One can observe that the mean histogram of adenomas is higher for larger values of the magnitude of orientation dominance.

We next exploit the differences of the mean histograms to construct features for the discrimination between the two types of polyps. A total number of three features are constructed. The first feature is the normalised kurtosis of the magnitude of orientation dominance, defined as $k = \frac{E[(x-E[x])^4]}{\sigma^4}$. This measure was chosen because we observed that the histogram of adenomas has a more platycurtic shape than that of hyperplastic polyps (see Figure I(a)).

The next two features are the values of two bins of the histograms. The locations of these two bins are the intervals [0.17, 0.20] and [0.27, 0.38]. Although these intervals were heuristically chosen, they coincide with the points where the Fisher criterion is maximized. This can be seen in Figure I(b) where the Fisher criterion, defined as $f = \frac{(\mu_1-\mu_2)^2}{({\sigma_1}^2+{\sigma_2}^2)/2}$, is presented for a dense choice of bins (the corresponding intervals are marked with a green line).

In Figure II we plot the orientation dominance field (scale 2) on the image of an adenomatous and a hyperplastic polyp. The colour of the vectors is blue, red and black when their magnitude lies in [0.17, 0.20], [0.27, 0.38] and outside these intervals respectively. This is a representative example of how the magnitude of orientation dominance is related to the polyp's vascularity and the way it can be used for the discrimination of the two types of polyps.

B. Classification Process

Fisher Linear Discriminant Analysis is used for the classification process. For a two class problem, with $\boldsymbol{S_b}$ and $\boldsymbol{S_w}$ being the between-class and within-class scatter matrices respectively (estimated by the training set of 61 images), the direction maximizing the between-class to within-class scatter is found as the non negative eigenvector of $\boldsymbol{S_w^{-1}S_b}$. After projecting the feature vector of each polyp on this direction, classification takes place using a suitable threshold for the separation of the two classes. This threshold can be set at the middle of the projected means of the two classes but in general its value is determined by the desired trade-off between the sensitivity and specificity of the algorithm.

II. EXPERIMENTAL RESULTS

The proposed algorithm was tested using 38 and 24 images of adenomatous and hyperplastic polyps respectively. These images were captured using NBI and a magnification factor between 30 and 105 times. The reference standard was histopathology. The contour of the polyps was marked with the help of an expert so only the area of the image corresponding to the actual polyp's surface was used for further analysis.

The three-dimensional feature vector of each polyp was first constructed using the algorithm presented in Section II. Then, the "leave one out" method was used to train the classifier and estimate the correct classification rate. This means that the classification process was repeated 62 times, using each time 61 images to train the classifier and the remaining image for testing. The correct classification rate was finally computed as the ratio of correctly classified to total number of images.

Following this procedure, the correct classification rate (accuracy) was estimated as 80.6%, with sensitivity $\left(\frac{\#\text{correctly classified adenomas}}{\#\text{adenomas}}\right)$ at 81.58% and specificity $\left(\frac{\#\text{correctly classified hyperplastic}}{\#\text{hyperplastic}}\right)$ at 79.17%. These preliminary results are encouraging and are in accordance with the rates produced by other algorithms in the literature [1,2,3]. However, these results need to be validated with an external data set, which we aim to do in the near future.

FIGURE II
THE ORIENTATION DOMINANCE FIELD

a) Adenomatous polyp *b) Hyperplastic polyp*

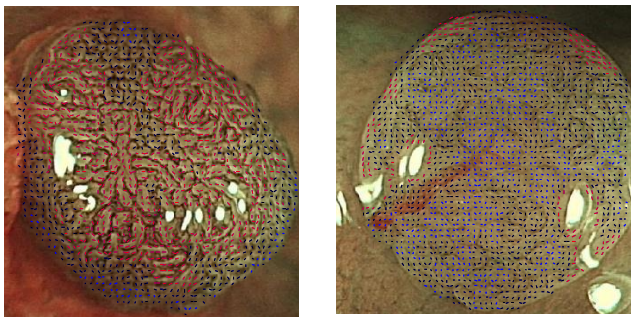

III. CONCLUSION

The produced classification rates presented here indicate that the magnitude of orientation dominance, as a means of quantifying the polyp's vascularity, is a useful measure for discriminating between adenomatous and hyperplastic polyps. In a future study we intend to combine it with other proposed features to investigate whether we can improve the classification accuracy.

REFERENCES

[1] M. Hafner et al, "Comparison of k-NN, SVM, and NN in Pit Pattern Classification of Zoom-Endoscopic Colon Images using Co-Occurrence Histograms", Proceedings of ISPA'07, pp. 516-521.
[2] M. Hafner et al, "Pit Pattern Classification of Zoom-Endoscopical Colon Images Using DCT and FFT", 20th IEEE Int. Symposium on Computer-Based Medical Systems, 2007, pp. 159-164.
[3] M. Hafner et al, "Pit Pattern Classification of Zoom-Endoscopic Colon Images using Wavelet Texture Features", Proceedings of MEDSIP'06, pp.1-4.
[4] A.A. Bharath and Jeffrey Ng, "A Complex Steerable Wavelet Construction and its Application to Image Denoising", IEEE Transactions on Image Processing, Vol 14, pp. 948-959, July 2005.
[5] J.E. East and B.P. Saunders, "Narrow band imaging at colonoscopy: seeing through a glass darkly or the light of a new dawn?" Expert Rev. Gastroenterol Hepatol., Feb. 2008, 2(1):1-4.

Proceedings of the 5th UKRI PG Conference in Biomedical Engineering and Medical Physics 2009

WATER REGULATION IN THE CEREBRAL ENVIRONMENT

Brett Tully, Yiannis Ventikos

Institute of Biomedical Engineering, University of Oxford, Oxford, UK.

brett.tully@eng.ox.ac.uk

***Abstract*—This research investigates acute hydrocephalus resulting from stenosis of the cerebral aqueduct. A novel spatio-temporal model of water regulation and tissue displacement in the cerebral environment is developed and interrogated.**

The multi-porosity, multi-permeability poroelastic theory is modified to investigate the influence of cerebrovascular- and intracranial-pressure on the flow of cerebrospinal fluid (CSF) and displacement of the brain tissue. Preliminary findings demonstrate clearly the importance that the fluidic-poroelastic coupling plays: ventricular enlargement is significantly reduced with local stenosis patterns and almost all the observable pressure drop occurs across the stenosis.

I. INTRODUCTION

Over the coming decades, the need for computational biological models will become increasingly apparent. In Europe, the Virtual Physiological Human (VPH) project is set-up as a collaborative investigation of the human body as a single complex system. It holds an ambitious goal to create quantitative, integrative and predictive models that describe human life from conception to death and from genes to whole organism [1].

The brain is the most important and complex of all the human organs and a computational investigation of this environment fits within the framework of VPH. Through well developed mechanisms the brain is able to function under a variety of conditions and sometimes drastic changes in its environment. Central to this are a set of delicate yet extremely efficient and sophisticated processes that control the regulation of water and ion flow, playing a pivotal role across all the spatial scales of the cerebral environment. Our inability to treat effectively a host of neurological conditions may be connected with our lack of understanding of the basic mechanics of this environment.

By coupling poroelastic theory with a multi-dimensional simulation of the cerebral aqueduct we are able to investigate, for the first time, the impact of physically relevant stenosis patterns on ventricular enlargement, accounting for the non-intuitive long time-history responses of the ventricular system.

II. POROELASTIC THEORY

Single fluid-network poroelastic thoery was first proposed by Biot [2] and has since been shown to be useful in modelling soft biological tissue. For instance, a poroelastic representation of the brain has been utilised to demonstrate the onset stages of acute hydrocephalus [3]. The theory generalizes Hooke's constitutive law for a solid-fluid mixture, by introducing a term for the fluid (pore) pressure, p. An isotropic, linearly elastic solid matrix subject to a stress field undergoes a small-strain deformation, u.

$$\mathbf{F} + G\nabla^2\mathbf{u} + \frac{G}{1-2\nu}\frac{\partial(\nabla\cdot\mathbf{u})}{\partial\mathbf{x}} - \alpha\frac{\partial p}{\partial\mathbf{x}} = \frac{\partial^2\mathbf{u}}{\partial t^2} \quad (1)$$

$$\frac{\partial p}{\partial t} - \kappa M\nabla^2 p = -\alpha M\frac{\partial(\nabla\cdot\mathbf{u})}{\partial t} - \kappa M\nabla\cdot\mathbf{f} + M\gamma \quad (2)$$

where G and ν are the bulk modulus and Poisson's ratio, α is the Biot coefficient, κ is the permeability of the CSF matrix, M gives the relative compressibility of the system and γ represent a source/sink of CSF.

III. SOLUTION METHOD

The governing poroelastic equations are simplified to a one-dimensional, quasi-steady approach and coupled with a multi-dimensional simulation of the cerebral aqueduct. The system is solved with an implicit second-order central finite differences scheme on the mid points and forward or backward Euler method used on the boundary nodes. The quasi-steady time discretization is performed through a first-order Euler approach. Flow through the multi-dimensional aqueducts is solved using the multi-physics software CFD-ACE+, based on the finite volume approach with central-difference spatial discretization, algebraic multigrid scheme and SIMPLEC pressure-velocity coupling. The coupling between the poroelastic solver and the flow solver is achieved through the use of CFD-ACE+ user-defined subroutines (UDS). After each time step of the poroelastic solver, the pressures at the skull and inside the ventricles are passed to the UDS as a pressure boundary condition. Following the solution of the aqueduct flow, the mass flux is calculated in the UDS and passed to the poroelastic solver for the next iteration.

IV. RESULTS

A particular drawback of the current poroelastic models is the assumption that Poiseuille flow through a pipe can model the dynamic effects of a stenosed aqueduct [3]. To model a blockage of the aqueduct, it is assumed that the diameter decreases along the full length of the pipe. The comparison of realistic stenosed aqueducts with the historical collapsed pipe tells us that assuming Poiseuille flow over the full length of the aqueduct may lead to overestimation of certain parameters. Fig. 1 shows a comparison of Poiseuille-flow and coupled flow simulations. There is negligible difference between the analytic and coupled approach when the entire length of the pipe is constricted (1-D and 2-D cases, respectively) telling us that the detailed CFD solution captures the analytic Poiseuille

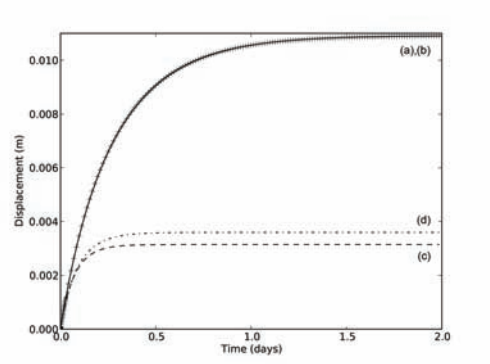

Fig. 1. A novel coupling of the poroelastic solver with CFD allows the investigation of the Poiseuille-law assumption. The 2-D coupled model (a) agrees with the 1-D analytic model (b) when the entire length of the aqueduct is constricted (Poiseuille approach). However, when the stenosis is modelled in a physically relevant manner – as an axi-symmetric (c) and fully three-dimensional (d) local stenosis – there is a significantly smaller enlargement of the ventricles.

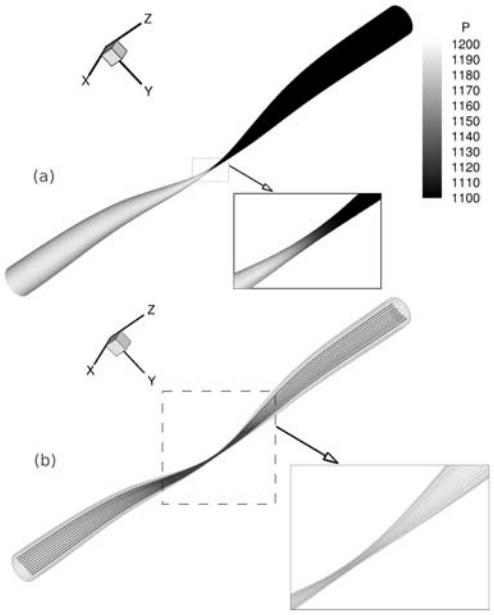

Fig. 2. Flow through the three-dimensional aqueduct shows: (a) distinct pressure drop through the restriction; and, (b) smooth flow through the aqueduct.

evolution, as expected. However, the locally stenosed axi-symmetric and 3-D aqueducts display a significantly smaller ventricular enlargement. This can be explained by Fig. 2(a) where it can be seen that all of the pressure drop occurs in the vicinity of the stenosed section and, for a given diameter, is of lesser magnitude than the pressure drop expected from the analytic approach.

V. DISCUSSION

This research extends current poroelastic models through a novel coupling with a multi-dimensional aqueduct. In doing so, it is possible to investigate the role of pulsations in CSF flow, assess the potential for small intracranial pressure gradients to lead to ventricular dilation and determine the impact of the magnitude of the stenosis on ventricular pressure and dilation. It is shown that current analytic models may overestimate ventricular enlargement and a significant obstruction must be present to cause ventricular enlargement on the scale seen in clinical data.

The results provide a useful insight into the theories of hydrocephalus. However, there are too many simplifications and assumptions in the current model for it to provide clinically useful, quantitative statements. The most significant of these assumptions are the simplified geometry and the mechanical properties of the tissue. Furthermore, we have used small-strain, quasi-steady approximations in our constitutive relationship, which is likely to restrict this model to the onset stages of hydrocephalus only.

VI. CONCLUSION

This research focuses on the novel coupling of poroelastic and flow solvers to investigate acute hydrocephalus resulting from stenosis of the cerebral aqueduct. There is little contention that this type of obstruction to CSF movement will result in dilatation of the ventricles. However, the underlying physics must also provide useful information on the pathophysiology of chronic, non-obstructive hydrocephalus. It is shown that analytic assumptions often introduced in the current state of the art poroelastic models may overestimate ventricular dilation. That is not to say that poroelastic theory should be abandoned in preference of another methodology. In fact, we suggest that poroelastic theory is an important part of the solution, however, it should be enhanced and expanded in order to match the physical system more closely. Work in the immediate future will aim to increase the physical relevance of the geometry, while addressing some of the more fundamental limitations of a single fluid-network poroelastic model.

In the search for a better understanding, Bergsneider *et al.* [4] outline ten fundamental, un-answered questions about hydrocephalus. Computer modelling shows great potential to help in the search for answers, however, to be successful it is necessary that the level of interrogative representation and multiscalarity reach more physically representative levels.

ACKNOWLEDGMENT

The authors would like to thank the ESI Group (Paris, France) and Dr. M. Megahed for making the CFD-ACE+ platform available to us. This work was made possible by the support of the Oxford University Clarendon Fund and British ORS award.

REFERENCES

[1] STEP Consortium, "Seeding the europhysiome: A roadmap to the virtual physiological human," Online: http://www.biomedtown.org/biomed_town/STEP/Reception/step_presentations/RoadMap/vph_roadmap_printed_3.pdf, Jan. 2009.

[2] M. Biot, "General theory of three-dimensional consolidation," *Journal of Applied Physics*, vol. 12, pp. 155–164, Feb. 1941.

[3] A. Smillie, I. Sobey, and Z. Molnar, "A hydroelastic model of hydrocephalus," *Journal of Fluid Mechanics*, vol. 539, pp. 417–443, 2005.

[4] M. Bergsneider, M. R. Egnor, M. Johnston, D. Kranz, J. R. Madsen, J. P. Mcallister, C. Stewart, M. L. Walker, and M. A. Williams, "What we don't (but should) know about hydrocephalus," *Journal of Neurosurgery: Pediatrics*, vol. 104, no. 3, pp. 157–159, 2006.

Magnetic Antenna for Near-Field Pulse Radio Communication

Sandeep Manjunath and David R. S. Cumming
Dept. of Electronics and Electrical Engineering
University of Glasgow
Glasgow, UK, G12 8LT
Email: s.manjunath@elec.gla.ac.uk

***Abstract*—A novel method of implant communication is presented in this paper. Unlike traditional wireless technologies, the proposed system operates in the near-field region of the antenna. The antennas act as pulse shaping filters and hence use of modulators is unnecessary. This effectively reduces the number of block components and power budget of the overall implantable system thus making this near-field baseband system attractive for integration with lab-in-a-pill or system-on-chip technologies. A decision choice between magnetic antennas and electric antennas is made to enhance the advantages provided by the proposed pulse radio system.**

I. Introduction

Implantable telemetry systems transmit physiological information, for instance temperature, oxygen, pH and blood glucose concentration, regarding animals or human beings. Pill shaped implants are able to transmit critical information from closed cavities or inaccessible places wirelessly as shown in Fig. 1 [1].

Wireless connectivity has always been provided by traditional communication schemes, including back-scatter, frequency modulation (FM) and amplitude modulation (AM). Digital communication has received considerable interest in recent years, wherein digital signals are modulated using amplitude-shift keying (ASK), frequency-shift keying (FSK) and phase-shift keying (PSK). FM and ASK are the most adopted forms for robustness and simple circuitry [2], [3]. Invariably, all the above mentioned methods require hardware blocks such as oscillators, mixers and power amplifiers. This in practice translates to larger area of implementation and stringent power requirements. They also suffer from low data rates that might be crucial for applications involving gastrointestinal tract imaging or stimulation of neural prosthesis.

In this work, we propose a new transmission scheme that discards the use of mixers or oscillators and simply involves direct relay of baseband pulses from an antenna. The novelty lies with the fact that antennas act as pulse shaping modulators.

II. Antenna Choice: Electric or Magnetic?

The idea of transmitting digital pulses, without any modulation, stems from the fact that individual pulses occupy very large instantaneous bandwidths. This suggests that the pulses might propagate without a carrier. In this particular system, antennas should complement the advantages of a pulse based transmission scheme. Antennas come in various shapes and sizes. Some are sensitive to electric fields and the others to magnetic fields. As the antennas have to be small enough to be integrated inside a pill-shaped object, it can be no more than a few centimetres. Electromagnetic waves are strongly absorbed inside the human body and the absorption increases as the frequency increases [4]. It is suggested that the range of frequencies should be in the high frequency rather than very high frequency. Therefore the operational bandwidth has to be specified within an acceptable level. With the above mentioned design constraints, the suitabilty of electric or magnetic antennas for use in our system is investigated.

The size and frequency of operation suggests that the wave energy has to be coupled in the near-field. While doing so, it has to preserve the pulse shape also. Therefore the temporal and frequency characteristics of an antenna need to be determined. We approach this design problem by considering an antenna as a pulse shaping filter that can be represented by a lumped equivalent circuit.

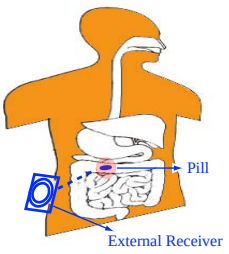

Fig. 1. Ingestible Pill and an External Receiver.

A dipole can be regarded as a network of lumped elements [5]. Advanced Design Simulator (ADS) was used to simulate the behaviour of a dipole excited by a pulse. The amplitude of the pulse is $1\,\mathrm{V}$ and its width $0.5\,\mu\mathrm{s}$. It can be deduced from Fig. 2(a) (shown red) that the dipole antenna behaves like a capacitor and stores almost all of the energy electrically, across its terminals. The voltage that appears as magnetic energy in a dipole is shown in Fig. 2(a)(shown black). The amplitude levels are too low and hence signal will be lost in the background noise. The electric energy might be coupled if the dipole antenna can come into contact with bodily fluids which is undesirable [6]. Hence use of dipole antennas and in general electric antennas is infeasible.

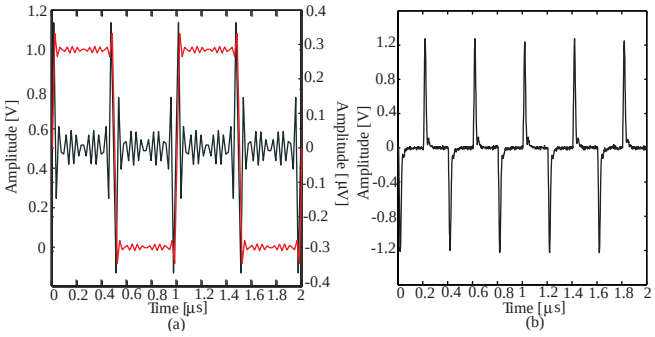

Fig. 2. Energy Waveforms:(a)Electric; and (b)Magnetic.

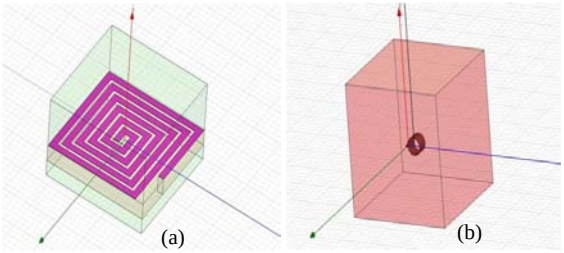

Fig. 3. (a)Square Loop Antenna; and (b)Solenoid Antenna.

A loop antenna can be represented by a network of passive elements. The resistance represents the sum of radiation and loss resistances. The loop antenna was designed to have a flat magnitude response and almost linear phase response. The broad passband characteristic perfectly preserves the rising and falling edges that help decoding the symbol transmitted as shown in Fig. 2(b). Hence the transmission may be termed as a waveform transmission. The magnetic energy stored in the inductance L_e was modulated by the pulse excitation and hence information transmitted by mutual coupling between the transmission and reception antennas.

The transmitting antenna has to be designed to allow for maximum reactive energy in its near-field. A loop antenna can be regarded as a magnetic dipole, in which magnetic current I_m is directly proportional to the area S of the radiating element [7]. Loop antenna can be efficiently utilised for transmission either by driving more current or maximising the area in a given volume as suggested by (1). Ansoft HFSS was used to analyse the reactive fields of a printed square loop antenna and a solenoid antenna. The square loop antenna had 6 turns, a track width of 0.5 mm on a duroid substrate of thickness 1 mm, as shown in Fig. 3(a). The solenoidal loop had 9 turns, a loop radius of 5 mm and a pitch of 1 mm, as shown in Fig. 3(b).

$$I_m l = jS\omega\mu I_o \tag{1}$$

III. Results and Discussion

Figs. 4(a) and 4(b) show the simulation results of variation of gain with distance in the case of a square and solenoidal loop antenna respectively. Figs. 4(c) and 4(d) show the experimental results. With the square loop, it can be seen that gain falls rapidly with distance. The range of operation is upto few millimeters. But as opposed to a square loop, a solenoid has gradual decrease in gain with distance and the range of operation is also increased significantly. Both are in good agreement with each other. Hence it can be concluded that the best choice for a transmitting implant antenna is a solenoid that occupies comparatively larger volume than a printed spiral shaped antenna element. The inductive magnetic energy density is also higher in the solenoid.

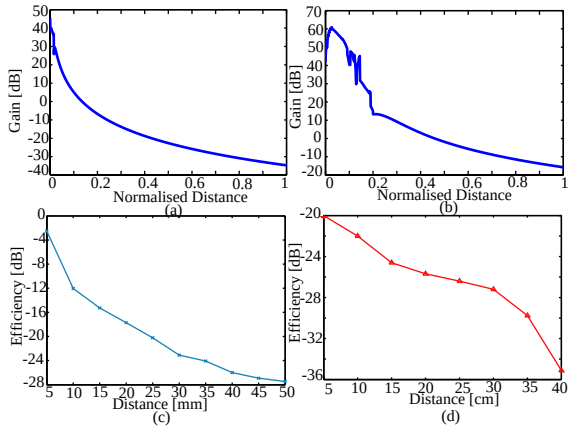

Fig. 4. Gain Vs Normalised Distance(a)Square Loop; (b)Solenoid; Experimental Results(c)Square Loop; and (d)Solenoid.

IV. Conclusion

A new approach to the design of implant antennas is presented in this paper. The reactive energy as opposed to the radiating energy is utilised to carry information as baseband pulses. Solenoidal antennas are preferred over printed loop antennas.

Acknowledgment

This project was funded by an ORS scholarship.

References

[1] L. Wang, E. A. Johannessen, P. Hammond, L. Cui, S. W. J. Reid, J. M. Cooper, and D. R. S. Cumming, "A programmable microsystem using system-on-chip for real time biotelemetry," *IEEE Trans. Biomed. Eng*, vol. 52, no. 7, pp. 1251–1260, 2005.

[2] N. M. Neihart and R. R. Harrison, "Micropower circuits for bidirectional wireless telemtry in neural recording applications," *IEEE Trans. Biomed. Eng.*, vol. BME-52, no. 11, pp. 1950–1959, 2005.

[3] M. Ghovanloo and K. Najafi, "A BiCMOS wireless stimulator chip for micromachined stimulating microprobes," *Proc. IEEE 2nd Joint EMBS BMES Conf.*, pp. 2113–2114, Oct. 2002.

[4] L. C. Chirwa, P. A. Hammond, S. Roy, and D. R. S. Cumming, "Radiation from Ingested Wireless Devices in Biomedical Telemetry Bands," *Electronics Letters*, vol. 39, no. 2, pp. 178–179, Jan. 2003.

[5] T. G. Tang, Q. M. Tieng, and M. W. Gunn, "Equivalent circuit of a dipole antenna using frequency-independent lumped elements," *IEEE Transactions on Antennas and Propagation*, vol. 41, no. 1, pp. 100–103, Jan. 1993.

[6] S. J. Song, N. Cho, and H. J. Yoo, "A 0.2-mW 2-Mb/s Digital Transceiver Based on Wideband Signaling for Human Body Communications," *IEEE Journal of Solid-State Circuits*, vol. 42, no. 9, pp. 2021–2033, Sep. 2007.

[7] C. A. Balanis, *Antenna Theory:Analysis and Design*, 3rd ed. Wiley Interscience, John Wiley and Sons, 2005.

ACCELERATED GENERATION OF DIGITALLY RECONSTRUCTED RADIOGRAPHS

O. Dorgham[1], M. Fisher[1] and S. Laycock[1]

[1]School of Computing Sciences, University of East Anglia, Norwich, UK

{O.Dorgham, Mark.Fisher, S.Laycock}@uea.ac.uk,

Abstract – In this paper we present an approach for speeding up the generation of Digitally Reconstructed Radiographs (DRRs). The generation of Digitally Reconstructed Radiographs (DRRs) is a bottleneck in 2D/3D medical image registration. This registration approach is required when the patient's anatomy needs to be aligned with a 3D data used for surgical planning, a situation that routinely arises during the delivery of radiotherapy treatment. This paper focuses on high speed rendering of DRR images from a CT volume exploiting low cost multi-core parallel processing architectures currently available on a PC. The results demonstrate speed-up the rendering of DRR images better than three times.

I. INTRODUCTION

2D/3D medical image registration is achieved by matching (registering) reference X-ray images to synthesised 'floating' Digitally Reconstructed Radiograph (DRR) images, derived from three-dimensional Computed tomography (CT) volumetric data. The output from a 2D/3D medical image registration process is a rigid transformation (rotation and translation), which when applied to the floating volume yields a DRR which is in some sense a best match to the reference X-ray image. Some authors have also considered registrations involving more complex non-rigid transformations (rotation, translation, scaling and warping), but as our focus is currently the rendering of DRR images, our current registration system only uses affine transformations.

2D/3D registration is widely used to confirm patient setup prior to radiation therapy treatment. DRRs are generated from CT volumetric data by summing the attenuation of each voxel along known ray paths through the CT volume. However, this conventional ray tracing approach to DRR rendering is an extremely computationally expensive process and forms a bottleneck in 2D/3D image registration [1]. Normally, conventional DRR generation requires $p \times q$ rays to be cast to generate a DRR from a CT volume; where p and q are determined by the image resolution, usually chosen to match that of the solid-state flat panel X-ray detector used to form the reference image.

Recently, we have investigated two fast methods of rendering DRRs, both offline and online. For the offline approach the CT volume is compressed using an Octree data structure. As the resulting partition involves fewer subspaces DRRs we have demonstrated that can be rendered (online) more quickly, using a conventional ray tracing algorithm (more information about this method can be found in [2]).

The second approach we are investigating involves parallel processing (i.e. the simultaneous use of more than one CPU to execute a program [3]). In simple terms, we generate DRR images by casting rays using more than one processor in order to obtain faster results. This means we are now able to process more than one ray concurrently. This multi-threaded technique is well suited to multi-core CPUs found in many modern PC's and we have obtained significant speed up in the generation of DRRs with this approach. In our knowledge this is one the first studies to generate DRRs images exploiting CPU parallel processing to be used within a 2D/3D registration framework.

II. METHOD

The complexity of DRR generation results from the massive number of calculations needed and the large number of ray casting operations. Compared with more general surface rendering techniques, rendering DDR images is considerably more computationally demanding as we need to compute the attenuation of a monoenrgetic beam due to different anatomic material (e.g. bone, muscle tissue etc.) within each voxel, using Beer's Law [4].

$$I = I_0 \times \exp^{\Sigma -\mu_i x_i}$$

Where I_0 is the initial X-ray intensity, μ is the linear attenuation coefficient for the voxel (material) through which the ray is cast, x is the length of the X-ray path and subscript *i* denotes the voxel index along the path of the ray, as illustrated in Figure 1.

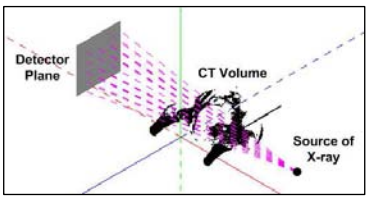

Figure 1: Shows the process of DRR generation

Voxel values in CT volumes are represented by CT number quantified in Hounsfield Units (HU). The attenuation coefficient of the material comprising each voxel can be recovered by [5]:

$$CT_{number} = 1000 \times [(\mu_i - \mu_w)/\mu_w]$$

Where μ_i is the attenuation value of a particular volume element of tissue (voxel) and μ_w is the linear attenuation coefficient of water for the average energy in the CT beam.

A. Parallel Processing

Our objective is to increase the speed of DRR generation using parallel processing. To test the approach, we developed and implemented the following algorithm (Algorithm 1) in C++ using the OpenMP library.

Algorithm 1 Parallel processing of DRR generation using OpenMP

```
1: #openmp start parallel for
2:   for i ← 0 ; i < ImgDimX ; i++
3:     count ← i × ImgDimY
4:     for j ← 0 ; j < ImgDimY ; j++
5:       x_ray ← x_rays[count]
6:       absorptionSum ← 0
7:       for t0 ← stratTime ; t0 < endTime; t0++
8:         if CTimg.intersection(x_ray)
9:           inrsecPnt ← x_ray.getPosition(t0)
10:          absrp← CTimg[CTimg.offset(inrsecPnt)]
11:          absorptionSum← absorptionSum + absrp
12:        end if
13:      end for
14:    drr.setAbsorption(absorptionSum )
15:    count ++
16:  end for
17: end for
14: #openmp end parallel
```

The execution times (of the parallel Algorithm) for different number of cores with different size of CT volumes were compared as shown in Table I.

TABLE I
Time consumption of pelvis DRR images generation in milliseconds, with and without interpolation*.

	Number of Processors		
DRR Image Size	**Single**	**Dual**	**Quad**
128 x 66	55, 15*	27, 8*	14, 4*
256 x 133	665, 205*	346, 111*	181, 58*
512 x 267	5523, 1635*	2865, 863*	1516, 466*

Samples of the resulting DRR images using parallel processing are presented in Figure 2.

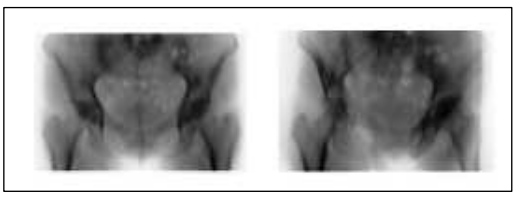

Figure 2: Samples of DRR images generated from pelvis CT volume, using parallel processing.

B. Performance

Writing our algorithm in OpenMP does not offer algorithmic capabilities that are not already available in C++. So the main reason to program in OpenMP is performance [6]. Our results in Table I, match the curves of Amdahl's law at 90% of parallel portion. This means that the algorithm represents about 90% of the parallel portion of the DRR generation, as illustrated in Figure 3.

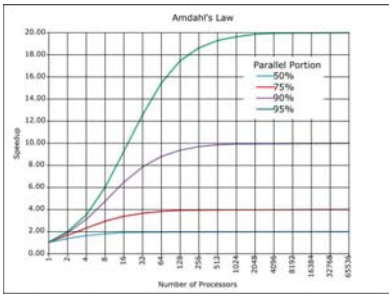

Figure 3: The relation between the number of processors and the gained speed up [7].

III. CONCLUSION

The growth and availability of multi-core technology provides a low cost computing platform which we have exploited to speed-up the generation of DRR images. The acceleration we achieve varies according to the number of processors. Our results shows that we can speed-up the generation of DRR images better than three times, by using parallel processing with a machine employing 4 processor cores. An important consideration is that our approach of CPU parallel processing does not require any pre-processing steps. Future work will investigate the effect of further increasing the number of processors.

REFERENCES

[1] A. Khamene, P. Bloch & W. W. et.al. "Automatic registration of portal images and volumetric CT for patient positioning in radiation therapy." Medical Image Analysis 10, pp. 96–112, 2006.

[2] Osama Dorgham and Mark Fisher. Performance of 2D/3D medical image registration using compressed volumetric data. In Proc. Medical Image Understanding and Analysis 2008, pp. 261–265, 2008.

[3] Kumar Vipin, Grama Ananth, Gupta Anshul, and Karypis George, Introduction to parallel computing: design and analysis of algorithms, Benjamin-Cummings Publishing Co., Inc., 1994.

[4] R. A. Ketcham & W. D. Carlson. "Acquisition, optimization and interpretation of X-ray computed tomographic imagery: applications to the geosciences." Comput. Geosci. **27**, pp. 381–400, 2001.

[5] L. B. Schwartz, D. L. Olive & S. McCarthy. Diagnostic Imaging for Reproductive Failure. Taylor and Francis Ltd, UK, 1998.

[6] Chandra Robit, Dagum Leonardo, Kohr Dave, Maydan Dror, McDonald Jeff, and Menon Ramesh, Parallel programming in openmp, Morgan Kaufmann Publishers Inc., 2001.

[7] Daniels220, Amdahl's law, available at: http://en.wikipedia.org/wiki/File:AmdahlsLaw.svg, last accessed: May 2008.

DYNAMICALLY PROGRAMMABLE M-PSYCHIATRY SYSTEM FOR SELF-MANAGEMENT OF BIPOLAR DISORDER

J.M. Blum[1] and E.H. Magill[1]
[1]Department of Computing Science and Mathematics, University of Stirling, Stirling, UK
{jmb,ehm}@cs.stir.ac.uk

Abstract – A rule-oriented approach to programming mobile psychiatric monitoring systems was designed. Initial simulations of rule processing have tested system personalisation issues and reviewed characteristics of the rule-oriented approach including the degree of task expressiveness and ease of expressing domain knowledge. A technical trial is being prepared to analyse the approach in a non-simulated environment.

I. INTRODUCTION

The Personalised Ambient Monitoring (PAM) project is investigating the feasibility of reducing the incidence of debilitating episodes of Bipolar Disorder (BD) by monitoring activity signatures using mobile and environmental sensors. Monitoring activity signatures may detect changes in patient mental health and alert sufferers and their care providers early enough to maintain eurythmia.

System personalisation is a core issue for PAM since activity signatures differ amongst patients and can change over the course of patient lifetime. The types of sensors used, and their patterns of usage, must be personalised in order to match patient states and be accepted by users. System personalisation requires a dynamic and flexible programming method but it must also be easy to program, represent domain information and above all result in correct system behaviour.

This paper discusses the developement and initial assessment of a rule-oriented approach to personalise PAM technology called PAM-A. The research extends other work on rules-based sensor network programming by using rules to turn a mobile phone into a mobile sensor network gateway. We used a simulated scenario to test whether this approach could simplify programming, make proving program correctness easier, and remain highly expressive, as is asserted for other forms of rules-oriented sensor networks in [2]-[3].

II. METHODS

A mobile phone-based healthcare platform was designed and tested against a scenario to review domain knowledge expressiveness, programming simplification and program correctness.

A. Platform Description

The Personalised Ambient Monitoring Infrastructure (PAM-I) is a wireless network comprising wearable sensors, mobile phones and in-home sensors. Data is enhanced with patient-recorded answers to mood and activity questionnaires.

Custom Java-based middleware called the Personalised Ambient Monitoring Architecture (PAM-A) was developed to program PAM-I devices by handling inter-device network connections, controlling data streaming frequencies, recording streamed data to persistent storage and transferring data offsite for long term storage and analysis. PAM-A stores connection and frequency settings, along with questionnaire results in a knowledgebase. It uses a Java-based implementation of Prolog for mobile devices as a rule engine to control monitoring [1]. Settings are processed by the rule engine and used to personalise the system. Figure 1 depicts PAM-I and PAM-A.

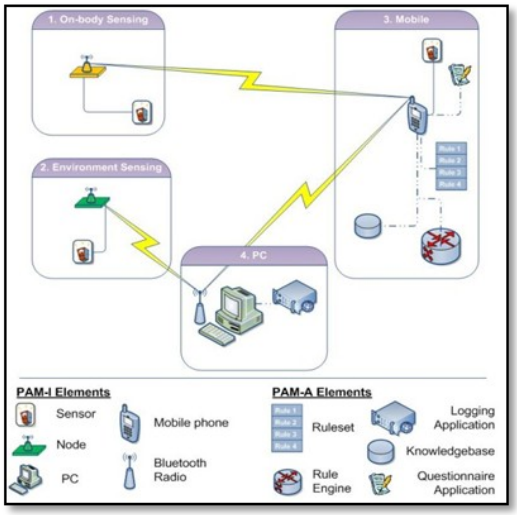

Figure 1. Graphical view of PAM-I and PAM-A

B. Scenario Test

The degree to which the rule-oriented programming model of PAM-A could easily and correctly express a common BD case was examined by simulating characteristics of the system using a scenario we called “Manic Phoning”. The scenario identified increased talkativeness by monitoring the mobile phone call log and dynamically reacting to changes with appropriate notifications. It was chosen to illustrate a series of interactions between

identified actors and exclusively concentrated on the phone software, thereby testing the programming model without regard to hardware concerns. The scenario was motivated by research into changes in BD patient talkativeness [4].

The PAM-A software and rules were tested with Symbian s60 (3rd ed.) mobile phone emulator. To test the scenario, its description was encoded as Prolog facts and rules, and actions were coded as first-class objects in Java. The rules and objects were dynamically loaded into the device mediator at runtime.

III. RESULTS

The test environment successfully simulated making phone calls and sending appropriate warning notifications. The program simulated accessing the mobile phone call log a number of times and tried to detect the prodrome "talkativeness". The ruleset described actions to check call frequency and duration after each call was made. The maximum call per day threshold and maximum call length threshold were easily personalised to match the scenario description. The prodrome "talkativeness" was registered when the thresholds were exceeded and personalised warning text messages were sent at the expected times. When messages were sent, the knowledgebase was dynamically updated with the time the message was sent to prevent multiple notifications per day.

IV. DISCUSSION

The system simulator met its goal of monitoring aspects of patient behaviour using a mobile rule engine to respond correctly to changes in user behaviour. However, the programming approach was not as simple to use as originally envisioned due to complex interrelationships between the ruleset and the action objects. Writing valid Prolog rulesets to declare the domain knowledge was relatively easy as was programming the Java action objects, yet, the success of the program was founded on a working knowledge of both languages and views into how the rules and actions interacted. Future work is required to simplify the process to allow domain experts to describe expected usage patterns resulting in valid and complete rulesets.

Work is now underway to test PAM-A in a live environment using real sensors and mobile phones during a technical trial. The trial will be used: to evaluate component integration and system acceptability, to assess reliability issues, to determine the feasibility of capturing behaviour unobtrusively and to investigate whether the recorded data can be used to inform an operational research model.

PAM-A is being used to personalise wearable and environmental sensor data for the trial. Rules on phones are used to access built-in sensors such as GPS receivers and questionnaire applications, and control data collection rates of wearable sensors to balance power issues with the need for complete sets of data. They are also being used to personalise mobile phones and wearable/environmental sensors to make sure that the devices selected for monitoring, and their monitoring patterns are acceptable to subjects. We hope to show that rules can be used to auto-configure the monitoring to match patient preferences. For instance if sleep monitoring was desired but a patient objected to placing a sensor in bed, rules could be used to configure other environmental sensors such as PIR sensors to attempt to monitor for nightly activity.

V. CONCLUSION

The PAM m-psychiatry healthcare information system was designed to monitor activity signatures of the mentally ill, with the hope of reducing manic and depressive episodes. To deal with inherent system personalisation issues, the PAM team have developed a novel dynamic sensor network middleware integrating logic rules and first-class action objects. Initial simulations of the system have shown promising results. A technical trial is being prepared to analyse system acceptability and reliability.

ACKNOWLEDGEMENTS

We wish to thank the Engineering and Physical Sciences Research Council (EPSRC) for funding the PAM project, the Universities of Nottingham, Southampton and Stirling for their support, and our fellow team members on the PAM project.

REFERENCES

[1] *mProlog: Lightweight PROLOG Engine*, 3APL Group, http://www.cs.uu.nl/3apl--m/mprolog.html, last accessed on 13 August, 2008

[2] S. Sen and R. Cardell-Oliver, *A Rule-Based Language for Programming Wireless Sensor Actuator Networks using Frequency and Communication*, Third IEEE Workshop on Embedded Networked Sensors, 2006

[3] X. Fei and E. Magill, *Rule Execution and Event Distribution Middleware for PROSEN–WSN*, Proceedings from the Second International Conference on Sensor Technologies and Applications, 2008

[4] R. Morriss, *The early warning symptom intervention for patients with bipolar affective disorder*, Advances in Psychiatric Treatment, vol. 10, pp. 18-26, 2004

FABRICATION AND CHARACTERIZATION OF SU8 POLYMERIC MICRORING RESONATORS FOR BIOSENSORS

M. Hazimin M.S[1], R. Wilson[1], A.Glidle[1], M.Sorel[2], J.M. Cooper[1]

[1]*Bioelectronics Group, Department of Electronics & Electrical Engineering, University of Glasgow, Glasgow*
[2]*Optoelectronics Group, Department of Electronics & Electrical Engineering, University of Glasgow, Glasgow*
mhazimin@elec.gla.ac.uk

Abstract - In this paper, SU8 polymer was used to fabricate a waveguide and microring resonator for optical biosensing applications in biological (aqueous) media (e.g. to measure protein or DNA interactions). Fabrication steps and results obtained by using UV photolithography at 2µm gap and electron beam lithography showing the fabrication of microring with 200µm of radius with a 200nm critical coupling gap are presented. Characterization of the SU8 waveguide including propagation and bending losses was performed by using HeNe laser 632.8 nm of wavelengths. Future works on resonator characterization, immobilization, and resonance wavelength shift measurement are currently in progress.

I. INTRODUCTION

Polymeric materials offer many advantages over inorganic silica waveguides in terms of their processability and cost. They can be easily structured for optical sensor waveguide application, and currently, there is significant interest on investigation of SU8 polymer because of easy fabrication [1], processing, integrated on lab-on-chip and optical-waveguide sensors.

One of the general waveguide structures, which can be used for biosensing, is the microring resonator. It offers an advantage over other structures in reducing the device size without scarifying the interaction length between the light and the biological material. The strength of the interaction can be measured by the resonance wavelength shift at high quality-factor (Q) resonance [2]. Interaction event between antibodies that immobilised on SU8 waveguide surface with antigen (in solution) will change the effective refractive index of microring resonator, thus resonance wavelength [3]. Resonance wavelength shift after interaction event will be measured. High Q factors improve the sensitivity due to the long residence times of the photons that propagate within the ring (which increases the probability of photons interacting with the analytes in solution).

II. METHODS

A. Waveguide fabrication

The SU8 waveguides were fabricated using SU-8 2 (MicroChem, Newton MA, USA) as a core material. Waveguide and microring resonator structure were fabricated on the top of 3.5µm thick oxide in Silicon wafer. First step was the spin coating of the SU8 to obtain a layer of 2µm thick with a spin speed of 3000 rpm at 30 s. The layer was soft baked at 95^{o}C on the hotplate for 120 s. After the polymer was exposed, post exposure bake is performed on the hotplate at 65^{o}C and subsequently moved to 95^{o}C for 60 s each. The following step, polymer was chemically developed with Microposit ™ EC solvent at 120 s and rinsed by IPA or deionised water. The polymer was then hard baked on the hotplates at 180^{o}C for 180 s.

B. Dose test

Before we fabricated the structure, we performed a dose test for UV photolithography and electron beam on SU8, to optimise the exposure time and working dose (e.g. UV photolithography from 10 – 30 seconds), and the dose test for electron beam lithography (VB6, JWNC) from (100 - 1.0) µC/cm^2.

C. Propagation Losses

The losses of polymer waveguides were measured using the "cut-back method" for a waveguide with a width of 2µm. The length of the samples was cleaved from 35 to 10 mm in four steps. The HeNe laser was end-fire coupled using lensed fiber (6 µm lens, Advance Fiber Product Ltd). The output light was collected at the opposite end using same method with bare fiber coupling. The signal was analysed with optical spectrum analyser (OceanOptics, HR2000CG-UV-NIR, USA)

D. Bending Losses

The bending losses of polymer waveguide are an important parameter if the fabricated structures consist of curve. For microring resonator, the bending loss is a crucial aspect to identify because losses in the ring structure

are related to the arc of the waveguides curve. Using a waveguide width size of 2µm we fabricated rings with different radii between 500µm to 1µm. The bending losses were measured using 632.8nm laser light, same setup as describe above.

III. RESULTS AND DISCUSSION

B. Dose test

i. UV Photolithography

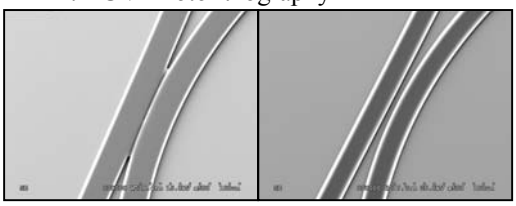

(a) (b)

FIG. 1 SEM image of UV exposure (a) without UV filter at 30 s and (b) with UV filter at 35 s for 2µm gap

ii. Electron Beam

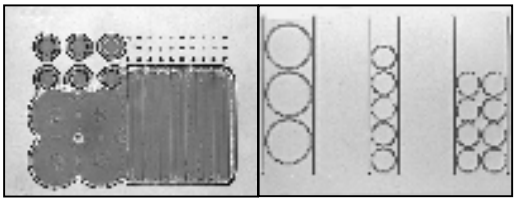

(a) (b)

FIG. 2 Microscope image of electron beam dose test (a) 50µC/cm^2 and (b) 2.5µC/cm^2

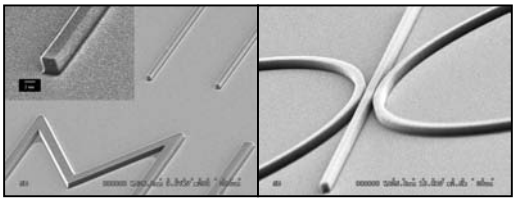

(a) (b)

FIG. 3 SEM images of (a) SU8 2µm x 2µm waveguide (inset shows smooth sidewall), and (b) microring resonator with 200 nm of gap

C. Propagation Losses

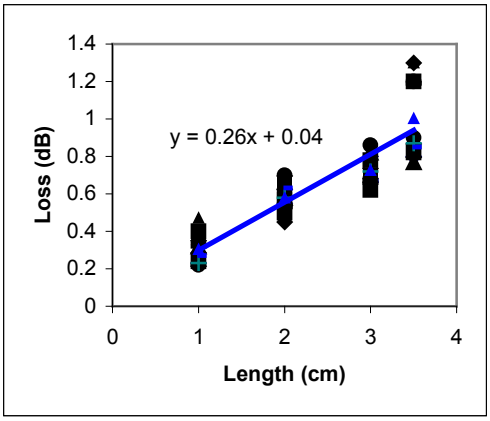

FIG. 4. Loss dependence of waveguide as a function of length at 638.2nm wavelength.

The propagation losses were obtained to be approximately (0.26 ± 0.04) dB/cm at 632.8 nm for SU8 waveguide dimension of 2µm x 2µm.

D. Bending Losses

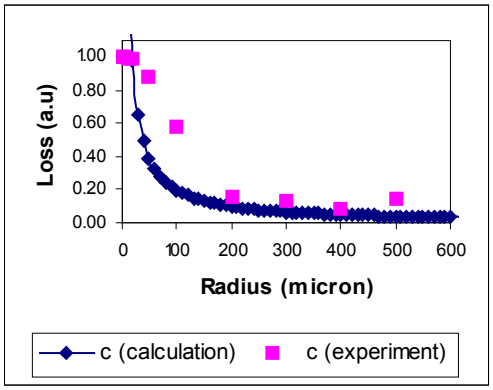

FIG. 5. Loss dependence of waveguide as a function of ring radius

The comparison of experimental results with calculation [4] shows relatively good agreement, when the radius is smaller than 100µm, the bending losses exponentially increased.

IV. CONCLUSION

In conclusion, we have demonstrated UV photolithography and electron beam methods for SU8 polymer fabrication. The exposure time for UV photolithography was 35 s using the UV filter. The fabrication dose for electron beam was 2.5µC/cm^2. Furthermore, we show these waveguide have a low propagation loss around 0.26 dB/cm at 632.8nm and the bending losses were more than 50% if the ring radius is lower than 100µm.

V. ACKNOWLEDGMENT

We wish to acknowledge the James Watt Nanofabrication Centre (JWNC) staff for the clean room facilities. We should also like to acknowledge partial financial support from International Islamic University Malaysia (IIUM), Gombak, Selangor, Malaysia and Ministry of Higher Education Malaysia (MOHE).

REFERENCES

[1] M. Nordstrom, D. A. Zauner, A. Boisen, and J. Hubner, "Single-mode waveguides with SU-8 polymer core and cladding for MOEMS applications," *Journal of Lightwave Technology*, vol. 25, pp. 1284-1289, 2007.

[2] C. Y. Chao, W. Fung, and L. J. Guo, "Polymer microring resonators for biochemical sensing applications," *Ieee Journal of Selected Topics in Quantum Electronics*, vol. 12, pp. 134-142, 2006.

[3] U. Levy, K. Campbell, A. Groisman, S. Mookherjea, and Y. Fainman, "On-chip microfluidic tuning of an optical microring resonator," *Applied Physics Letters*, vol. 88, pp. -, 2006.

[4] Marcatil.Ea, "Bends in Optical Dielectric Guides," *Bell System Technical Journal*, vol. 48, pp. 2103-&, 1969

OVERCOMING THE LIMITATIONS OF TRADITIONAL EEG ACQUISITION THROUGH THE USE OF CAPACITIVE ELECTRODES

Anthony J. Portelli and Slawomir J. Nasuto
CIRG, School of Systems Engineering, University of Reading, RG6 6AY
Siu05ajp@reading.ac.uk

Abstract - This paper describes the design of a Data Acquisition (DAQ) system in the form of a single channel capacitive Electroencephalograph (EEG) sensor suite comprising hardware and software modules. Through the use of Titanium Oxide (TiO_2) coated Stainless steel discs, it has been possible to detect human bio-potentials without charge contact thus eliminating any potential safety risks involved with the use of bio-potential signal measurement. In this paper the capacitive interface has been successfully demonstrated. Further development will assess the quality of signals from within the human body obtained using the capacitive electrodes.

I. INTRODUCTION

One of the important tools the Electroencephalogram (EEG) is used in the identification and characterisation of neurological disorders such as epilepsy and encephalitis.

However traditionally used resistive electrodes require a good electrical interface, mediated by the application of an electrolytic gel. This converts ionic current flow in the skins surface, into an electron flow which can then be detected by an electronic amplifier [1].

Additionally before this gel is applied the subject's skin is normally abraded at the relevant sites to reduce skin impedances, a painful procedure if repeated, making preparation an inconvenient and lengthy process. The gel used also suffers from viscosity changes when in contact with the heat of the human body and dries out with exposure to air. These problems cause artefacts and can alter the results of the EEG. One of the implications this has is the restriction on recording time.

Capacitive sensors are not the only proposed solution, alternate sensors for the recording of bio-potentials include resistive Active electrodes [2] and Super-conducting Quantum Interference Devices (SQUID) magnetometers [3].

II. CONCEPT

Capacitive electrodes do not require real charge contact with the skin in order to detect bio-potentials [4] making them inherently safe. These electrodes detect bio-potential signals via the variation of charge between the skin and a conducting plate placed in close proximity.

III. SENSOR HARDWARE IMPLEMENTATION

A common problem with the selection of electrode material remains the issue of bio-compatibility, which is whether or not a material performs without ill or toxic effect in a specific setting, in this case external contact with a subject's skin. Stainless steel was chosen as the electrode plate conductor. Grade 304 (the most common grade of stainless steel) was utilised as the plate material. It was chosen due to its bio-compatibility, wide usage, low cost and favourable conductivity when compared against other materials. To achieve the capacitive effect the discs had to be coated with a dielectric. Titanium Oxide (TiO_2) was chosen as the dielectric as it would not only be resistant to corrosion in contact with sweat but also provide acceptable electro-chemical properties [5].

$$C = \frac{\varepsilon_r \varepsilon_0 A}{d} \quad (1)$$

Formula 1 shows a capacitor model formula, where C is the capacitance, ε_r is the relative static permittivity constant of insulating dielectric, ε_0 is the permittivity of free space, A is the surface area of the plates and d is the distance of separation of the plates. This formula can be used to estimate the amount of capacitive coupling present between a subject's skin and an electrode.

A 1µm layer of Titanium Oxide with a 100ηm adhesion layer of Titanium was selected to allow a sufficiently thick layer to withstand intense use and provide a strong capacitive coupling. Using the capacitor model, equation 1, the approximate amount of capacitive coupling that could be achieve by an electrode of diameter 1cm.

$$C = \frac{114 \text{ x } 8.85 \text{ x } 10^{-12} \text{ x } 0.005^2 \text{ x } 3.14}{1 \text{ x } 10^{-6}} = 79.2\text{nF} \quad (2)$$

Other calculated capacitive couplings are much smaller than for these electrodes [6]. This would indicate that the TiO_2 coated electrodes would perform with an increased signal to noise ratio. This does assume constant mechanical contact with the electrode face

IV. RESULTS

When the unit was designed it was assumed that there would be a large quantity of environmental noise that could contaminate the signal. Unfortunately this proved to be accurate based on the initial prototype.

The first tests of the unit performed with an unacceptably low signal to noise ratio characterised by the strong peak at 50Hz present in the power spectrum.

Figure 1 illustrates, in addition to the 50Hz component, a secondary peak at 4Hz shown more clearly in figure 2. This second peak was the result of the capacitive inducing of a sine wave signal from a function generator. The signal generator and electrode circuitry at

no point shared a common ground. This and other tests demonstrate the capacitive coupling of the system, proving the interface.

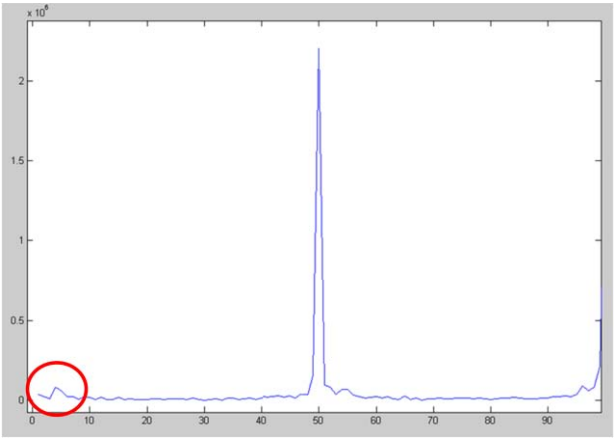

Frequency (Hz)

Figure 1. Shows that strongest peak at 50Hz from "line noise" interference

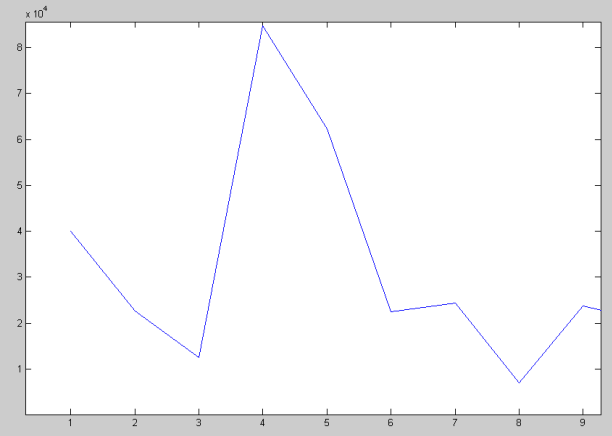

Frequency (Hz)

Figure 2. Shows the 4Hz Peak in the power spectrum more clearly

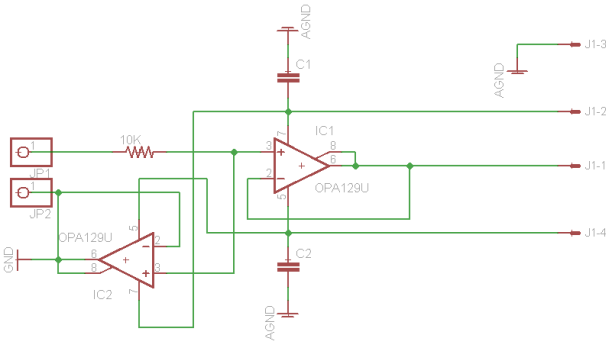

Figure 3. New electrode circuitry

Despite the ability to capacitively couple known signals to the electrodes, the system has at present been unable to acquire bio-potentials, most likely due to the fact that the signal to noise ratio is so low and therefore any useful signal is lost in noise.

New electrode circuitry has recently been developed, shown in figure 3, whose signal to noise ratio is of a much highly level and should soon prove able to detect bio-potentials. This circuitry provides a second operational amplifier to "guard" or actively shield the electrode environment aiding in attenuation of the environmental noise.

V. CONCLUSION AND FUTHER WORK

In the future work will be concentrated on the increase in the signal to noise ratio of the detected signals as well as reduction of the noise floor.

Testing of the new prototype electrodes will take priority whilst solving other problems with the system. The power consumption of the systems requires improvements as it is too high for battery operation. In addition, at present the hardware requires both a USB port and a Serial port (for power and data transfer). Extension to the full speed USB protocol was implemented it would be both more efficient and would allow for the addition of more channels.

Acknowledgement: The author would like to thank Paul Minchinton for his good natured but unwavering cynicism even in face of tangible results. The author would also like to extend his thanks to the New Scotland University Thin Film Centre.

VI. REFERENCES

[1] C.J.Harland, T.D.Clark, R.J.Prance, *Electric Potential Probes - new directions in the remote sensing of the human body.* Measurement Science and technology, 2002. **13**: p. 163-169.

[2] T.Degen, S.Torrent, H.Jackel, *Low-Noise Two-Wired Buffer Electrodes for Bioelectric Amplifiers.* IEEE Transactions on Biomedical Engineering, 2007. **54**(7): p. 1328-1332.

[3] J.P.Wikswo, *SQUID magnetometers for biomagnetism and nondestructive testing: important questions and initial answers.* IEEE Transactions on Applied Superconductivity, 1995. **5**(2): p. 74-120.

[4] A.Ueno, Y.Uchikawa, M.Noshiro. *A Capacitive Sensor System for Measuring Laplacian Electromyogram through cloth: A Pilot Study*. in *Annual International Conference of the IEEE EMBS* 2007. Cite Internationale, Lyon France.

[5] C.Fonseca, J.P.Silva Cunha, R.E.Martins, V.M.Ferreira, J.P.Marques, M.A.Barbosa, Martins da Silva, *A Novel Dry Active Electrode for EEG Recording.* IEEE Transactions on Biomedical Engineering, 2007. **54**(1): p. 162-165.

[6] Furusawa, Yoichi. *Low Invasive Measurement of Electrocardiogram for Newborns and Infants*. In *Asian-Pacific Conference on Biomedical Engineering*. 2003. Japan.

MOTORS AND MAGNETISM – NEW METHODS IN THE CHARACTERIZATION OF BACTERIAL FLAGELLAR MOTORS

A. D. Karenowska[1†], R. M. Berry[1] and J. F. Gregg[1],

[1]Department of Condensed Matter Physics, Clarendon Laboratory, University of Oxford, Oxford, UK

[†]corresponding author, a.karenowska@physics.ox.ac.uk,

Abstract – Bacterial flagellar motors (BFMs) are tiny – yet remarkably powerful – rotary machines which decorate the cell membranes of certain swimming bacteria. Gathering information about their torque-speed characteristics provides important clues about their underlying operating principles. Two methods for characterizing BFM torque-speed relationships are widely used, but both have significant shortcomings. In this paper we report the demonstration of instrumentation capable of exercising quantitative magnetic control over the *Escherichia coli* (*E. coli*) BFM. The powerful 'magnetic tweezers' we have developed promise exciting new insight into motor structure and operation, and major practical advantages over conventional torque-speed data gathering techniques.

I. INTRODUCTION

Several species of bacteria are equipped with tiny rotary propulsion units known as 'bacterial flagellar motors' (BFM). Each motor comprises two parts: a 'stator' embedded in the bacterial cell wall and a rotor connected to a long external filament or flagellum (Fig. 1). The bacteria 'swim' through rotation of the corkscrew-like flagella [1].

The BFM is a truly 'high performance' miniature power plant; just 50nm across, its power-to-weight ratio is at least equivalent to that of an absolute state-of-the-art internal combustion engine.

Probing the structure and operating characteristics of the BFM not only promises fascinating insight into the elegant complexity of the natural world, but has significant implications for man-made micro- and nano-scale systems and biosystems engineering. The BFM may unlock the door to wholly new types of sensors, drug delivery systems and information processing technologies.

The structure of the BFM is too small and complex to be analysed directly, but – to an extent – its components and their function can be inferred through analysis of its speed-torque characteristics.

II. TECHNICAL INFORMATION

Methods

Several types of rotary bacterial flagellar motor exist, one of the most important – and the subject of this paper – is that of *Escherichia coli* (*E. coli*). *E. coli* is a sausage-shaped bacterium, with a minor diameter of around 1μm and an aspect ratio of ~ 3:1. Its motor units (~4-6 are typically present on each bacterial cell) have a diameter of 50nm (Fig. 1). The flagella are protein stalks 6-10μm in length. The *E. coli* BFM is known to be powered by an ion flux (Na^+ or H^+) down an electrochemical gradient present across the cell's cytoplasmic membrane. The electrochemical gradient – also known as the 'proton-motive force' (pmf) or 'sodium-motive force' (smf) according to the driving ion – has two components: a transmembrane voltage, and a concentration difference across the membrane. The ion channel through the stator is triggered by the motion of the rotor, and torque is thought to be delivered via conformal changes in the stator brought about by ions moving on and off its constituent protein subunits. However, the detail of the pmf/smf to torque conversion mechanism is not well understood [2].

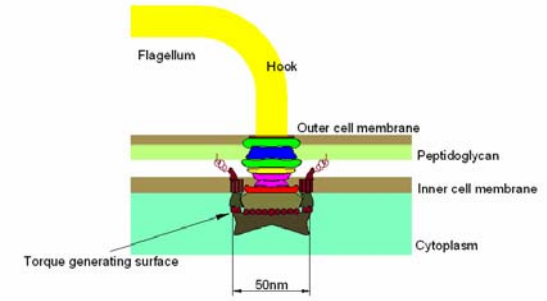

FIG. 1. A schematic representation of the key structural elements of the bacterial flagellar motor. The unit comprises a 'stator' embedded in the envelope of the cell and an extracellular helical flagellar rotor around 10 um in length. A soft elastic linkage or 'hook' exists between the motor and the flagellum.

Two methods for characterizing BFM torque-speed relationships are well-reported in the literature. The first involves shearing a motor's flagellum to around one tenth of its full length, sticking the host cell body to a glass cover-slip, and fixing a polystyrene bead to the flagellar stub. The rotational speed of the bead is then monitored by a weak optical trap and the viscosity of the medium in which it is rotating varied. Alternatively, the viscosity η may be fixed, with the bead radius R as the variable. In either case, the torque can be

inferred from the Stokes formula for the drag D acting on the bead: $D = 6\pi\eta R$ [2-4]. The second method is electrorotation. In this technique, the flagellum is left intact and it – rather than the host cell – is used as an anchor. A high-frequency circulating electric field rotates the cell body and the rate of rotation is measured optically. The motor torque can then be inferred from a force balance on the motor [2]. Neither of these techniques is particularly satisfactory. In both cases, gathering torque data for a range of motor speeds can only be achieved by comparative studies of several motors. Consistent motor behaviour across a range of assays is a pre-requisite assumption, but not necessarily a valid one. The range of load torques is limited, and experiments are challenging and laborious.

Against this background we have proposed and demonstrated a new 'magnetic trap' technique, an extension of similar techniques used to investigate F_1-ATPase and protein machines that work on DNA [5-6]. The key component of the instrumentation is a purpose-designed 'magnetic trap' operating in conjunction with specially prepared *E. coli* BFMs with magnetically tagged flagella.

Results

We have successfully attached latex encapsulated super-paramagnetic microspheres of varying diameters (~0.5-1μm) to the sheared, free flagellar stubs of Na^+-driven chimaeric BFMs and – via purpose-designed magnetic trap – demonstrated an ability to progressively load individual motors to stall over a wide range of speeds (0 to >100Hz) (Figs. 2-3). The magnetic trap uses a four-pole electromagnet (together with control circuitry) to provide a rotating magnetic field in the vicinity of the magnetically tagged flagella. Both the strength and the frequency of the magnetic field are variable.

Torque-speed data from calibrated experiments is expected shortly.

Discussion

With a) knowledge of the current-field profile of the magnetic trap and b) calibration of individual magnetic beads, we anticipate being able to recover fast, quantitative information about the torque-speed characteristics of individual BFMs over a range unattainable with conventional techniques.

Future work will include the development of a closed-loop experimental system in which the real-time angular position of the BFM – obtained via focal back-focal-plane (BFP) interferometry – will be used as a feedback

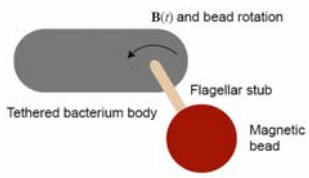

FIG. 2. The 'magnetic trap' applies a torque to the BFM via a rotating magnetic field coupled to a super-paramagnetic tag attached to a sheared flagellum. The body of the bacterium is tethered to a glass cover-slip.

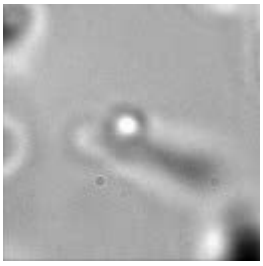

FIG. 3. In the image above, the bright sphere is a super-paramagnetic particle ~ 1μm in diameter tethered to the flagellar stub of a sodium-driven BFM. The host cell is tethered to a glass cover-slip.

signal to control the strength and frequency of the magnetic trap [7].

III. CONCLUSION

In summary, sophisticated magnetic control of the sodium-driven *E. coli* flagellar motor has been demonstrated. Preliminary 'load-to-stall' experiments show the potential of our magnetic trapping technique to provide heretofore unattainably detailed, quantitative information about the torque-speed relation and power-torque conversion mechanisms particular to this and other rotary molecular motors.

REFERENCES

[1] A. D. T. Samuel and H. C. Berg, *Torque-generating units of the bacterial flagellar motor step independently*, J. Biophys. vol.71, 1996, pp. 918-923.

[2] J. Xing, F. Bai, R. M. Berry and G. Oster, *Torque-speed relationship of the bacterial flagellar motor*, PNAS, vol.103(5), 2006, pp. 1260-1265.

[3] K. C. Neuman and S. M. Black, *Optical trapping*, Rev. Sci. Instrum., vol.75(9), 2004, pp. 2787-2809.

[4] T. Pilizota, T. Bilyard, F. Bai, M. Futai, H. Hosokawa and R. M. Berry, *A programmable optical angle clamp for rotary molecular motors*, J. Biophys., vol.93, 2005, pp. 264-275.

[5] Y. Rondelez, G. Tresset, T. Nakashima, Y. Kato-Yamada, H. Fujita, S. Takeuchi and H. Noji, *Highly coupled ATP synthesis by F_1-ATPase single molecules*, Nature, vol.443, 2005, pp. 773-777.

[6] S. B. Smith, L. Finzi and C. Bustamante, *Direct mechanical measurement of the elasticity of single DNA molecules by using magnetic beads*, Science, 258, 1992, pp. 1122-1126.

[7] Y. Sowa, A. D. Rowe, M. C. Leake, T. Yakushi, M. Homma, A. Ishijima and R. M. Berry, *Direct observation of steps in rotation of the bacterial flagellar motor*, Nature, vol.436, pp.916-919.

A NOVEL WEARABLE MEDICAL DEVICE FOR CONTROLLING URINARY INCONTINENCE BY CONDITIONAL NEUROMODULATION

N.A. Edirisinghe[1]; B. Leaker[2]; J. Susser[3]; M. Al-Mukhtar[3]; N. Donaldson[1]; M.D. Craggs[3]

[1] Department of Medical Physics and Bio-engineering, University College London.
[2] Nephro-Urological Clinical Trials Ltd, Queen Anne Street Medical Centre, London.
[3] Neuro-spinal Research Centre, Division of Surgery & Interventional Science, University College London & London Spinal Cord Injuries Centre, Royal National Orthopeadic Hospital, Stanmore.

nedirisi@medphys.ucl.ac.uk,

Abstract - Urinary incontinence in spinal cord injured (SCI) persons is mainly due to neurogenic detrusor overactivity (NDO). This novel device worn in the anal canal transrectally stimulates the pudendal nerve when electromyograpic (EMG) activity of the sphincter is detected. Sphincter EMGs were recorded through the device during standard urodynamics with and without conditional neuromodulation (CN) in six SCI subjects with NDO. In all subjects CN suppressed NDO resulting in a significant increase (P=0.001) in bladder capacity from 115ml to 380ml and reduction in bladder pressure. This novel wearable CN device prevents incontinence by suppressing NDO; increasing bladder capacity by 240%.

I. INTRODUCTION

Urinary incontinence is a major medical and social problem in the UK affecting one in twenty of the population across all ages. In spinal cord injuries (SCI) incontinence is caused by neurogenic detrusor (bladder muscle) overactivity (NDO) with sphincter dyssynergia. NDO can be suppressed using drugs which also improves bladder capacity. However, these drugs have some bothersome side-effects. The aim of this research was to develop and test a novel wearable device designed to replace drugs for overactive bladders by stimulating the pudendal nerve electrically on demand [1]. This technique is known as conditional neuromodulation (CN).

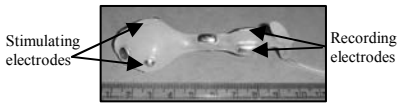

FIGURE 1
THE BLADDER CONTROL DEVICE, WHICH IS MADE OUT OF SOFT MEDICAL-GRADE SILICONE RUBBER WITH TWO ELECTRODES RECORDING SPHINCTER ELECTROMYOGRAM (EMG), TWO BILATERAL PAIRS OF ELECTRODES FOR TRANSRECTAL STIMULATION OF THE PUDENDAL NERVE AND A GROUND ELECTRODE ALL FABRICATED FROM MEDICAL-GRADE STAINLESS STEEL.

The device detects electromyogram (EMG) of the pelvic sphincter muscles during NDO. The EMG is electronically processed to produce a signal for automatically triggering electrical stimulation of the pudendal nerves transrectally. The stimulation suppresses the bladder resulting in increased capacity. This technique is known as conditional neuromodulation [2]. It also contracts the urinary sphincter to prevent leaking (Figure 2).

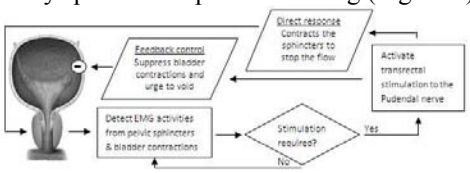

FIGURE 2
ELECTRODES DETECT EMG SIGNALS FROM THE ANAL SPHINCTER, ACTING AS A SURROGATE FOR THE URINARY SPHINCTERS. THIS SIGNAL IS PROCESSED AND WHEN IT EXCEEDS THE PREDETERMINED THRESHOLD, ACTIVATES STIMULATION OF THE PUDENDAL NERVES TO SUPPRESS THE BLADDER AND TO CONTRACT THE SPHINCTERS.

II. METHODS

With ethics committee approval and informed consent, six spinally injured male patients aged 18-75 with NDO were tested using the device placed in the anal canal (Figure 3).

FIGURE 3
THE DEVICE WAS WORN IN THE ANAL-RECTAL CANAL FACING THE ANTERIOR POSITION. ANAL ELECTRODES DETECTED EMG ACTIVITY FROM THE SPHINCTERS AND OTHERS FOCUSSED ON THE PUDENDAL NERVES BILATERALLY TO DELIVER ELECTRICAL STIMULATION TRANS-RECTALLY.

A standard cystometrogram (CMG) at 60ml/min was performed by recording bladder pressure (Pves), rectal pressure (Pabd) and the difference, detrusor pressure (Pdet). The EMG of the anal sphincter was recorded through the device. The sensory thresholds for stimulation through the device were also obtained. Software was pre-programmed to activate stimulation (200μs pulses for 1min at a frequency of 15 Hz), when the rectified-smoothed EMG exceeded a pre-determined threshold associated with a bladder pressure rise of 20cmH_2O. The statistical values of

difference of the change in maximum bladder pressure and bladder capacity compared with controlled were determined by the Wilcoxon signed-ranked test.

III. RESULTS

All six patients showed successful conditional neuromodulation of bladder overactivity and automatic contraction of their sphincters. (Figure 4) shows typical results from one subject (AA).

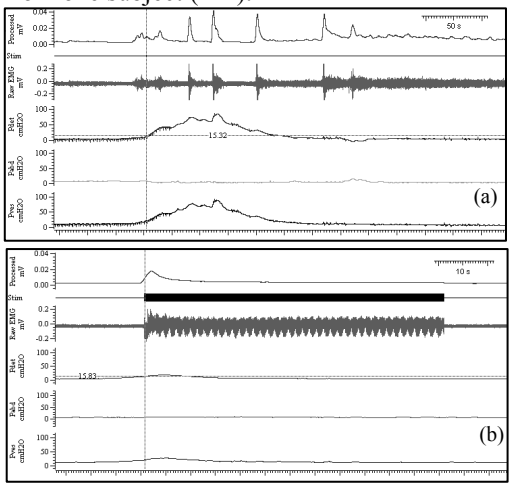

FIGURE 4

Pves, Pabd and Pdet represent the bladder, abdominal and detrusor pressure respectively. EMG of the anal sphincters represents in "Raw EMG" and the waveform use for triggering is filtered, rectified, smoothed EMG shown as the "processed" signal. (a) shows NDO contraction; (b) shows neuromodulation through the device using EMG threshold of 6μV in the processed signal to trigger the stimulation while filling the bladder at 60ml/min.

Using a more physiological bladder filling rate of 10ml/min it was demonstrated that repeated automatic conditional neuromodulation (Figure 5) enhanced bladder capacity by between 180%- >300% across the 6 subjects.

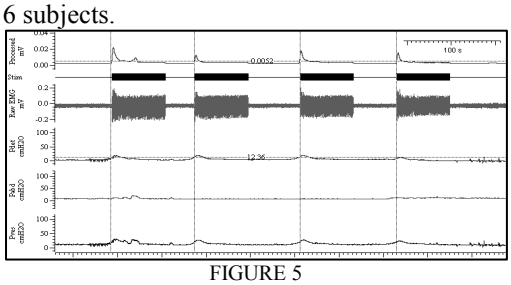

FIGURE 5

THIS SHOWS FOUR REPEATED CONDITIONAL NEUROMODULATION IN SUBJECT (AA) CONSISTENTLY SUPPRESSING NDO. AN EMG THRESHOLD WAS SET AS SHOWN IN FIGURE 4.

As a result of repeated conditional neuromodulation bladder pressure reduced and bladder capacity increased significantly (Table 1).

TABLE 1
THE SIGNIFICANT EFFECT OF NEUROMODULATION ON PVES (MAX) AND BLADDER CAPACITY.

Subject	Control P_{ves} (max) (cm of H_20)	P_{ves}(max) with stim. (cm of H_20)	Control bladder capacity (ml)	Bladder capacity with stim. (ml)
RG	72	13	110	418
BB	120	17	128	358
ES	147	46	105	331
CC	60	29	115	333
PK	83	57	87	381
AA	89	27	150	500
Mean	95.2	31.5	115.8	386.8
S.D.	29.6	15.5	19.6	58.7
P-val.	**≤0.001**		**≤0.001**	

IV. DISCUSSION

In the instances shown in figure 5, the EMG threshold level proved to be a reliable source for triggering stimulation. When it crosses the threshold the stimulation activated and NDO suppressed in less than 4s.

The threshold level for triggering stimulation varies on each individual. Furthermore for a given SCI subject few repetitive measurements will be required in deciding the threshold level in order to avoid false and missed triggering.

V. CONCLUSION

This paper describes the utility of a novel and wearable CN device for suppressing NDO automatically. Bladder suppression began within 5s of conditional neuromodulation in all subjects and sphincter contractions occurred almost immediately to prevent leakage. Repeated conditional neuromodulation significantly increased bladder capacity across all subjects reducing the number of catheterisations for bladder emptying.

In future the device needs to be modified for a self-contained electronic circuitry, battery and external wireless communication link. Furthermore the regulatory requirement for a medical device and CE marking needs to be obtained.

REFERENCES

[1] CRAGGS MD, (WO/2007/101861), "NEUROMODULATION DEVICE FOR PELVIC DYSFUNCTION", PATENTS. 6 MARCH, 2006.

[2] CRAGGS MD, MCFARLANE J, "NEUROMODULATION OF THE LOWER URINARY TRACT", EXPERIMENTAL PHYSIOLOGY, VOL. 84(1), JAN. 1999, PP. 149-60.

POWER HARVESTING FROM HEAD MOTION FOR COCHLEAR IMPLANTS

R. Saba, S. Wang, O. N. Baumann, S. J. Elliott

Institute of Sound and Vibration Research, University of Southampton, UK

rs1604@soton.ac.uk

Abstract – Fully implanted cochlear implants require an independent power source for which head motion provides a suitable candidate. To utilise this source, an inertial electromagnetic device is required to convert mechanical energy into electrical power. This paper explores the feasibility of such a device and its best configuration to respond to the broadband excitation from head motion. Single and multiple frequency excitations in six axes of motion (linear and rotational) are considered. The power is shown to be proportional to a cube of the excitation frequency and possible to achieve at a level of 150 μW.

I. INTRODUCTION

A fully implantable cochlear implant requires an internal self maintained power source. Head motion provides an easy, local power source for this application in which an inertial device (most likely electromagnetic) converts the mechanical energy into electrical energy. To achieve maximum power, an understanding is important of the frequency content of walking where source amplitudes are much greater than the size of the device. One approach is to tune this device to a specific frequency (fundamental or a harmonic). Another is to heavily damp the device in order to take advantage of a broad bandwidth. In the experiment the device was mounted just behind the ear near to where it would be implanted. Power generated at the fundamental and harmonic frequencies are calculated in order to establish the best configuration for maximum power. The power required is around 150 μW [1].

II. DYNAMICS OF AN INERTIAL HARVESTING DEVICE

Theory

Linear and rotational motion were investigated and it was found that although in rotational motion there is no limit on the throw of the device, linear motion produced most energy in the z direction (up and down).

This prediction is governed by the following result:

$$W = \rho A \omega_d^3 l^4 / 16 \qquad (1)$$

The equation shows that power increases proportionally with amplitude A, density ρ, fourth power of the device's characteristic length l and a cube of the frequency of the vibration ω. This was derived for the following system:

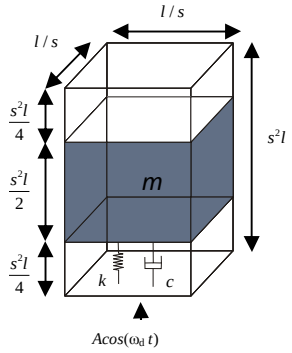

Figure 1. Inertial harvesting device s is the shape factor and k and c are the stiffness and damping of the system respectively.

The efficiency of this system is defined as

$$E = \frac{F}{4+2F} \qquad (2)$$

Where F is a non-dimensional transduction coupling factor and this has to be at a maximum for maximum efficiency (i.e. as large of a magnet and as many coils as possible with a minimum damping and resistance) therefore equation (2) becomes a half. Hence, this limits efficiency at 50%.

Power available

The power available using data from [2] is calculated assuming the device is tuned to the fundamental frequency. The device length l has to be small to be implanted and at around 1.6 steps/s, the power predicted is around 60 μW for a 1 cm^3 device. This is encouraging but higher frequency information was required and so an experiment was conducted in order to obtain higher harmonic data. This used a tri-axial accelerometer and a treadmill on which one subject walked or ran (Figure 2) at velocities similar to the data [2] from 1 to 2.7 steps/s. The power spectral density of the motion in Figure 3

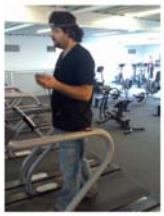

Figure 2. Subject walking with accelerometer strapped to the head taken from [3].

shows a peak at the fundamental frequencies and peaks at the harmonics of this velocity.

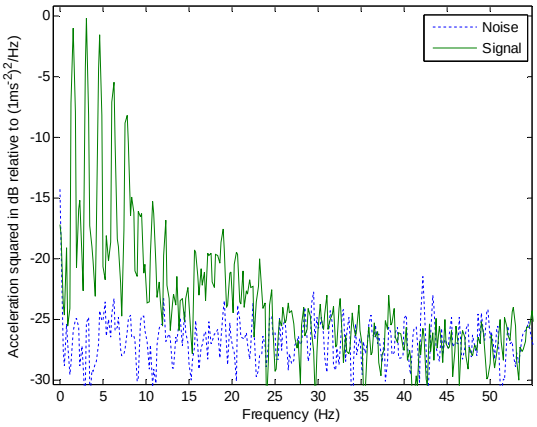

Figure 3. Power spectral density of vertical head acceleration at a walking speed of about 1.6 steps per second on the treadmill taken from [3].

The peaks gradually decrease but an increase in frequency is favoured over power at that peak and hence amplitude of motion as demonstrated by the cubed frequency term in equation 1. For the same speed at 1.6 steps/s it was predicted that most power was available from a single harmonic if the device was tuned to the 3rd harmonic (4.7 Hz) in that motion. This generated around 100 µW which is more than at the fundamental. The subject also walked normally over a longer distance to get a more average walking speed result, and this provided further encouraging results of around 460 µW.

While results are within the order required, the device is tuned to a specific frequency and if the subject walks at any speed deviating from that frequency the response will drop sharply. For this reason, further study into harvesting from multiple harmonics was conducted and Figure 4 shows how the power available changes with tuning frequency.

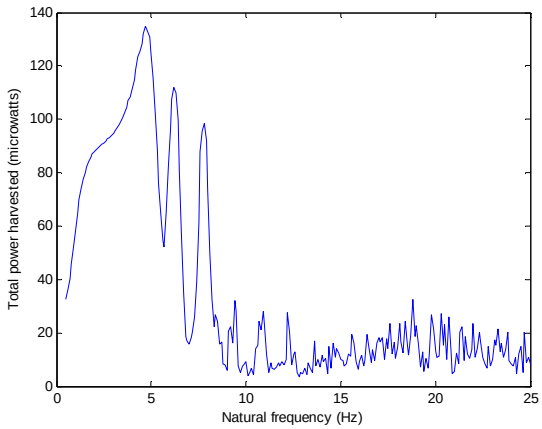

Figure 4. Graph showing power harvested from all frequencies against tuned frequency for 1.6 steps/s.

It can be noted from the above figure that as tuned frequency increases, the sharpness of the peaks increases. This figure also implies that maximum energy is available at the 3rd harmonic (4.7 Hz) giving almost 140 µW. This required a damping ratio of about 0.2 which would mean the device is less sharply tuned but it would still be unable to respond to any changes in speed of more than 10%.

III. DISCUSSION

The results indicate that a balance must be achieved between frequency bandwidth and power. Higher frequencies would deliver a higher energy levels but the practicality of this approach is limited. It is perhaps a more practical solution if one were to adopt a lower tuning frequency. This would yield lower power levels but at the same time broaden the sensitivity bandwidth of the device. The device would harvest power from multiple frequencies and its sensitivity to changes in speed would drop. This essentially allows users to walk normally and at their own comfort.

Also, the more over-damped the system is (and the lower the tuning frequency) the more power is available due to availability of other harmonics compared with the power generated if the source only had frequency components at that frequency.

IV. CONCLUSION

The purpose of the paper is to explore the maximum power available in the most practical scenario. Initially, it was believed that a higher tuned frequency would deliver more power. Its sharp tuning proved to be a problem. In order to achieve a device that works well at a wide range of walking speeds and responds significantly to all harmonics in head motion, an over-damped system is most practical.

REFERENCES

[1] W. Germanovix, and C. Toumazou. “Design of a micropower current-mode log-domain analog cochlear implant”, IEEE Transactions on Circuits and Systems Ii-Analog and Digital Signal Processing, vol.47(10), 2000, pp. 1023-1046.

[2] P. D. Woodman, and M. J. Griffin, “Six axes of head acceleration during ambulation”, Inter-Noise 96 - the 1996 International Congress on Noise Control Engineering, 25Th Anniversary Congress - Liverpool, Proceedings, Books 1-6 - Noise Control - the Next 25 Years, 1996, pp. 1719-24.

[3] R.Saba. "Motional Power Sources for Cochlear Implants." Diss. ISVR, 2007.

PATTERN CLASSIFICATION OF TONGUE MOVEMENT EAR PRESSURE SIGNAL BASED ON WAVELET PACKET FEATURE EXTRACTION

K.A. Mamun[1], M. Mace[2], M. E. Lutmen[1], R. Vaidyanathan[2], S. Wang[1]

[1]ISVR, University of Southampton, Southampton, UK, [2]Mechanical Engineering, University of Bristol, Bristol, UK

sy.wang@soton.ac.uk, r.vaidyanathan@bristol.ac.uk

Abstract – Tongue movement has been suggested as a means for paralysed patients to control equipment. The objective of this paper was to classify patterns of tongue movement monitored by ear cannel pressure changing. In order to improve classification performance with short training sets and low signal to noise ratio, features were extracted using wavelet packet transformation. The results showed that feature extraction based on wavelet packet significantly improved the classification rate from 78% to 88% when signal to noise ratio was low. The computation time has been reduced as well.

I. INTRODUCTION

We have previously introduced a novel hands-free human machine interface system, which detects and classifies tongue movement monitored by air pressure changing within the aural cavity of the ear canal [1-2]. The system may enable patients with limited movement due to stroke, quadriplegia or arthritis to interface with their environment by controlling peripheral equipments ranging from mechanical assistive devices, lights, television, prosthetic aids to computers. By using matched filter methods, correct classification of four types of tongue movements was able to achieve 86.5%. A decision fusion algorithm increased the classification rate to 97% [1]. To remove noise in real environment, varied traditional filters and wavelet thresholding method were used previously [2]. The other challenge in real environments is that there are only limited training sets available and a classification algorithm with high robustness is necessary. In this paper, we applied a wavelet packet transform to extract features of tongue movement ear pressure (TMEP) signals with limited training sets and low signal to noise ratio (SNR).

II. TMEP SIGNAL ACQUISITION AND CLASSIFICATION

A microphone-earpiece was inserted into the ear canal and the pressure change in the aural cavity was recorded by the microphone when the tongue moved in four directions (Figure 1a), which were up (U), down (D), left (L), and right (R) in random order [1]. The action in each direction was repeated 100 times in total and the signals were sampled at 2 kHz. As external interference may merge with TMEP signal in real life situation, it was simulated by adding babble noise to the recorded TMEP signals at 0dB SNR in this study (Figure 1b). Recordings were made from five subjects. The experiment was approved by the local research ethics committee.

The occurrence of each action was detected by setting a threshold for the energy level of TMEP signals. Then a data segment of 512 points was extracted and normalised by standard deviation. All 100 data segments in each action were aligned together using pair-wise cross-correlation. Four data segments were randomly selected out of 100 segments as a training set and averaged to generate a template for each action. Other data segments were used as a test set. Four templates and four test sets were generated for classification. Each segment from one test set was aligned to the four templates using cross-correlation. The pattern was classified as the action whose template had the minimum Euclidean distance from the data segment, which is

$$E_{ij} = \sqrt{\sum_{k=1}^{512} (x_i(k) - X_j(k))^2} \quad ,$$

where $x_i(k)$, i=1,2,3…96, is the i^{th} test signal and X_j(k), j=1, 2, 3, 4, is the j^{th} template.

The classification accuracy of the classifier was measured as the percentage of correct classification [1]. The above procedure was repeated twenty times and each time the templates were generated from randomly selected data segments. The classification rate was then averaged.

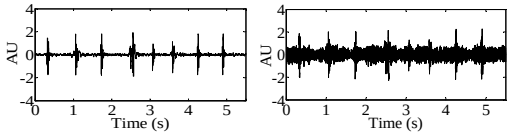

(a) (b)

Figure 1. TMEP signals were recorded during different up, down, left, right actions (a). The TEMP signals with 0dB signal to noise ratio (b).

III. WAVELET PACKET TRANSFORM BASED FEATURE EXTRATION

The discrete wavelet packet transform (WPT) provides a level by level transformation of the signal from time domain to time-scale domain [3]. The wavelet packet coefficients at one scale can be recursively decomposed into the coefficients at the next scale using a low-pass and high-pass analysing filter. To compute the WPT coefficients of scale levels i=1, … , I, we recursively filter the WPT coefficients at previous stage. Let $W_{i,j}(k)$, j=0, …, 2^i-1 to represent the WPT coefficients at level i. Then we have the following equations to compute the wavelet packet coefficients

$$W_{i,2j}(k) = \sum_{l=0}^{L-1} h(l) W_{i-1,j}(2k + 1 - l \bmod N_{j-1})$$

$$W_{i,2j+1}(k) = \sum_{l=0}^{L-1} g(l) W_{i-1,j}(2k+1-l \bmod N_{j-1})$$

Where $k = 1,\ldots, N$ and $N_j = N/2^j$. $h(l)$ and $g(l)$ are the impulse responses of scaling and wavelet filters which represents low-pass and high-pass filters, respectively. They are quadrature mirror filters and have only finite nonzero coefficients, which results in a very efficient way to compute WPT coefficients.

The TMEP data segments were transformed into WPT coefficients at scale 3 as features where a *symlet* wavelet of order 7 was used. Then the classification performance was evaluated using the templates and test sets generated from the WPT coefficients of the first frequency band according to the above procedure.

IV. RESULTS

The power spectra of four actions in the TMEP signals show dominant peaks at low frequency around 30 Hz with two separated peaks in some cases. The majority of power was below 100Hz (Figure 2). So the WPT coefficients at the first frequency band were extracted for classification, which was corresponding to 0-125Hz.

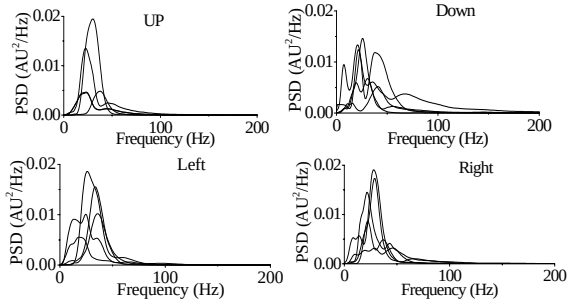

Figure 2. Average power spectral density of four actions in the TMEP signals in 5 subjects.

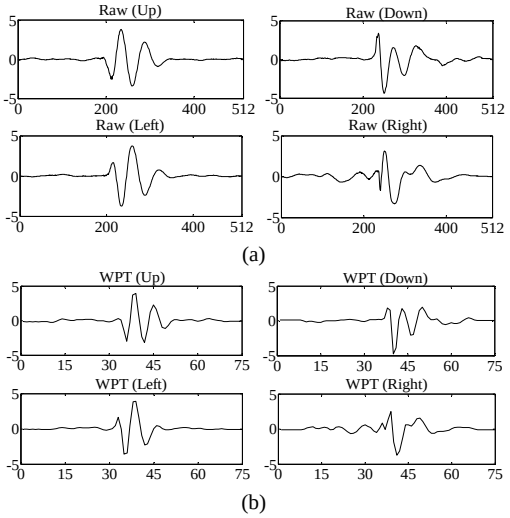

Figure 3. TMEP templates of four actions generated from raw signals (a) and WPT coefficients (b).

The templates were generated by averaging the randomly selected data segments (Figure 3a) or WPT coefficients (Figure 3b) of TMEP signals in each action. Similarly, the templates were generated from the TMEP signals with 0 dB SNR as well.

The average classification rate was 89% and there was no significant difference between two types of templates when signals were clean (Figure 4). When the signals were contaminated with noise, the performance deteriorated. Wavelet transformation improved the performance significantly.

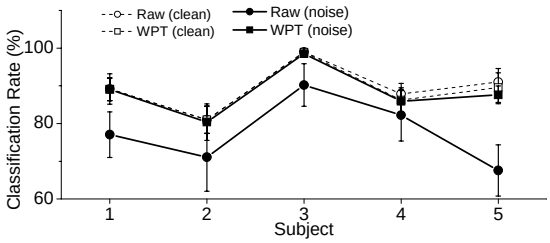

Figure 4. Average classification rate (mean ± standard deviation) when raw TMEP signals and WPT coefficients were used in clean and 0 dB SNR conditions.

V. DISCUSSION AND CONCLUSION

Tongue movement ear pressure signals have been proposed for human-machine interface control. Previously large data segments were used to generate training sets and templates. A high classification rate of 97% was achieved. When number of the training data segments decreases, performance is worsened and only 89% were correctly classified (Figure 4). The noise causes the classification rate further to be further reduced to 78%. When the classification is based on the feature extracted from WPT coefficients, the classification rate was improved to 88%. The overall computation cost is slightly reduced as well. The pattern classification of tongue movements based on wavelet packet transformation feature extraction is robust to noise. The methods developed in this study may be useful to extract features from other biomedical signals, for instance surface electromyogram [4] or deep brain local field potentials [5]. Further effort to improve the performance with limited training sets is necessary for developing a real time assistive system controlled by tongue movement ear pressure signals.

REFERENCES

[1] R. Vaidyanathan, B. Chung, L. Gupta, H. Kook, S. Kota, and J. D. West, "Tongue-movement communication and control concept for hands-free human-machine interfaces", IEEE Transactions on Systems, Man and Cybernetics Part A: Systems and Humans, vol.37(4), 2007, pp. 533-546.

[2] R. Vaidyanathan, S. Wang, and L. Gupta, "A wavelet denoising approach for signal action isolation in the ear canal", the 30th Annual International Conference of the IEEE Engineering in Medicine and Biology Society, Vancouver, Canada, August 20-24, 2008.

[3] A. Walden, "Wavelet analysis of discrete time series", Progress in Mathematics, vol.202, 2001, pp. 627-641.

[4] S. Wang, X. Liu, J. Yianni, T.Z. Aziz, and J.F. Stein, "Extracting burst and tonic components from surface electromyograms in dystonia using adaptive wavelet shrinkage". Journal of Neuroscience Methods. Vol.139(2), 2004, pp.177-184.

[5] P. Brown, C.C. Chen, S. Wang, A. Kuhn, L. Doyle, K. Yarrow, J.F. Stein, and T. Aziz, "Involvement of human basal ganglia in off-line feed-back control of voluntary movement", Current Biology, vol.16(7), 2006, pp.2129-2134.

OBJECTIVE MEASUREMENT OF PERCIEVED AUDITORY QUALITY IN HEARING AID FEEDBACK CANCELLATION SYSTEMS

A.J.Manders, D.M.Simpson, S.L.Bell

ISVR, University of Southampton, Southampton, UK

ajm105@soton.ac.uk, ds@isvr.soton.ac.uk, slb@isvr.soton.ac.uk

An approach for predicting subjective quality ratings of audio signals processed by adaptive feedback cancellers is proposed. This is based on the adaptation of existing objective quality evaluation metrics described in the literature, which hitherto have neither been formally evaluated, nor optimized for this specific application.

I. INTRODUCTION

Acoustic feedback imposes a limit on the maximum gain that may be applied by a hearing aid before instability occurs, resulting in oscillation. Adaptive feedback cancellation is an effective solution to this problem, and has become a common signal processing feature in modern hearing aid design. Adaptive feedback cancellation can increase the gain-margin of stability of a hearing aid by as much as 20 dB [1], however, maintenance of a good sound quality in this 'added stable' region of gain is desirable. Adaptive cancellers are inherently prone to entrainment, a non-linear distortion artefact produced by tonal or highly periodic signal inputs such as music. Entrainment distortion manifests as the appearance of extraneous harmonic components in the signal output, and can be bothersome to hearing aid users [2]. In addition, when entrainment occurs, the ability of the feedback canceller to remove unwanted acoustic feedback is impaired, resulting leakage of residual feedback distortion into the hearing aid output.

Owing to the expense and variability of subjective tests using human volunteers, a fully objective method of measuring the sound quality of signals processed by adaptive feedback cancellers is required. In recent years, objective signal quality assessment metrics that predict a mean subjective numerical opinion rating (MOS) [3] of a signal by human listeners, have been proposed. These algorithms commonly use perceptual auditory models (in order to simulate peripheral auditory effects such as temporal and spectral masking, and human perception of loudness and pitch), and are trained using databases of distorted audio samples and corresponding MOS ratings obtained from human subjects. Significant research of this technology has been conducted in the context of telephony and audio codec signal assessment; however, less has been achieved in the field of hearing aid signal quality assessment, and less still for quality evaluation of adaptive feedback canceller distortion. Recently developed objective audio quality estimation metrics intended for use with hearing aids include [4], [5], and [6]. Objective quality estimation algorithms originally developed for use in telephony and audio codec processing that might be suitable for assessing feedback canceller signal quality include PEAQ [7], and some techniques used in the low complexity non-intrusive quality model described by Grancharov [8]. With the exception of methods proposed by Spriet et al. in [4], none of these metrics have been evaluated for quality estimation of signals containing feedback canceller distortion artefacts, while [4] has not been used to predict subjective quality scores.

The objective of this project is to adapt or alter these metrics for this application, using a training database of distorted audio samples containing distortions characteristic of entrainment, and residual feedback leakage. The ability of these metrics to predict subjective quality of feedback canceller artefacts may then be evaluated by applying them to 'unseen' validation sets of distorted audio samples.

Subjective opinion score (MOS) data used for metric training will initially be obtained using normal hearing subjects, although at a later stage in the project, hearing impaired subjects will be used, in order to account for the effects of damage to the peripheral auditory system.

The current paper presents the experimental methods developed for objective detection of responses and some early results on evaluating these methods.

II. METHODS

Obtaining data for metric training

For the purpose of training the objective signal quality estimation metrics described in I., it is necessary to obtain an array of distorted audio samples containing varying levels of distortion. These have been created in MATLAB using a simple time-domain implementation of the CAF adaptive feedback canceller algorithm described by Spriet et al. [1]. The model also incorporates an acoustic feedback path, with a transfer function also obtained from [1]. Short, 12 second samples of music (horn, violin, trumpet) were processed by the model, which added entrainment and residual feedback distortion at the output. In order to generate an array of samples with varying levels of distortion, the intensity of the added distortion artefacts can be controlled by altering the adaptation rate of the adaptive filter (faster adaptation rates produce a greater amount of entrainment distortion, and vice versa).

In an initial experiment, the array of distorted samples will be presented monaurally to a group of 20 normal hearing subjects, who are required to rate their opinion of the sound quality on a 5-point MOS scale described by [3]. Samples containing no entrainment or residual feedback distortion are provided to subjects as a reference.

In a later development of this experiment, it is intended that a set of training data will obtained from a group of hearing impaired subjects, in order to account for impaired peripheral auditory functioning.

Peripheral auditory model

In order to assimilate peripheral auditory effects which occur naturally in the ear, a psychoacoustic model of the peripheral auditory system based on the work of Bramslow [9] will be used. This model is based on an array of overlapping band-pass filters, which simulate the auditory filters. In order to

simulate the behaviour of the peripheral ear, the widths of the simulated auditory filters in this model adapt dynamically in response to signal intensity, and can be widened to account for varying degrees of hearing impairment.

III. RESULTS

The MATLAB model of the adaptive feedback canceller has been developed and tested, by comparing its performance to commercial digital hearing aids that utilise adaptive feedback cancellers. In figure 1, the power spectrum of the model output in response to a 2KHz tone stimulus is compared to that of the output recorded from an Oticon Spirit III digital hearing aid in response to an acoustic 2KHz tone stimulus, presented at 75 dB HL. Recordings from the hearing aid were obtained via a 2cc coupler. Output signals obtained from a Prisma 2 Pro digital aid coupled to a KEMAR mannequin, using short samples of music played on a violin indicate similar processing characteristics to that of the model. The samples of sounds for testing in human volunteers are currently being generated.

IV. DISCUSSION

Figure 1 illustrates that the spectral composition of the model and commercial hearing aid responses to a tonal stimulus exhibit similar characteristics. The appearance of large numbers of extraneous harmonics in 1.b also confirms attributes of entrainment behaviour described by Freed and Soli [2]. Based on preliminary comparisons between distortion produced by the MATLAB feedback canceller model, and several commercial hearing aids using feedback cancellation, it is concluded that the artefacts produced by the model in response to tonal, and music stimuli are a reasonable representation of those produced by commercially available hearing aids.

In order to vary the level of distortion added by the model (for the purpose of producing a set of training data), a second method was considered in addition to altering the filter adaptation rate. This involved mixing the input with varying levels of white noise, in order to reduce the correlation between the input and output of the adaptive filter, and hence reduce the intensity of entrainment distortion. This approach was designed to simulate a range of distortions produced by canceller algorithms which use a pre-whitened input, in order to reduce filter adaptation bias; i.e. Spriet et al. [1]. The approach was abandoned in favour of varying the filter adaptation rate, after a review of the literature revealed that such methods do not in fact reduce or prevent filter entrainment [10].

The need for the use of a ‘perceptually relevant’ objective measure of quality, which accounts for peripheral auditory effects, has been indicated in informal pilot tests which reveal that the calculated SNR of processed audio signals does not always correlate well with subjective impressions of signal quality. This effect has been well documented [11].

V. CONCLUSION

There is a need for the development of a perceptually relevant objective quality measure for signals processed by adaptive feedback cancellation algorithms. An approach for obtaining objective predictions of subjective quality ratings of audio signals processed by adaptive feedback cancellers is proposed, based on the adaptation of a selection of existing objective quality evaluation metrics described in the literature, which hitherto have neither been formally evaluated, nor trained for this specific application. The proposed method involves the collection of a training database for these objective quality metrics, which will consist of an array of music audio samples containing varying levels of feedback canceller distortion artefacts, with a corresponding array of mean subjective opinion ratings of quality (MOS) obtained from normal and hearing impaired human listeners. The required audio samples (containing distortion) will be generated using a MATLAB time-domain model of an adaptive feedback canceller. Comparisons of the model output to several commercially available hearing aids suggest that the distortions produced by the model are a fair representation of those perceived by hearing aid users.

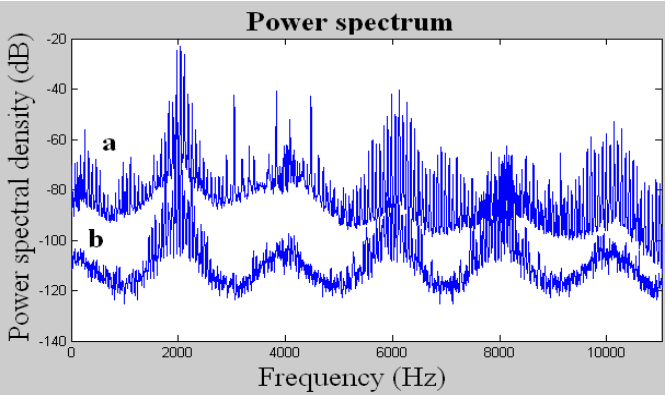

Figure 1. Welch PSD estimates of output signals of (a. commercial hearing aid (Spirit 3D) and (b. MATLAB model of adaptive feedback canceller, using a 2 KHz sinusoidal input stimulus

REFERENCES

[1] A. Spriet, G. Rombouts, M. Moonen, and J. Wouters, "Adaptive feedback cancellation in hearing aids," *Journal of the Franklin Institute-Engineering and Applied Mathematics*, vol. 343, pp. 545-573, 2006.

[2] D. J. Freed and S. D. Soli, "An objective procedure for evaluation of adaptive antifeedback algorithms in hearing aids," *Ear and Hearing*, vol. 27, pp. 382-398, 2006.

[3] "Methods for the subjective assessment of small impairments in audio systems including multichannel sound systems," ITU-R BS.1116-1, 1997.

[4] A. Spriet, K. Eneman, M. Moonen, and J. Wouters, "Objective measures for real-time evaluation of adaptive feedback cancellation algorithms in hearing aids," in *Published in the Proceedings of the 16th European Signal Processing Conference* Lausanne, Switzerland, 2008.

[5] C. T. Tan and B. C. J. Moore, "Perception of nonlinear distortion by hearing-impaired people," *International Journal of Audiology*, vol. 47, pp. 246-256, May 2008.

[6] A. Olofsson and M. Hansen, "Objectively measured and subjectively perceived distortion in nonlinear systems," *Journal of the Acoustical Society of America*, vol. 120, pp. 3759-3769, 2006.

[7] T. Thiede, W. C. Treurniet, R. Bitto, C. Schmidmer, T. Sporer, J. G. Beerends, C. Colomes, M. Keyhl, G. Stoll, K. Brandenburg, and B. Feiten, "PEAQ - The ITU standard for objective measurement of perceived audio quality," *Journal of the Audio Engineering Society*, vol. 48, pp. 3-29, Jan-Feb 2000.

[8] V. Grancharov, D. Y. Zhao, J. Lindblom, and W. B. Kleijn, "Low-complexity, nonintrusive speech quality assessment," *Ieee Transactions on Audio Speech and Language Processing*, vol. 14, pp. 1948-1956, Nov 2006.

[9] L. Bramslow, "An objective estimate of the perceived quality of reproduced sound in normal and impaired hearing," *Acta Acustica United with Acustica*, vol. 90, pp. 1007-1018, Nov-Dec 2004.

[10] L. S. Theverapperuma and J. S. Kindred, "Continuous adaptive feedback canceller dynamics," in *2006 49th IEEE International Midwest Symposium on Circuits and Systems*, San Juan, Puerto Rico, 2006, pp. 271-275.

[11] A. W. Rix, J. G. Beerends, D. S. Kim, P. Kroon, and O. Ghitza, "Objective assessment of speech and audio quality - Technology and applications," *Ieee Transactions on Audio Speech and Language Processing*, vol. 14, pp. 1890-1901, Nov 2006.

SENSORS ENHANCING SELF-MONITORING FOR PEOPLE WITH BIPOLAR DISORDER

P. Prociow[1], J. Crowe[1]

[1]Electrical Systems and Applied Optics Research Division, Faculty of Engineering, University of Nottingham, Nottingham, UK
eexpap@nottingham.ac.uk

Abstract – This paper presents sensor configurations to be used for monitoring changes in behaviour which play a vital role in managing bipolar disorder. The paper presents possible uses of both custom and off-the shelf devices in on-body and home environment monitoring.

I. INTRODUCTION

People with bipolar disorder, will in their lifetime, typically go through several episodes of manic or depressive behaviour. During such episodes a person's lifestyle and behaviour can change both rapidly and markedly leading to serious consequences. Many such people have well-developed self–awareness that is an important factor in the management of this condition with early recognition of symptoms of particular importance.

The aim of the Personalised Ambient Monitoring (PAM) project is to develop a support platform for people suffering from bipolar disorder. This platform will help patients to self monitor their mental state and also provide their care providers with accurate and informative data without compromising their privacy (at a mutually and previously agreed level). One of the key research areas of the projects is the development of a flexible sensor network providing data about patients' activities and behaviour [1].

Requirements of such sensors are that they must not compromise patients' privacy and must be simple, both to implement and to use. The sensors can be divided into two groups: wearable and environmental. Decisions on the types of sensor to be deployed were made following discussion with a clinical psychologist and other experts in this field. The first group includes those carried by the patient throughout the day. A component of this class is a mobile phone used as a sensor, data logger and communications channel. The second comprises ambient sensing units incorporated into the patients' home environments (to monitor audio environment, movement within the home, electrical appliance usage etc.).

This paper will present the sensor configurations used in the preliminary technical trial of PAM on volunteers with no history of bipolar disorder.

II. SENSORS

The target sensor configuration can be divided into two main groups: wearable and environmental. Sensors for both groups were selected based on their possible effectiveness in detecting activity changes in areas known to be influenced during the course of bipolar disorder (e.g. bed occupancy sensor for detecting lack of sleep in both depressive and manic episodes [2]). Table 1 provides example correlations made between specific bipolar episode prodromes and possible sensors.

TABLE I
EXAMPLE MANIC EPISODE PRODROMES

Prodrome	Sensors
Decreased need of sleep	• Light levels • Bed occupancy
Talkativeness / Pressure to keep talking	• Microphone • Questionnaires
Excessive and unnecessary movements	• Accelerometer • Motion sensors • Door usage sensors
Increased mobility	• GPS • Accelerometer
Excessive social activity	• GPS • Bluetooth encounters

The following paragraphs describe sensors selected for the preliminary trial in both groups.

Wearable sensors

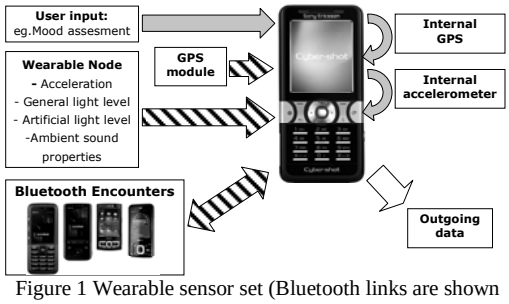

Figure 1 Wearable sensor set (Bluetooth links are shown with striped arrows).

As seen in fig. 1, the main element of the wearable sensor set is a mobile phone capable of: connecting to local RF devices using Bluetooth; processing data streams and transmitting data packets. The advantage is that such functionality is accessible in phones from most suppliers. Additionally, depending on the device, a mobile phone can give access

to internal resources that could be utilised as a sensor input for monitoring activity (e.g. built in GPS or tilt-sensing accelerometer). The mobile phone used for Personalised Ambient Monitoring is equipped with an application operating in the background which performs communication with other wearable devices and if needed can perform basic processing on incoming data prior to storage. Additionally it performs scans for other Bluetooth-enabled devices in range (especially other mobiles) which can correlate with the current social environment [3]. In order to maximise compatibility the application was developed using universal the Java interface which should work on all Java-enabled phones, regardless of brand.

Using the phone as a processing and storage node resulted in utilising Bluetooth as a main wireless connectivity standard for the other wearable devices used in the design. These are: an off-the-shelf GPS unit (which is an option for phones without built-in GPS module) and a custom made belt-worn device that incorporates a microphone acquiring basic features of ambient sound (e.g. zero crossing rate) that it is possible to process to infer the profile of surrounding environment [4]. Another sensor included is a light detector able to determine the ambient light level. What is more, the sensor is able to determine whether the light source is artificial by extracting the 50 Hz component corresponding to the frequency of the mains supply. The device also incorporates an accelerometer for monitoring users' activity [5]. The applied three axis accelerometer acquires data with sampling frequency of 20 Hz at 8bit resolution.

Environmental Sensors

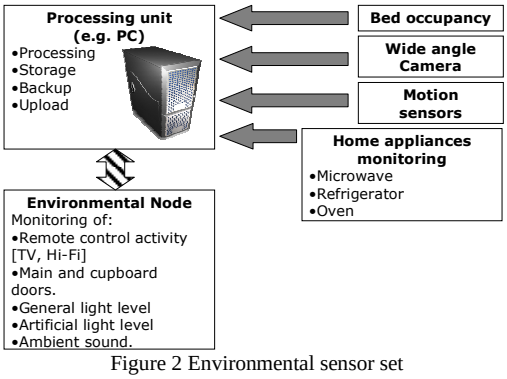

Figure 2 Environmental sensor set

The second group of sensors selected for the technical trial consists of mostly off-the-shelf devices for indoor monitoring. The list includes: Passive Infra-Red motion detectors, wall-mounted camera, bed occupancy mat, and a custom made set top device with sensors for monitoring light levels, ambient sound (as in the wearable unit) and remote control activity. Most of the devices are wireless and communicate using either Bluetooth or a 433 MHz radio frequency link

III. INITIAL EXPERIMENT

In the preliminary tests a willing participant with no history of bipolar disorder was carrying some or all components of the wearable set during the day with sensor data recorded on the phone. Also a subset of the environmental sensors was incorporated into a household. The aim was to prevalidate the technology before conducting more thorough tests on the system as a whole.

Results rendered all sensors operating correctly and ready for experimenting with persistent ambient monitoring.

IV. DISCUSSION

The next step for the project is to validate the system as a whole and assess its capability for continuous monitoring. The technical trial focusing on reliability and acceptability is due to start in the near future. The success of the project may result in a completely novel approach in managing bipolar disorder effecting lives of thousands patients diagnosed with the condition

ACKNOWLEDGEMENTS

The authors would like to thank the EPSRC, UK for their funding of the PAM project (Grant: EP/F003714/1), our fellow team members on the PAM project from the University of Stirling and the University of Southampton and colleagues from the Applied Optics Group at the University of Nottingham.

REFERENCES

[1] C.J. James et al., "Personalised Ambient Monitoring (PAM) for the mentally ill", 4th European Congress for Medical and Biomedical Engineering, November 2008

[2] S. N. Ghaemi, "Mood Disorders : A Practical Guide", Blackwell, 2008, pp.29-58

[3] J Perki et al., "Utilizing Rich Bluetooth Environments for Identity Prediction and Exploring Social Networks as Techniques for Ubiquitous Computing", International Conference on Web Intelligence, 2006

[4] E. Alexandre, L. Cuadra, M. Rosa and F. López-Ferreras "Feature Selection for Sound Classification in Hearing Aids" IEEE Trans. on Audio, Speech, and Language Processing, Vol. 15, 2007, pp.2249-2256

[5] J.D. Amor and C.J. James. "Personalised Ambient Monitoring: Accelerometry for Activity Level Classification", 4th European Congress for Medical and Biomedical Engineering, November 2008

SMART IMPLANTS USING TELEMETRY

J. L. Nemchand[1], A.W.Anson[1], B.J.Jones[1], D.Wilson[2]
[1]Experimental Techniques Centre, Brunel University, Uxbridge, UB8 3PH UK
Smith and Nephew Research Centre, York, YO10 5DF
Jaya.Nemchand2@brunel.ac.uk,

Abstract - The object of this study is to determine strain distribution in an intramedullary nail instrumented with strain gauges, positioned in three physiologically relevant sites. Loads carried by the nail during simulated fracture healing were monitored *in-vitro*, using custom designed jigs, integrated in a biomechanical test frame. Strain measurement was higher on the medial side of each of the fractures in various positions. Simulated bone composite material was applied to the fracture incrementally, to approximate fracture healing. Strain was measured after each step of bone callus bridging and a gradual decrease in strain was observed.

I. INTRODUCTION

Intramedullary (IM) nailing is a method of internally stabilizing, diaphyseal long-bone fractures to facilitate healing. Typically, the nail is secured by lateral screw fixation and its structural properties such as stiffness are expressed according to load directions, bending or torsional stiffness.

Continuous monitoring of changes of the *in-situ* load distribution between the implant and the surrounding bone is typically carried out using conventional X-Rays, MRI and micro CT imaging. During fracture healing, load sharing between the implant and the bone changes; measurements of the loads occurring during fracture healing can be performed using the telemetry system with strain transducers.

Telemetry has previously been used experimentally to investigate the performance of implants. Telemetry used in measurements with strain gauges and methods for a safe design has been developed and demonstrated by Bergmann *et al.*, for the measurement of hip prostheses loading [2]. A later study by Schneider *et al.* [1] concluded that "an implant equipped with a multi channel telemetry system is a powerful tool for investigating loading *in-vivo*, the influence of posture and physiotherapy, load changes due to fracture consolidation and skeletal loading in general can be realised." However, there has been no published study to measure the load supported by a cannulated intramedullary nail during the healing process [1].

II. METHODS

A commercial tibial nail (1.3cm x 32cm) was instrumented with 12 strain gauges which were wired to an external data logger. The gauges were mounted onto machined flats at three strategic positions, four proximally, four at the mid-shaft section and four distally. The four gauges at each level were placed on the anterior, posterior, medial and lateral sides of the nail and oriented with respect to the vertical axis of the nail.

The instrumented tibial nail was implanted in an anatomically correct bone mimic. A polymer interface was attached at the top and the bottom of the construct to interface with a calibrated test machine as shown in Figure 1. Three segmental transverse fracture patterns were investigated in the proximal, midshaft and distal third of each sawbone. A "T"-pin loading mechanism was used to accommodate bending and angular or offset loads applied to the construct. The custom-made loading fixtures were used to facilitate a combined loading of torque and axial compression while applying different offsets, proximal, 23mm, and distal, 9mm, from the axis of the tibia. The proximal and distal offsets were based on a study by Hutson [3].

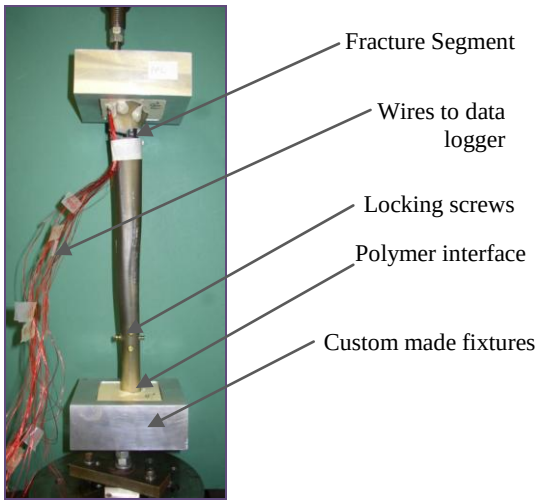

FIGURE 1: PROXIMALLY FRACTURED ANATOMICALLY CORRECT BONE MIMIC CONSTRUCT ATTACHED TO THE INTERFACE OF A COMPRESSION MACHINE

The fixtures and loading pins were tailored to fit an Instron Mechanical Test Machine (8501). Strain gauge output was directed to a Solartron Data Logger, controlled by a Scorpio data acquisition system. The mechanical test rig was capable of applying a mixed bending/compression load. The nail construct was loaded axially with the load beginning at 0 N to 500 N at 50 N increments. At each load increment, the nail-sawbone strain was measured. Axial unloading was also measured.

III. RESULTS & DISCUSSION

It was observed that for each construct, the medially positioned gauge at the site of fracture measured the highest strain value. The lowest value was generally found on the posterior side. The highest strain measurement observed ranged from 400 με to 550 με at a peak load of 500 N. Both the loading and unloading strain was measured and the hysteresis was indicative of elastic deformation under the test load conditions. The strain measured showed consistency in the results. However, by performing bending and torque, the result will be reinforced.

The hypothesis proposed is that forces measured from an intramedullary nail, normalised by the ground reaction force, will progressively decrease in a sigmoidal manner as a midshaft fracture heals. A reduction in nail load will depend on the fracture mechanics and the patient status. Schneider *et al.* reported a 50% drop in the load transmitted in the nail for a midshaft comminuted fracture [1]. To investigate this hypothesis, fracture healing simulation was introduced in the study.

In order to achieve a composite with similar mechanical properties to bone callus material, an experiment was initiated to approximate callus material. The method was to mix by volume, particulate and fibrous materials of 5%, 10% and 25% with an epoxy resin. The filler materials used were from macerated Sawbone and hydroxyapatite powders. Each mixture was cast as a solid cylinder and under compression testing, stress-strain data was compared to human bone properties.

The modulus of elasticity for human bone in compression is 18.2 GPa [4]. The values of the composites designed from epoxy, sawbone and HA, range from 68 -111 MPa. At 111MPa, the composite used was 0.6% of the actual modulus of elasticity of bone, but is used as a proxy model to approximate early-stage healing.

The composite was then applied to the fracture on the proximally fractured sawbone construct. The steps followed for the callus bridging application have been described below. **Step 1:** External callus bridging-posterior plane; **Step 2:** External callus bridging-medial plane; **Step 3:** Internal cortical wall bridging-posterior plane; **Step 4:** Internal cortical wall bridging medial plane; **Step 5:** External callus bridging-lateral plane; **Step 6:** Internal cortical wall bridging-lateral plane; **Step 7:** Internal cortical wall bridging-anterior plane; **Step 8:** External callus bridging-anterior plane. The width of the external callus was set at 5 mm. Strain measurement was taken after each step, and the process took approximately 8 days, including 24hrs to ensure curing of the synthetic callus mixture. Figure 2 below shows the drop in strain on the proximally fractured sawbone, the medial gauges in steps.

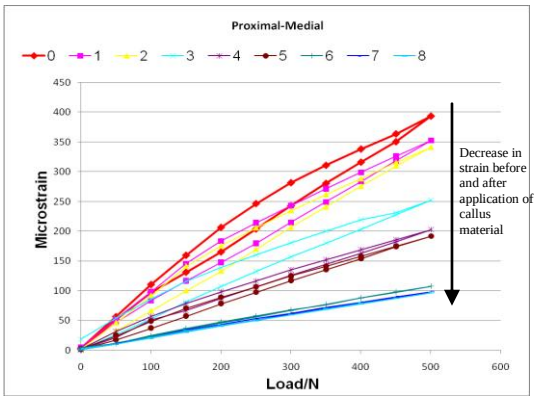

FIGURE 2:PROXIMAL FRACTURE, MEDIAL GAUGE

IV. CONCLUSION

Loading the bone during simulated fracture healing has been investigated; this indicates a decrease in strain in the IM nail as healing processes continue and identifies the site of highest strain in the medial side, independent of fracture site. The bone composite material used is 0.6% of the modulus of elasticity of bone. This shows the response of mechanical loading on the nail when initial callus bridging occurs. The decrease in strain measurement is comparable with the *in-vitro* study by Schneider *et al.* They stated that fracture healing results in a large reduction of implant loads. However, even after fracture consolidation, the loads on the nail can be significant and are expected to increase with patient activities [1]. This study simulated early fracture healing and did not take into account the influence of connective and muscular tissue activity which plays a significant role in fracture healing. However, this study confirms that bone healing processes play an important role in the loading regime of the intramedullary nails and proposes an experimental methodology to replace animal models in the development of novel implants.

ACKNOWLEDGEMENTS

We Thank Smith and Nephew Plc for supply of instrumentation and support

REFERENCES

[1]. E.Schneider, M.C. Michel, M.Genge, K. Zuber, R. Ganz and S. M. Perren; J Biomech 34 (2001) 849-857

[2]. G. Bergmann , F. Graichen , J. Siraky , H. Jendrzynski and A. Rohlmann; J Biomech, Vol.21, No. 2, pp. 169-176, 1988

[3]. Hutson, Zych, Cole, Johnson, Ostermann, Milne, Latta; Clin Orthop Relat R. 315:129-137, June 1995.

[4]. Bones Structure and Mechanics – J.D.Currey, Princeton University Press,2002

THE EFFECTS OF MECHANICAL PROPERTIES OF TRANS-TIBIAL PROSTHESES ON USE PERFORMANCE

M. J. Major, M. Twiste, L. Kenney, and D. Howard

Centre for Rehabilitation and Human Performance Research, University of Salford, Salford, UK

m.j.major@pgr.salford.ac.uk

Abstract - There currently exists a wide range of commercially available prosthetic components which prosthetists can select in order to assemble a modular trans-tibial prosthesis. Each component possesses a specific mechanical function which will affect the performance of the user. This study introduces a novel method of systematically investigating the influence of prosthetic mechanical function on user performance. This is conducted with the use of a purpose-built prosthesis that allows for independent control of the dorsiflexion and plantar flexion stiffness of the ankle joint. The prosthesis is then tested in gait experiments under various walking conditions, from which preliminary results are reported.

I. INTRODUCTION

As the design of trans-tibial prostheses has continued to advance, this has led to a wide range of alternative commercially available modular components, which when assembled comprise the trans-tibial prosthesis. Each component's mechanical function will have a direct influence on the performance of both the prosthesis and, consequently, the user. The effects of various trans-tibial components on user performance have been thoroughly investigated [1]. Studies have also been conducted which characterise the mechanical properties of prosthetic components (i.e. stiffness and damping properties) and attempt to reveal their specific mechanical behaviour during gait [2].

However, there appears to be very little quantitative evidence supporting manufacturers' claims that particular foot designs provide the user with a biomechanical or physiological advantage compared to alternative designs. The objective of this study was to design a controlled method of investigating the influence of trans-tibial prosthesis stiffness properties on the biomechanical and physiological performance of the amputee. Preliminary results of gait experimentation will also be presented.

II. METHODS

The primary objective of this study was to perform a controlled investigation of the influence of mechanical properties on user performance. In order to do so, a purpose-built prosthesis was designed with adjustable ankle-joint stiffness characteristics. This allowed for a comprehensive investigation of the effects of a wide range of prosthetic stiffness properties on gait without the use of commercial products. The mechanical model known as "roll-over shape" was adopted in order to quantify the mechanical behaviour of the prosthesis [3]. Roll-over shape is a quasi-static representation of how the prosthesis deflects during the stance phase of gait. This information on compliance during weight-bearing reflects the dorsiflexion and plantar flexion stiffness of an assembled prosthesis (i.e., foot and pylon). The roll-over shape of the prosthesis is measured independent of the amputee user by a custom-designed test-rig, utilizing a 6-component load cell (JR3, JR3 Inc., CA, USA) that is installed between the pylon and mounting surface [4].

III. RESULTS

The purpose-built prosthesis used during gait experimentation is comprised of four components, as described in Figure 1. Controlled adjustment of the mechanical properties of the prosthesis is performed through use of a custom-designed foot-ankle mechanism. The ankle stiffness, and hence roll-over shape, is determined by two linear compression springs which can be moved along a track to vary their distance from a central pivot. The ankle dorsiflexion stiffness ($K_{rot,1}$) and plantar flexion stiffness ($K_{rot,2}$) is then described by the following equation,

$$K_{rot,i} = K_{lin,i} \times r_i^2 \qquad \text{for } i = 1, 2, \qquad (1)$$

where $K_{lin,i}$ is the linear stiffness of the respective spring in dorsiflexion or plantar flexion, and r_i is the fixed distance of that spring from the pivot. An important feature of this device is that the dorsiflexion and plantar flexion stiffness can be modified independently of each other. The custom test-rig is used to quantify the mechanical properties of the assembled prosthesis (i.e., all components distal to the socket) for various arrangements of the springs.

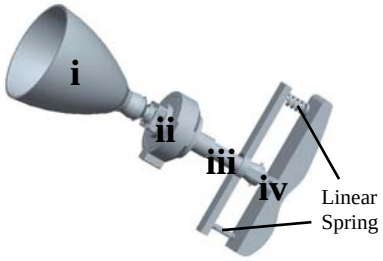

Figure 1. Components of the purpose-built prosthesis, from most proximal to most distal: i) socket, ii) load cell, iii) pylon, and iv) foot-ankle mechanism

The purpose-built prosthesis described here allows for controlled investigations of the effects of different mechanical properties on amputee gait kinematics, gait kinetics and physiological performance. For this investigation, these parameters will be observed during self-selected and fast walking (133% of self-selected speed) on a level surface, a +5% grade and a -5% grade. Motion capture equipment (10 Cameras, Vicon 612, Vicon Ltd., Oxford, UK) is used to measure the kinematics of the amputee and the purpose-built prosthesis is used to measure the roll-over shape and kinetics (i.e., force and moments distal to the socket).

During gait experimentation, the foot-ankle mechanism will be setup such that each walking condition will be tested against all combinations (four in total) of high and low dorsiflexion stiffness, and high and low plantar flexion stiffness. The levels of high and low stiffness are defined by a previous study of the mechanical properties of commercial products which reflect the prosthetic foot function of a standard, non-dynamic foot and an "energy-storage and return" foot [5]. The roll-over shapes of two of these setups as measured with the purpose-built prosthesis are presented in Figure 2. For this measurement, the purpose-built prosthesis was rolled over the floor to simulate the stance phase of gait with a constantly applied vertical force of 400 Newtons (approximately half of an average male body weight).

IV. DISCUSSION AND CONCLUSION

In summary, this paper discusses a new approach to investigating the relationship between the mechanical function of a trans-tibial prosthesis and the performance of the amputee. The novelty of this approach is that the methodology provides for a systematic exploration which is decoupled from the constraints imposed by the use of commercial products. Another novel aspect is that the purpose-built prosthesis utilises the same techniques and equipment to measure the roll-over shape in-vivo as is used in the test-rig independent of the amputee (i.e., load cell and motion capture equipment). This method allows for a seamless transition between these two measurements, thus retaining the specific foot alignment of the prosthesis as prescribed by the prosthetist.

Future work will involve investigating the effects of various roll-over shapes in order to draw correlations between mechanical characteristics of the trans-tibial prosthesis and user performance. Such information will be useful in developing an understanding of how mechanical properties should vary depending on walking condition to produce the most optimal gait. The results from this study will provide insight into appropriate prosthetic prescription of modular components and assist in establishing improved design guidelines for future prostheses.

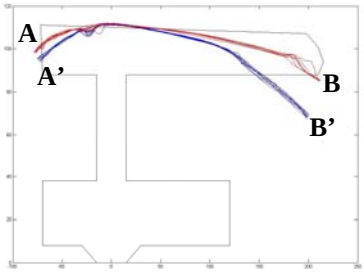

Figure 2. Roll-over shapes as measured with the purpose-built prosthesis. Ten measurements are taken of each shape and superimposed on the outline of the prosthetic foot-ankle mechanism. Shape *A-B* represents high dorsiflexion and high plantar flexion stiffness. Shape *A'-B'* represents low dorsiflexion and low plantar flexion stiffness.

REFERENCES

[1] B. J. Hafner, J. E. Sanders, J. Czerniecki, and J. Fergason, "Energy storage and return prostheses: Does patient perception correlate with biomechanical analysis?", Clinical Biomechanics, vol.17(5), 2002, pp. 325-344.

[2] H.W. van Jaarsveld, H. J. Grootenboer, J. de Vries, H. F. Koopman, "Stiffness and hysteresis properties of some prosthetic feet", Prosthetics and Orthotics International, vol.14(3), 1990, pp. 117-124.

[3] A.H. Hansen, D. S. Childress, E. H. Knox, "Prosthetic foot roll-over shapes with implications for alignment of trans-tibial prostheses", Prosthetic and Orthotics International, vol.24(3), 2000, pp. 205-215.

[4] M.J. Major, M. Twiste, L. Kenney and D. Howard, "Novel method of quantifying mechanical properties of trans-tibial prostheses", the 21st Congress of the International Society of Biomechanics, Taipei, Taiwan, July 1-5, 2007.

[5] J.F. Lehmann, R. Price, S. Boswell-Bessette, A. Dralle, K. Questad, B. J. deLatuer, "Comprehensive analysis of energy storing prosthetic feet: Flex Foot and Seattle Foot versus standard SACH Foot", Archives of Physical Medicine and Rehabilitation, vol.74(11), 1993, pp. 1225-1231.

THE SPATIO-TEMPORAL LOCALISATION OF THE CHROMOSOMAL PASSENGER COMPLEX IN DROSOPHILA

S. Li[1,2], A. Noble[1] and J. Wakefield[2]
[1]Institute for Biomedical Engineering, University of Oxford, Oxford, UK
[2]Department of Zoology, University of Oxford, Oxford, UK
simon.li@zoo.ox.ac.uk, noble@robots.ox.ac.uk, james.wakefield@zoo.ox.ac.uk

Automated techniques for screening biological images at the subcellular level are frequently used in high throughput investigations. The complementary approach of developing tools to analyse specific phenotypes allows the quantification of subtle variations. Four proteins comprising the chromosomal passenger complex have been fluorescently tagged. A combination of levelsets segmentation, feature detection and multiple particle tracking is being used to analyse time-lapse movies of their localisation. Initial results suggest the system cannot be used in a fully automated manner, but will be useful for assisted analysis of data.

I. INTRODUCTION

Automated quantitative techniques are a promising tool for the analysis of biological data at the subcellular level. Most work has so far concentrated on the statistical analysis of high-throughput data with a view to identifying potentially interesting targets, for instance by screening uncharacterised genes for behaviour suggestive of a role in cancer, or testing thousands of novel drug compounds [1].

The generality of these imaging tools limits their utility in analysing specific subcellular phenotypes, and in addition they are typically limited to *in-vitro* data. The alternative approach of developing targeted algorithms for tasks such as following chromosome movements or microtubule tracking is gaining in popularity [2], [3], and will open the way towards the analysis of *in-vivo* data, with applications ranging from low-level biological research to diagnostic analyses of tumour biopsies.

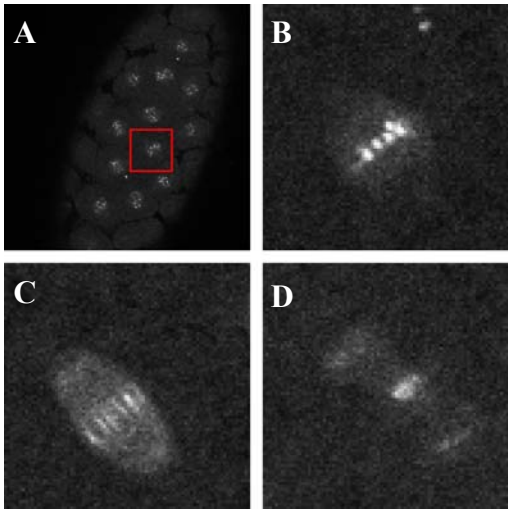

FIGURE I. BOREALIN-GFP LOCALISATION DURING MITOSIS. **A**: CONFOCAL IMAGE OF AN EMBRYO IN PROPHASE. **B**: CLOSE-UP OF ONE NUCLEUS AT METAPHASE. **C**: ANAPHASE. **D**: TELOPHASE.

The chromosomal passenger complex (CPC) is a complex of four core proteins involved in the regulation of mitosis (cell division). The CPC has a highly dynamic localisation throughout the cell cycle, but the mechanisms of complex formation and dissociation are yet to be identified, and typical methods of perturbing their function (e.g. using RNAi) lead to catastrophic phenotypes early in mitosis, precluding a detailed analysis of their behaviour [4]. The novel application of quantitative image analysis techniques to the dynamic characterisation of the protein complex will allow the quantification of subtle phenotypes in response to minor perturbations, leading to information on the functional behaviour and interactions of the CPC members.

II. METHODS

A. Image Acquisition

Drosophila melanogaster fly lines were genetically engineered to express a green fluorescent protein (GFP) attached to one of the four CPC members. Live embryos were imaged on a laser-scanning confocal microscope, and the subcellular localisation of the GFP-tagged proteins throughout the cell cycle was recorded. 512 x 512 images with pixel size 250 nm by 250 nm were recorded at 10 s intervals.

A complete mitotic division takes around eight minutes (40 frames). During the early stages of mitosis the CPC localises to the kinetochores, visible as a set of dots. In the latter stages it localises to the central spindle which has the appearance of streaks, followed by relocating to the midbody in-between the two daughter nuclei.

B. Detection and Tracking

Early embryos (0-3 h old) contain a field of synchronously dividing nuclei (Figure 1a). A frame at metaphase (Figure 1b), which is easily detectable by a user, is manually selected. An initial segmentation is obtained by using Otsu's method twice to identify the bright kinetochore dots, followed by the less intense indistinct

nuclear/spindle localisation. A fast levelsets algorithm, which uses an iterative process to evolve a contour towards any edges present in the image is used to refine the segmentation [5]. Following and preceding frames are segmented using the neighbouring frame's segmentation as an initialisation. Due to the variation in intensity over the image a cost function which is not reliant on absolute intensity values is used [6].

Particle detection is performed using a particle filter [3]. This uses a Bayesian approach to tracking, allowing prior knowledge to be incorporated, and has the ability to handle multiple hypotheses. This should allow the tracker to recover from tracking errors, whether due to noise or temporary disappearance of a particle.

From anaphase onwards the streaks associated with the central spindle are detected using a steerable filter pair designed to detect ridges [7]. Their locations and orientations are found by thresholding and averaging the filter responses.

III. RESULTS

The ability of the tracker to follow the kinetochores and subsequent central spindle localisation is highly dependent on the image quality (Figure 2). Example tracking errors (compared with manual tracking) are shown in Table 1. Visual assessment of the detected tracks suggests most of the error is due to one of the four particles apparently disappearing from view, which is a major problem for both automated and manual tracking, and this is partly reflected by the errors of the three best particles. The disappearance or variation in intensity of particles is primarily due to them moving in or out of focus.

TABLE I
EXAMPLE ROOT MEAN SQUARE TRACKING ERRORS (RMSE) FOR 2 SEQUENCES

Length of image sequence (frames)	11	15
RMSE per track per frame (px)	2.0	2.0
RMSE ignoring tracks (best 3) (px)	1.0	0.8

IV. DISCUSSION

The current tracker is not sufficiently robust to be run unsupervised, but the flexibility of the particle filter should allow further improvements to be made.

There is still the potential to use the tracker for assisted analysis of data, and at present it is being used to analyse data obtained from a fluorescence recovery after photobleaching (FRAP) experiment which involves the measurement of the intensity recovery following photobleaching of a fixed region, providing information on the molecular kinetics of a protein. The use of this software will remove the restriction to stationary objects.

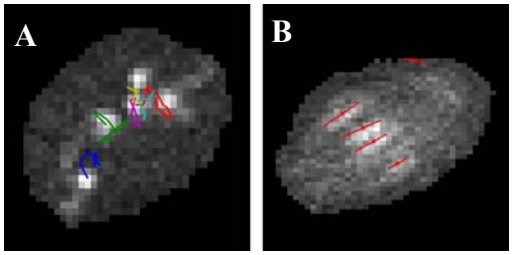

FIGURE 2. **A**: EXAMPLE KINETOCHORE TRACKS AFTER CORRECTION FOR EMBRYO MOVEMENT. **B**: EXAMPLE OF CENTRAL SPINDLE STREAK DETECTION.

Future work will involve examining the trade-off between spatio-temporal resolution of the data, photobleaching and noise, and obtaining sufficient quantities of data to find statistically valid differences.

V. CONCLUSION

The development of novel analytical software to probe the formation and function of protein complexes is heavily interdependent on the image acquisition parameters. Although a complete system has not been achieved, the existing software should be useful in a user-assisted setting, and work on improving the system continues.

REFERENCES

[1] T. Walter, M. Held, B. Neumann, J. Heriche, C Conrad, R. Pepperkok and J. Ellenberg, "A genome wide RNAI screen by time lapse microscopy in order to identify mitotic genes-computational aspects and challenges", Proc. 5th Int. Symp. Biomedical Imaging, 2008, pp. 328-331.

[2] C. Yau and J. Wakefield, "Quantitative image analysis of chromosome dynamics in early Drosophila embryos", Proc. 4th IEEE Int. Symp. Biomedical Imaging, 2007, pp. 264-267.

[3] I. Smal, K. Draegestein, N. Galjart, W. Niessen and E. Meijering, "Particle filtering for multiple object tracking in dynamic fluorescence microscopy images: Application to microtubule growth analysis", IEEE Trans. Med. Imag., vol.27(6), 2008.

[4] S. Ruchaud, M. Carmena and W. Earnshaw, "Chromosomal passengers: Conducting cell division", Nature Reviews Molecular Cell Biology, vol.8(10), 2007.

[5] Y. Shi and W. Karl, "A real-time algorithm for the approximation of level-set-based curve evolution", IEEE Trans. Image Process., vol.17(5), 2008.

[6] S. Lankton, D. Nain, A. Yezzi and A.Tannenbaum, "Hybrid geodesic region-based curve evolutions for image segmentation", Proc. SPIE Medical Imaging, vol.6510(3), 2007.

[7] M. Jacob and M. Unser, "Design of steerable filters for feature detection using canny-like criteria", IEEE Trans. Pattern Anal. Mach. Intell., vol.26(8), 2004.

PHASE RESETTING AS A MECHANISM OF ERP GENERATION; EVIDENCE FROM THE POWER SPECTRUM

I. Daly[1] & S. J. Nasuto[1] & K. Warwick[1]

[1]Cybernetics Department, University of Reading, Reading, UK

i.daly@reading.ac.uk,

Abstract – A Neural Mass model is coupled with a novel method to generate realistic Phase reset ERPs. The power spectra of these synthetic ERPs are compared with the spectra of real ERPs and synthetic ERPs generated via the Additive model. Real ERP spectra show similarities with synthetic Phase reset ERPs and synthetic Additive ERPs.

I. INTRODUCTION

A current debate in the study of Event Related Potentials (ERPs) in the Electroencephalogram (EEG) is the mechanism by which they arise. Two common mechanisms proposed to explain their origin are the Additive and Phase reset models [4].

The Additive model assumes the ERP arises from the addition of an event locked amplitude modulation in the EEG [1]. By contrast the Phase resetting model assumes ERPs arise from the combined effect of phase synchronisation of different alpha band frequency components in the EEG [1].

Traditional methods of testing the two models are to simulate how the data would look if it were generated by one model. Properties of the simulated data are then tested against real recordings of ERPs [1]. However, the simulated data used for these tests is often over simplistic and does not produce realistic EEG. Often summed sine waves are used to produce the simulated ERPs [1]. Such simple models may differ from real EEG in significant ways such as their power spectra.

Attempts have been made to generate realistic ERPs by the Additive model through the use of Neural Mass models [3]. However, no such attempts have been made with the Phase reset model.

Therefore, a method of generating ERPs from realistic artificial EEG is introduced using a Neural Mass model. These synthetic ERPs adhere to the Phase reset modelling paradigm. The power spectra of the synthetic ERPs generated by the Phase reset model is compared against those generated by a synthetic Additive model and real ERP data.

II. ERP SIMULULATION AND DATA

A Neural Mass model represents a cortical area by a population of excitatory pyramidal cells, receiving both intrinsic inhibitory and excitatory feedback from local interneurons and excitatory input from extrinsic areas. Any extrinsic input is modelled by a stochastic Gaussian process, see [2] for further details.

The Additive model uses realistic synthetic EEG from the Neural Mass model. To this we add a sine wave of frequency 11.5Hz ranged from 0.28s to 0.40s and multiplied by a gain of 10. This is consistent with the Additive model for realistic synthetic ERP generation in [3].

The Phase reset ERPs are generated via the following steps.

i. Clean EEG is band-pass filtered into alpha (8 – 14Hz) and non-alpha frequency bands.
ii. Alpha band EEG is further band-pass filtered into 12 sub-alpha bands of width 0.5Hz.
iii. The Hilbert transform is applied to calculate the instantaneous amplitude and phase of each sub-alpha band signal.
iv. Each sub-alpha band is reset to a common phase ± the jitter with distribution $N(0,10)$.
v. All the sub-alpha bands and non-alpha bands are summed to produce the final trial containing a Phase reset ERP.

To asses the effects of the band pass filter step in this process both ERPs generated via the Additive mechanism and the real ERP data are band pass filtered in an identical manner to the Phase reset ERPs.

III. METHODS

It has been proposed that if the ERP shows greater power in particular frequencies then would be expected by chance it can be inferred that aspects of the EEG show event related phase synchronisation [3]. Thus, the power spectra could provide an insight into the mechanism of ERP generation.

The power spectra are found across 200 trials for the synthetic Phase reset and synthetic Additive ERPs. Thus, a distribution of expected powers across the alpha band is produced.

This process is repeated across the 48 trials of real ERP data. 48 trials of P300 ERPs are recorded at 500Hz. For further details of how this data is generated see [5].

Thus, three distributions, for Additive model, Phase reset model and real ERP data, of expected power could be formed at each frequency band. The distributions of the obtained power spectra are compared at different frequencies. A greater correlation of expected power between the real ERPs and the synthetic ERPs generated by one of the two models would indicate that the real ERP data is more likely to have been generated via that model.

IV. RESULTS

The mean power spectra for synthetic ERPs generated via Phase resetting and Additive models are compared to the mean power spectrum of the real ERP data in Figure I.

Figure I
Power spectra generated by synthetic Phase resetting and Additive models compared to real ERP data.

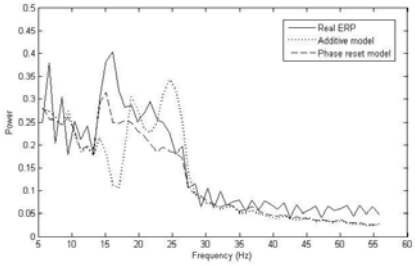

Visual inspection of the mean power spectra reveals an apparent correlation between the synthetic ERPs generated by the Phase reset model and the real ERPs in the Beta band (12 – 30Hz).

However T-tests of the difference in distributions of the expected power spectra for the three datasets highlight both some statistically significant differences ($P < 0.05$) and insignificant differences ($P > 0.05$) in the expected power between both the Additive and the Phase reset models when compared to the real ERPs. No significant differences in the power spectra are therefore conclusively indicative of either Phase resetting or the Additive model been the true mechanism of ERP generation.

V. DISSCUSSION

Traditional methods of investigating the mechanisms of ERP generation rely on over simplistic and unrealistic models of the ERP. A new method, coupled with a Neural Mass model has been introduced to simulate realistic ERPs using the Phase reset model.

The spectral power distributions of realistic ERPs simulated with the Phase reset and the Additive models have been compared to those of real ERP data. There are some differences within the Beta bands between each of the ERP generation mechanisms and real ERPs. There are also some significant similarities.

Visual inspection of the mean expected power of synthetic ERPs generated by both methods reveal an apparent stronger correlation between the mean of the Phase reset generated ERPs and the real ERPs then between the mean of the Additive ERPs and the real ERPs. However there are no significant differences between the power spectra distributions of the real ERPs and either of the synthetic ERPs that provide proof of causation of the ERP by one mechanism or the other. This adds weight to the arguments put forward in [3] that the power spectrum is not a definitive indicator of the ERP generation mechanism.

Future expansions to this work will include expanding the Neural Mass model to produce multi-channel data. This will allow additional predictions about Additive / Phase reset differences to be assessed.

VI. CONCLUSION

A method for realistic ERP generation via the Phase reset model has been introduced. ERPs generated with this method have been shown to have a power spectrum with some similarities to that of real ERPs. However consistent with the results in [3] this does not conclusively indicate causation of ERPs via Phase resetting.

This method forms a first step in more realistic modelling of phase resetting as a mechanism for ERP generation. This work demonstrates a new approach to the ongoing investigation of ERP generation.

REFERENCES

[1] Yeung N., et. al. “Detection of synchronized oscillations in the electroencephalogram: An evaluation of methods”, Psychophysiology, 41, 822-832, 2004
[2] David, O., Friston, K. J., “A Neural Mass model for MEG/EEG: coupling and neuronal dynamics”, NeuroImage, V20, 1743-1755, 2003
[3] David O. et. al. “Modelling event-related responses in the brain”, NeuroImage, 25, 756-770, 2005
[4] Ankoor S. Shah et. al. “Neural dynamics and the fundamental mechanisms of event-related brain potentials”, Cerebral Cortex, V14, 5, 476-483, 2004
[5] Data contributed by Dr. V. Calhoun. Available online http://mlsp2005.conwiz.dk/index.php”id=30.html

INFORMING PATIENT, CARER AND PROFESSIONAL IN IMPROVED STROKE REHABILITATION: FEEDBACK IN THE EXERCISE REHABILITATION REGIME

N. Shublaq[1], P. Probert Smith[1], J. Stebbins[2]

[1]Institute of Biomedical Engineering, Department of Engineering Science, University of Oxford, UK
[2]Oxford Gait Laboratory, Nuffield Orthopaedic Centre NHS Trust, Oxford, UK

nour.shublaq@eng.ox.ac.uk,

Abstract – Especially with early discharge from hospital, the progress and success in stroke rehabilitation depend crucially on maintaining and encouraging the patient's and carer's motivation for the prescribed exercise regime. The work described here develops robust algorithms to improve the application of inertial sensing technologies to provide timely and suitable feedback. It proposes a framework for a novel signal processing method which improves the reliability of measurements through incorporating anatomical constraints on a set of elementary movements integrated in typical upper arm rehabilitation, after comparing these with the 'gold standard' of a Vicon motion system.

Index terms – Rehabilitation; Telemedicine; Upper limb kinematics; Biomedical signal processing; Wearable technologies.

I. INTRODUCTION

Over two-thirds of stroke patients are impaired in activities of daily living (ADL) due to partial paralysis of the more affected upper limb [1]. The effectiveness of stroke therapy has been shown to depend on the intensity and frequency of treatment, especially in the months immediately following the stroke. While appropriate available treatments can help improve or regain function, standard treatment planning remains empirical, and the assessment of the patient's progress may vary between assessors [2]; in addition, especially with early discharge from hospital, the patient is likely to be given skilled feedback and encouragement only occasionally.

Studies [3, 4] and informal feedback from patients, carers and physiotherapists suggest that the provision of metrics which provide information on the quality of the exercises performed (e.g. the timing sequence of muscle groups, the trajectory of joints compared with the 'norm') would be beneficial in encouraging patients to take charge of their own rehabilitation regime, and perform their exercises accurately and frequently. For this to be monitored, a reliable, low cost method of measurement is needed. The goal of the work described here is to validate a simple measurement technique based on wearable sensors to monitor the arm kinematics and obtain detailed analysis of upper limb joint motion during exercises used in rehabilitation. The system would objectively inform patients and physiotherapists about progress. In the wider framework of the project, this is part of the Motivating Mobility Consortium[1].

In this paper we assess the application of this technology through comparing measurements from a state-of-the-art low cost motion sensor, Xsens™ (Motion Technologies, Netherlands), with a multi-camera Vicon™ (Oxford Metrics, U.K.) motion capture system, which acts as a 'gold standard' in a set of functional exercises which are typical in rehabilitation. We then describe and test (via simulation) a framework to improve the reliability of measurements by imposing simple anatomical constraints.

II. TECHNICAL INFORMATION

A. Methods

A trial was carried out to track and measure upper limb movements in three dimensions. The trial comprised six typical movement patterns [5], each repeated three times. A 12-camera Vicon (MX F40) system was used to capture the movements, with 39 (9 mm) passive reflective markers placed on the right / left upper limbs, the trunk, and pelvis (FIG. 1).

FIG. 1 MARKER/SENSOR PLACEMENT

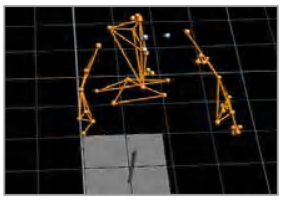

FIG. 2 UPPER LIMB MODEL (IN VICON)

A geometric model (FIG. 2) was developed based on the International Society of Biomechanics recommendations [6]. Joint angles were defined using Euler angles. Vicon compatible software (Nexus 1.2.103 and BodyBuilder 3.5.141) was used to reconstruct then label each marker and compute the spatial position and orientation of segments according to the model developed. In addition, 5 inertial Xsens MTx sensors (3-D accelerometers, gyroscopes, magnetometers; 3 shown in FIG. 1) were placed on the same segments; and

[1] funded by EPSRC (grant EP/F00382X/1)

tracked by Vicon at the same time. The two sets of measurements (Vicon, Xsens) were related to a common co-ordinate system.

B. Results

Results for forearm pronation/supination, as in FIG. 3A-3B, suggest an initial correlation (r = 0.87) between the pronation/supination angles measured by the Xsens system on the forearm segment and the angles generated by the upper limb model developed in Vicon (FIG. 3A) (rmse = 2.521). There are significant errors when the angle is small, as shown in FIG. 3B, probably caused by lack of resolution in the sensor or a sensor drift. The sensor has errors to simulate skin movement and slippage in mounting; these are superimposed on sensor measurements of the motion of skeletal structures where actual movement occurs.

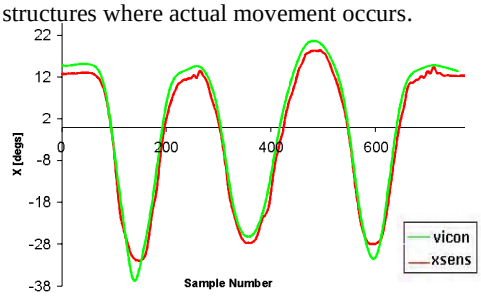

FIG. 3A: FOREARM PRONATION/SUPINATION (X)

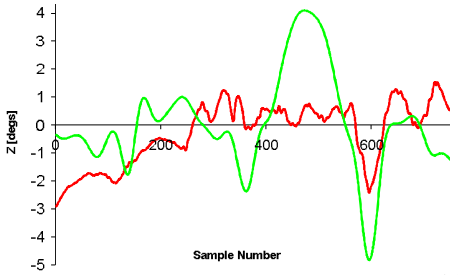

FIG. 3B: FOREARM PRONATION/SUPINATION (Z)

Sensor measurement errors may be reduced by imposing simple anatomical constraints for a given movement; e.g. forearm pronation/ supination takes place mainly about the longitudinal axis of the forearm and is minimal about the lateral axis. To test this framework formulation, we simulated a range/bearing sensor on the body watching movement of a target on the wrist in one dimension (such as a reach and grasp movement) predicting both its position in 2D and velocity. The range sensor has errors to simulate skin movement and slippage in mounting. The true vs. estimated plots of range and bearing are given in FIG. 4 (top, bottom) respectively. As can be seen, the estimated values of the wrist position converge to their corresponding true values inspite of the sensor errors. The results illustrate too the difficulties associated with Cartesian/polar transformations which can give 2π ambiguity non-linearity (in this case tangent) in the (see midway of simulation of FIG. 4 bottom). This might imply using a quaternion axis system.

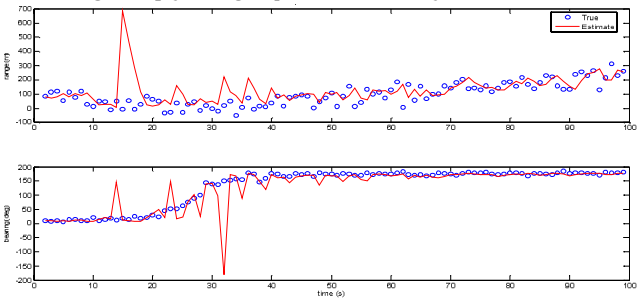

FIG. 4: SENSOR RANGE (m)/BEARING (deg): TRUE VS. ESTIMATE

C. Discussion

Early results have shown good agreement between inertial sensors and the Vicon multi-camera system. However there are difficulties when the angular velocity is low (the results are within 5° which is clinically seen as acceptable) [7]; optimisation algorithms to model joint and sensor readings together should extend the useful range [8]. The use of cyclic movement in exercise reduces the problem of drift in inertial sensors. Errors in sensor/marker placement and calibration also lead to errors, and a systematic mounting protocol is being developed. In addition, prediction algorithms with anatomical constraints have shown promise to improve sensor measurements. Further tests are requested on repeatability/clinical relevance.

III. CONCLUSION

A 3D biomechanical model was developed to measure upper limb motion using both Xsens and Vicon systems. Data from a small set of movements, including pronation/ supination of the forearm, were collected. Correlation (r = 0.87) was found in the angular graphs between the systems. A novel method to improve sensor measurement reliability by incorporating anatomical constraints was found promising.

REFERENCES

[1] M. Caimmi, S. Carda, C. Giovanzana et al., "Using kinematic analysis to evaluate constraint-induced movement therapy in chronic stroke patients," *Neurorehabil. Neural Repair*, vol. 22, pp. 31-39, 2008.

[2] E. Blair and F. Stanley, "Interobserver agreement in the classification of cerebral palsy," *Dev Med Child Neurol*, vol. 27, pp. 615-622, 1985.

[3] J. M. Winters, "TeleRehabilitation research: emerging technologies," vol. 4, A. R. o. B.., 2002, pp. 287-320.

[4] B. Rohrer, S. Fasoli, H. I. Krebs, R. Hughes et al., "Movement smoothness changes during stroke recovery," *J. Neurosci.*, vol. 22, pp. 8297-8304, 2002.

[5] C. Anglin and U. P. Wyss, "Review of arm motion analyses," *IMechE*, pp. 541-555, 2000.

[6] G. Wu, F. Van der Helm et al., "ISB recommendations on definitions of joint coordinate systems of various joints for the reporting of human joint motion Part II," *Journal of Biomechanics*, vol. 38, pp. 981-992, 2005.

[7] V. M. Zatsiorsky, *Kinematics of Human Motion*, 1998.

[8] H. Zhou et al.,"Use of multiple wearable inertial sensors in upper limb motion tracking," *Medical Engineering & Physics*, vol. 30, pp. 123-133, 2008.

RELIABILITIY OF MEASUREMENTS OF ABDOMINAL MUSCLE THICKNESS DURING ACTIVE STRAIGHT LEG RAISE (ASLR) TEST

S.P. Chen[1], M. Stokes[1], P.H. Chappell[2], R. Allen[3]
[1]School of Health Sciences, [2]School of Electronics & Computer Sciences, [3]Institue of Sound & Vibration Research, University of Southampton, Southampton, UK

sc3w07@soton.ac.uk

This pilot study on healthy Taiwanese women examined the reliability of measuring thickness of the transversus abdominis (TrA) muscle at rest and during a functional task of active straight leg raising (ASLR), using real-time ultrasound imaging. The reliability of repeated measurements was assessed between-scans and between-days in 16 subjects using intra-class correlation coefficients (ICCs) and Bland-Altman analysis. High ICCs indicated good reliability of all measurements (ICC > 0.73), particularly at rest (ICC > 0.8) and good agreement was displayed by Bland-Altman results. The findings demonstrate that ultrasound imaging has sufficient reproducibility for examining the TrA muscles during the ASLR test.

I. INTRODUCTION

The abdominal muscles are considered to be stabilizers in the lumbo-pelvic region, so assessment of these muscles is recognized as being important. The transversus abdominis (TrA) muscle is thought to play a particularly important role as a stabilizer to protect the lumbar spine [1]. The abdominal muscles can become wasted and weak in people with low back pain. A type of back pain can arise from the tail bone (coccyx), which is termed coccydynia [2]. This is a particular problem in Taiwan, more so than in western countries, possibly due to lifestyle differences, although evidence to support this is only anecdotal. The incidence of coccydynia is five times greater in women than men [2]. Rehabilitative Ultrasound Imaging (RUSI) offers a direct way to visualize and measure the abdominal muscles at rest and during functional tasks [3]. The active straight leg raise (ASLR) is a test used to examine the function of the lumbo-pelvic region. However, the reliability of repeated measurement of abdominal muscles during the ASLR task has not yet been established.

II. METHODS

A pilot study was carried out on 16 young Taiwanese women to establish the reliability of ultrasound measurements of TrA muscle thickness. Subjects aged 20 to 35 years-old were recruited from the Taiwanese students' society of the University of Southampton. They attended sessions for testing on two different days.

A real-time ultrasound scanner (Aquila, Pie Data) was used to obtain images of the muscles, using a 6MHz linear transducer (see Figure 1). The lateral abdominal wall was scanned bilaterally, twice at rest and twice during unilateral ASLR in each session. Alignment of the transducer was maintained as consistently as possible during the contraction, but some relative motion was unavoidable. Images were stored and muscle thickness was measured manually off-line using Image J software (http://rsb.info.nih.gov/ij/). The cursor was placed on the inside edge of superior and inferior muscle boarders in the middle region of the image where they are parallel horizontal.

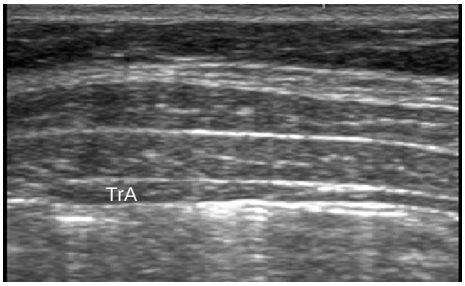

Figure 1: Ultrasound scan of the lateral abdominal muscles, indicating transversus abdominis (TrA), which is the deepest muscle.

Statistical analyses used to assess the between-scans and between-days reliability of the measurements of muscle thickness were intra-class correlation coefficients (ICCs) and Bland-Altman plots. The smallest detectable change (SDC) reflects the smallest within-groups changes in scores [5]. The standard error of measurement (SEM) and SDC were calculated to provide an indication of clinically meaningful variations in measurements. A two-way analysis of variance (ANOVA) was used to compare the differences between sides and between different states (i.e. rest and contraction) to calculate ICCs.

II. RESULTS

The thickness of the TrA muscle under the different conditions is shown in Table 1.

Table 1. Descriptive findings of transversus abdominis (TrA) muscle thickness (mm) obtained from the right (Rt) and left (Lt) sides of the abdomen, in states of rest and contraction during an active straight leg raise (ASLR)

Side/States	Mean (mm)	*SD (mm)*
Rt/Rest	2.1	*0.7*
Rt/ASLR	2.09	*0.65*
Lt/Rest	2.1 3	*0.63*
Lt/ASLR	*2.2 2*	*0.56*

High ICCs (ranges 0.75-0.99) were found between-scans and between-days, both at rest and during contractions (see Table 2).The SEM values were vey small ranging from 0.06-0.33 mm. The SDC values were also small, ranging from 0.04-0.22 mm.

Table 2. Results for intraclass correlations (ICCs), standard error measurement (SEM) and smallest detectable changes (SDC).

Between-scans measurement			
Side/States/ Day	ICCs	SEM (mm)	SDC (mm)
Rt/Rest/1st	0.85	0.26	0.18
Rt/Rest/2nd	0.87	0.28	0.19
Rt/ASLR/1st	0.96	0.18	0.12
Rt/ASLR/2nd	0.94	0.19	0.13
Lt/Rest/1st	0.8	0.3	0.21
Lt/Rest/2nd	0.88	0.23	0.16
Lt/ASLR/1st	0.99	0.06	0.04
Lt/ASLR/2nd	0.99	0.07	0.05
Between-days measurement			
Side/States	ICCs	SEM (mm)	SDC (mm)
Rt/Rest	0.9	0.22	0.15
Rt/ASLR	0.75	0.33	0.22
Lt/Rest	0.87	0.23	0.15
Lt/ASLR	0.89	0.19	0.13

1st and 2nd = mean of scans on the first and second days respectively; Rt and Lt = mean values for the right and left sides.

The Bland-Altman analyses for between-scans and between-days reliability showed good agreement, with the mean differences being close to zero (see Table 3).

Table 3. Results of the Bland and Altman analyses: mean difference ($\bar{d}$) and the 95% limits of agreement

	Bland and Altman	
	$\bar{d}$	95% CI for $\bar{d}$
Between-scans measurement		
1st /Rt /Rest	0	0.11 → -0.1
1st /Rt/ ASLR	0	0.11 → -0.13
1st/Lt/Rest	0.03	0.15 → -0.09
1st/Lt/ASLR	0	-0.1→0.1
2nd /Rt /Rest	0.01	0.08 → -0.07
2nd /Rt/ ASLR	-0.01	0.07 → -0.08
2nd /Lt/Rest	0.01	0.08 → -0.06
2nd /Lt/ASLR	-0.01	0.07 → -0.1
Between-days measurement		
Rt/ Rest	0	0.09 → -0.09
Rt/ASLR	0	0.1 → -0.1
Lt/Rest	-0.02	0.1 → -0.14
Lt/ASLR	-0.01	0.15 → -0.17

$\bar{d}$ is the mean difference between measurements of muscle thickness; 95% CI is the confidence intervals for the mean difference; 1st and 2nd = mean of scans on the first and second days respectively; Rt and Lt = mean values for the right and left sides.

IV. DISCUSSION

This is the first study to use real-time ultrasound imaging to measure the thickness of TrA muscles during the ASLR functional task. Similar muscle thicknesses of TrA at rest were found on both sides (Table 1) which is consistent with the literature [4].

All ICC values were high (>0.75), indicating that the technique has good reliability. The greater ICC values for the measurements made at rest than during contraction were consistent with existing published work for voluntary contractions of the TrA muscle [3]. The greater measurement errors during contractions may be caused by movement of the transducer over the skin surface or movement of the muscles beneath the skin relative to the transducer. Another explanation might be that the degree of contraction may not be identical between efforts, as this is difficult to standardise for the abdominal muscles.

The SEM and SDC values were very small and again tended to be greater for measurements made during contraction than at rest. The SDC is interpreted as a "real" change [5], so the small values found in our results can be interpreted as small measurement errors.

The limitation of the holding the transducer manually would have potentially involved changes in its angle relative to the muscle, but obviously not sufficiently enough to produce poor reliability on repeated testing. Despite the greater degree of error in measuring scans obtained during the ASLR task than at rest, all measurements were sufficiently reliable for the ultrasound technique to be used in further study of young Taiwanese women with coccydynia.

V. CONCLUSION

The application of ultrasound imaging for measuring TrA muscle thickness showed good reliability, whether performed at rest or during a functional movement using the ASLR tests.

REFERENCES

[1] P.W. Hodges, C.A. Richardson. "Transversus abdominis and the superficial abdominal muscles are controlled independently in a postural task". *Journal of Neuroscince Letters.* 1999, 265, 91-94

[2] G. Fogel, P. Cunningham, S. Esses, "Coccydynia: evaluation and management". *Journal of American Academy of Orthopedic Surgeons*, 2004, 1, 49-54.

[3] D.S. Teyhen, N.W. Gill, J.L. Whittaker, S.M. Henry, J.A. Hides, Hodges PW. "Rehabilitative Ultrasound Imaging of the Abdominal Muscles". *Journal of Orthopaedic & Sports Physical Therapy.* , 2007, 37 (8), 450-466.

[4] G. Rankin, M. Stokes, D.J. Newham. "Abdominal muscle size and symmetry in normal subjects." *Muscle & Nerve.* 2006, 34, 320-326

[5] C.B.Terwee,, S.D.M Bot, M.R. de Boer, D.A.W van der Windt, D.L. Knol, J.Dekker, L.M. Bouter, H.C.W de Vet. "Quality criteria were proposed for measurement properties of health status questionnaires". *Journal of Clinical Epidemiology*, 60, 2007, 60, 34-42.

Manufacturing of cuff electrodes and stimulation and recording of action potentials on frog sciatic nerves using self-spiralling cuff electrodes.

C.S. Stafford, Marcella Burke, Ken Rodgers, Niall MacCarthy and John Alderman
Tyndall National Institute, UCC, Cork, Ireland
ciara.stafford@tyndall.ie

Abstract – Nerve cuff electrodes are being developed to apply to peripheral trunk nerves for recording and stimulating. Split electrodes have been made with the idea of allowing specific fascicles within the cuffed nerve to be independently activated [1]. Here we describe the manufacturing of self-spiralling cuff electrodes and pilot animal studies carried out on cuff electrodes.

I. INTRODUCTION

Spiral nerve cuff electrodes consist of electrodes embedded within a self-curling sheath of biocompatible insulation which exhibits a spiral transverse cross section [2]. The spiral nerve cuff electrode is designed to be expandable so that it could be sized to fit snugly around a nerve and/or accommodate neural swelling [2]. This could be for use in peripheral nerve recording and stimulation in for example implanted FES applications such as a hand prosthesis. In this study cuff electrodes were wrapped around the sciatic nerve of a frog to generate a muscle twitch and record action potentials.

II. METHODS

a) Fabrication of self-spiralling cuff electrodes

This was done in a similar method to that outlined in ref. 3. Cuff electrodes are manufactured by gluing (silicone adhesive MED-2000) one silicone rubber sheet (thickness 0.005") to another which is stretched to a defined extent. The electrodes are fabricated on polyamide and are glued to the inside of the silicone sheets. It is the differential stretch between the silicone sheets that causes the silicone cuffs to self-roll. The electrodes are stuck down using a silicone primer (SP-120) followed by the silicone adhesive.

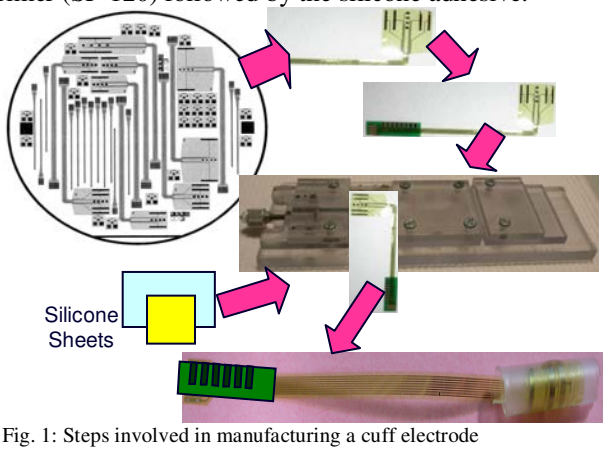

Fig. 1: Steps involved in manufacturing a cuff electrode

A PCB is attached to electrode to allow connecting to a recording and stimulating apparatus. Attach PCB to electrode before curling the silicone. Biocompatible stainless wire is soldered to the PCB. The connection of the wires to PCB is encapsulated with silicone. The encapsulation is for protection from the biological environment.

Fig. 2: Interconnections to cuff electrode

b) Animal Studies

The aim of the animal studies was to demonstrate that cuff electrodes can actually be used for electrical stimulation of neural tissue and recording of action potentials. The animal model chosen was the *Xenopus Laevis* Frog.

(i) Stimulate muscle contraction using cuff electrode

The Mac lab recording device is a computer program that simulates an oscilloscope recording device and incorporates a biological stimulator

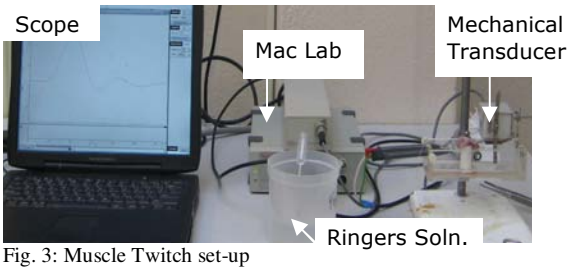

Fig. 3: Muscle Twitch set-up

Recording of muscle contractions requires the use of a transducer which converts shortening of the muscle into a voltage signal which is then fed into the Mac Lab amplifier.

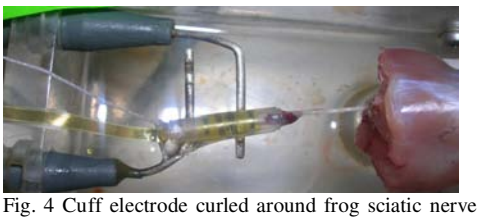

Fig. 4 Cuff electrode curled around frog sciatic nerve to stimulate and create muscle twitch.

(ii) Record Action Potential Using Cuff Electrode

Stimulated the nerve using electrodes and recorded the action potential in the nerve using a cuff electrode and the information was fed back into the Mac Lab. To prove action potentials recorded were not artefact a urethane experiment was carried out. Urethane is an anaesthetic used in animal studies. The urethane stops action potentials travelling down the nerve when applied.

III. RESULTS

a) Fabrication of self-spiralling cuff electrodes

The cuff electrodes diameter varied depending on the stretch of the silicone sheeting and the size of the device used. The cuff electrodes self-curled better when cured in a curled position.

b) Animal Studies

Gold and platinum devices were used for experiments. Delaminating was more evident on the platinum devices than the gold.

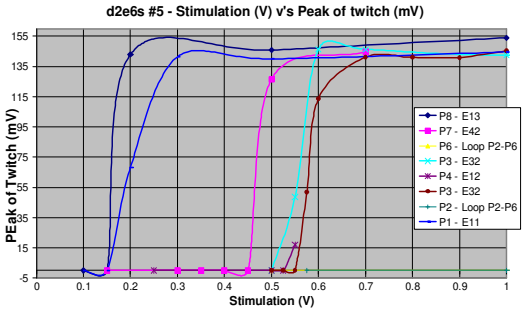

Fig. 5: Muscle Twitches – Peak of twitch vs. Stimulation (V)

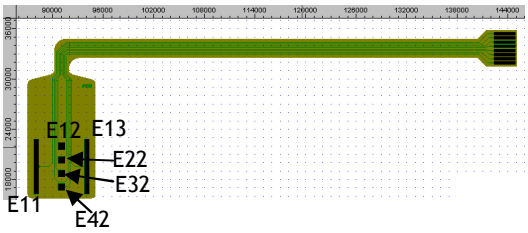

Fig. 6: Tyndall device d2e6s5 - labelling of electrodes

Muscle twitch was stimulated using cuff electrode and recorded the twitch created when stimulating using different electrodes on the device. This tells us if there is selectivity.

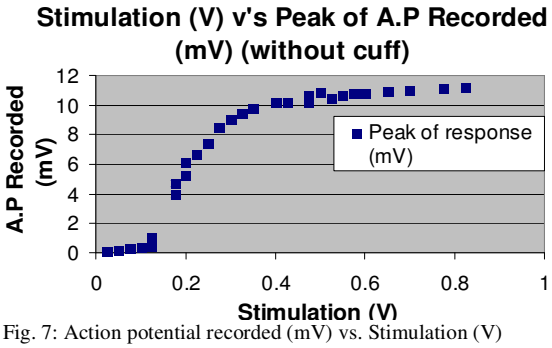

Fig. 7: Action potential recorded (mV) vs. Stimulation (V)

Recorded an action potential from a nerve using the cuff electrode and stimulated at different voltages to find out the threshold.

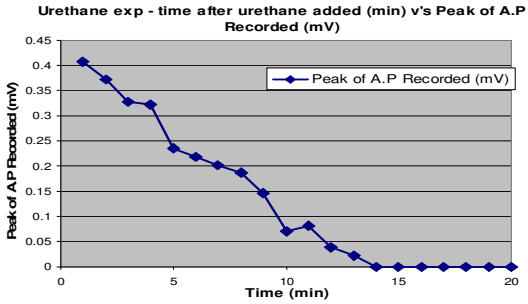

Fig. 8: Urethane Experiment – A.P recorded vs. Time (min)

To show selectivity recorded using different electrodes on the devices. The urethane experiment proved the action potentials been recorded were not artefacts.10 minutes after the urethane was applied the action potential recordings were reduced to zero.

In the animal studies the larger electrodes stimulated a muscle twitch and recorded an action potential at a lower voltage than the smaller electrodes on the device of cuff electrode.

IV. CONCLUSION

Fabrication of cuff electrodes has been achieved and used successfully for stimulating and recording in frog model.

ACKNOWLEDGEMENTS

EU PROJECT SMARTHAND for financial support.

References

[1] R. Riso. "Addition of an intrafasicular electrode at the site of application of a multipolar nerve cuff enhances the opportunity for selective fascicular activation" 2001 Proceedings of the 23rd Annual EMBS International Conference, October 25-28, Istanbul, Turkey

[2] Gregory G. Naples. "A spiral nerve cuff electrode for peripheral nerve stimulation". IEEE transactions on biomedical engineering, vol. 35, no. 11, November 1988.

[3] Martin Schuettler, Thomas Stieglitz. "18polar Hybrid Cuff Electrodes for Stimulation of Peripheral Nerves" Proc. 5th Annual Conf of the IFESS, 2000.

INVESTIGATING THE FUNCTIONAL ROLE OF SLOW WAVES IN BRAIN SIGNAL RECORDINGS DURING REST AND TASK CONDITIONS

C. Demanuele[1], C. J. James[1] and E.J.S. Sonuga-Barke[2]
[1]SPCG, ISVR, University of Southampton, [2]School of Psychology, University of Southampton, Southampton, UK.
cd3@soton.ac.uk

Abstract - Brain imaging studies have provided evidence that very slow neuronal oscillations (<0.5 Hz) are consistently present during different resting states and during task-related activity. This work presents a blind source separation methodology for investigating the functional role of these slow waves in electroencephalographic (EEG) data. Results suggest that both the amplitude and phase of the extracted sources in this frequency band exhibit a significant difference between rest and task conditions, which is in keeping with the view that these slow waves affect resting-state and cognitive brain processes differently.

I. INTRODUCTION

Spontaneous very low frequency oscillations (<0.5Hz), previously regarded as 'physiological noise', have been consistently analysed in blood oxygen level dependent (BOLD) imaging studies. These slow oscillations are thought to arise from variations in metabolic demands in the resting brain and are unrelated to cardiac and respiratory events. However, they also persist during active goal-directed processing where they contribute to inter-trial variability in evoked responses and may present a potential source of attention deficit during task performance. On the other hand, they may be promoting synchronisation between diverse neuronal networks [1]. This study investigates the contribution of these slow waves in electroencephalographic (EEG) data collected from adult healthy controls, during rest sessions (when participants are relaxed, focussing on a cross at the centre of the screen), and whilst performing a Go-Nogo sustained attention to response task (SART). This task imposes a rhythmic load on the brain and is particularly aimed at eliciting the P300 response - a well-studied late event-related (ER) component associated with attention and memory operations [2].

II. THEORY

A. Independent Components analysis (ICA)

ICA is often employed to isolate neurophysiologically meaningful brain sources and artifacts (ocular, muscular, ambient) from the recorded scalp EEG. In the standard ICA model, the sensor measurements $\boldsymbol{x}(t)=[x_1(t),.....,x_n(t)]^T$ are assumed to be made up of a linear instantaneous mixture of independent sources, $\boldsymbol{s}(t)=[s_1(t),.....,s_m(t)]^T$, such that $\boldsymbol{x}(t)=\mathbf{A}\boldsymbol{s}(t)$ where $\mathbf{A}$ denotes the $[n\times m]$ mixing matrix, and $(n\geq m)$. ICA aims to find an unmixing matrix $\mathbf{W}$ ($\mathbf{W}=\mathbf{A}^{-1}$) in order to demix the measurements, such that $\boldsymbol{y}(t)=\mathbf{W}\boldsymbol{x}(t)$, where the m-dimensional vector $\boldsymbol{y}(t)$ contains the independent components (ICs), which are estimates of the underlying sources $\boldsymbol{s}(t)$. Temporal decorrelation source separation (TDSEP) is a specific ICA algorithm which exploits the strong temporal structure inherent in EEG signals and achieves source separation by minimising temporal cross-correlations between the output signals. In essence, TDSEP determines $\mathbf{W}$ by performing joint diagonalisation of several time-lagged covariance matrices, $\mathbf{C}_\tau=\left\langle \boldsymbol{x}(t)\boldsymbol{x}(t-\tau)^T\right\rangle$, such that the source covariance matrix $\mathbf{C}_\tau^s$ is diagonal for all time lags, $\mathbf{C}_\tau^s=\mathbf{W}\mathbf{C}_\tau^x\mathbf{W}^T$ where $\mathbf{C}_\tau^x$ is the signal covariance matrix [3].

B. Hierarchical Clustering of Task ICs

Implementation of ICA on data recorded during task sessions renders three types of ICs: ER (task-related) ICs such as those forming the P300-complex, ICs constituting the background brain activity and artifacts. This grouping is commonly done by visual inspection of the topographies and time series of the estimated sources. We propose a more objective method based on hierarchical clustering as follows: (i) compute the coherent average of the ICs, (ii) find the Euclidean distance between the coherent averages as a measure of similarity, (iii) link pairs of averages which are in close proximity to generate a dendrogram, using (for e.g.) the Ward distance between the binary clusters, and (iv) determine the clusters by selecting an appropriate level on the dendrogram [4].

III. METHOD

We analysed multi-channel scalp EEG recordings of 10 participants. The data was recorded using 25 electrodes placed on the scalp according to the International 10-20 electrode placement system, with a nasal reference. The data was sampled at 250 Hz, downsampled offline to 100 Hz, and low pass filtered at 12 Hz. For each participant TDSEP-ICA was applied to the Rest and SART 5-minute segments separately. The SART ICs were clustered into ER, background and artifactual components using the hierarchical method described above. In order to investigate the slow wave contribution during Rest and SART sessions, the ICs were low pass filtered again from 0-0.5 Hz and their instantaneous amplitude and phase in this frequency band obtained by the Hilbert transform. Finally, for every participant, a direct comparison was performed between the power in the instantaneous slow-wave envelope of the Rest and SART ICs and between the probability density function (pdf) statistics of their instantaneous phases (Fig. 1(d)).

IV. RESULTS

For each Rest and SART data segment TDSEP-ICA extracted 25 components. Fig. 1(a) shows 5 of the 25 Task ICs of one participant; note the clear eye blink component (IC9), a low frequency component (IC11)

and the strongest ER-ICs (IC2, 23 and 24) with central and parietal spatial distributions typical of the P300 complex. The dendrogram of these ICs is illustrated in Fig. 1(c), where the blue cluster corresponds to the background ICs (including IC11), the red and green clusters and the individual branches correspond to the ER components with the exception of IC9 (eye blinks are often time-locked to the visual stimuli thus having a high coherent average). Meanwhile, Rest-ICs show most power in the frontal regions (due to visual fixation) and occipital regions (alpha power associated with relaxation and absence of task-engagement), Fig. 1(b).

For each participant, the total power in the slow-wave envelope of all 25 ICs (taking into account the portion of the power residing in the corresponding column of the mixing matrix), for a Rest and SART segment separately, was found in order to obtain the overall power in the slow-wave band for that dataset in that condition. Across participants, the median power in the slow-wave band was significantly higher during Rest than during the SART (p-value = 0.0966), whilst the mean kurtosis of the slow-wave phase during SART was significantly higher than that during Rest (p-value = 0.0148).

V. CONCLUSION

In this paper we highlight a methodology for analysing the functional role of neural slow wave activity during rest and during an externally imposed cognitive task. Evidence in the literature suggests that these very low frequency oscillations may not be apparent in the data as independent components per se but rather as a mechanism that modulates and perhaps even governs underlying brain processes [1]. Preliminary results demonstrate that both the instantaneous amplitude and phase of the ICs within the 0-0.5 Hz band are exhibiting consistent variations in the two scenarios. Future work will focus on developing a more robust method of comparison between the two conditions and between the individual SART component clusters and the Rest ICs.

REFERENCES

[1] M.D. Fox, & M.E. Raichle, "Spontaneous fluctuations in brain activity observed with functional magnetic resonance imaging". Nature Reviews Neuroscience, vol. 8, 2007, pp. 700-711.

[2] J. Polich, "Updating P300: An integrative theory of P3a and P3b", Clinical Neurophysiology, vol. 118, 2007, pp. 2128-2148.

[3] A. Ziehe and K. Muller. "TDSEP - an efficient algorithm for blind source separation using time structure". ICANN, vol. 98, 1998, pp. 675-680.

[4] B. Everitt, *Cluster Analysis*, Edward Arnold, New York, 3rd Ed., 1993.

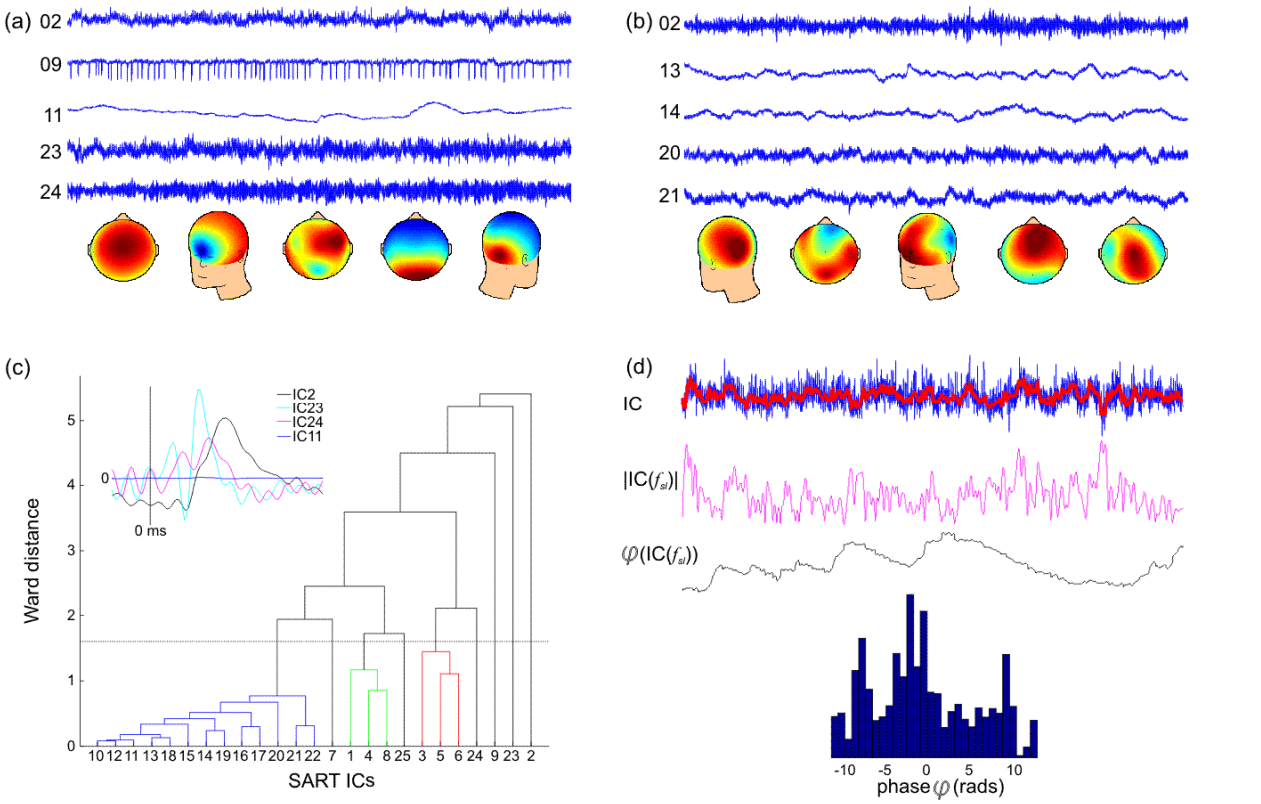

Fig. 1. Outline of the procedure for objective analysis of slow waves during Rest and SART conditions, (Results of 1 participant shown as an example). (a) Five of the 25 ICs and their spatial distribution extracted by TDSEP-ICA during SART and (b) during Rest. (c) Dendrogram built on the coherent averages of the SART ICs (selected traces shown): blue cluster corresponds to the background ICs, the red and green clusters and the individual branches correspond to the large ER-ICs and the artifacts (IC9). (d) One IC (blue trace), 0-0.5 Hz filtered IC (superimposed red trace), the instantaneous amplitude $|IC(f_{sl})|$ and phase $\varphi(IC(f_{sl}))$ of the filtered IC; the instantaneous slow-wave phase pdf.

GENERATION OF COLLAGEN MICROPATTERN BY PRINTING

A. Zarowna[1], E. Gu[1*], E.O. McKenna[3], M.D. Dawson[1], A. Pitt[3], J.M. Cooper[2], H.B. Yin[2*]
[1]Institute of Photonics, University of Strathclyde, Glasgow, UK
[2]Bioelectronics Research Centre, University of Glasgow, Glasgow, UK
[3]Faculty of Biomedical & Life Sciences, University of Glasgow, Glasgow, UK
erdan.gu@strath.ac.uk, and hy@elec.gla.ac.uk

Abstract – Cell patterning is a powerful technique to study cell behaviour under controlled micro-environments. However, methods used to create cell patterns are far from trivial. In this work, we are developing a simple and benign approach for generation of cell patterns through adhesive protein (e.g. collagen) micropatterns. The use of commercial piezoelectric printers for the formation of collagen micropatterns is presented.

I. INTRODUCTION

Cell patterns provide a versatile platform for cell manipulation and systematic *in vitro* studies. These have found increasing applications in life science, tissue engineering, diagnostics and the pharmaceutical industry [1]. It is well known that living cells can recognise and preferentially attach to the extracellular matrix (ECM) proteins that are naturally present in a body. Thus, the employment of an adhesive protein pattern to "coax" specific cell attachment in particular locations becomes an attractive approach. An additional non adhesive treatment of the spaces between the individual protein patterns would further constrain cells to selectively adhere on the protein patterns.

Collagen, as the most abundant ECM protein and the main component for all the connective tissues, has been widely used for *in vitro* cell culture [2]. Several methods for the generation of collagen patterns have been developed, such as photolithography and different methods of printing: micro-contact or microfluidics printing [3-5]. Although these methods are able to create high resolution patterns (e.g, 20 - 200 µm in ref. [4]; 2 µm in ref. [5]), they involve multi-step processes in clean room facility and exposition to denaturising conditions such as UV irradiation and organic solvent washing. These methods are difficult to reproduce in biology labs [6].

Inkjet printing is a simple, high throughput technique for the generation of small biomolecule microarrays. It avoids exposure of the biomolecules to any denaturising factors, thus preserving their native functionality. Surprisingly, the use of inkjet printing of collagen is rare; the smallest dimension of collagen pattern that has been so far generated by this method is 350 µm [7].

A protein (or multiple protein) pattern with arbitrary arrangement and dimensions ranging from tens to hundreds of microns allows flexible and specific manipulation of cell types and cell numbers, which is essential in quantitative cellular analyses. In this study we exploit inkjet printing for the generation of collagen micropatterns of resolution down to tens of microns, with the aim of developing a robust, flexible and non invasive method for subsequent cell pattern formation and cell based toxicity analysis.

II. MATERIALS AND METHODS

Dry collagen from calf skin, type I (Sigma) was dissolved in 0.1M acetic acid and the pH was adjusted to a physiological level of 7.4 with NaOH solution. This stock solution was further diluted with phosphate buffered saline (PBS) solution to concentrations of interest. For easy visualisation of printed collagen patterns, fluorescein sodium (Sigma) was added to the collagen solution to a final concentration of 1 µM.

Collagen solutions were printed using either a Dimatix® ©FUJIFILM inkjet printer or PerkinElmer® Packard™ BioChip Arrayer™. Dimatix® allows precise deposition of 10 pl volume of a solution, whilst a PerkinElmer® system, is capable of using a minimum printing volume of 330 pl. In both cases, the printing voltage and, where relevant, pulse width were tuned to an optimal operating value to minimise satellite droplet formation.

III. RESULTS AND DISCUSSION

For generation of collagen patterns of tens of microns, 10 pl droplets of a collagen solution were printed using the Dimatix® system. Figure 1A shows the micropattern formed on untreated glass substrate when printed at collagen concentration of 0.1 mg/ml. Although the main individual spots of ~30 µm diameter are highly reproducible, they are accompanied by a satellite dot. This is mainly due to the high surface tension of collagen solution (~66 10^{-3}N/m [8]), which is far beyond the optimum operation range (28-30 10^{-3}N/m) for the system.

To reduce the surface tension of the collagen solution, three surfactants, Pluronic 127, Tween 80 and Tween 20 were added at concentrations of 0.1%, 0.1% and 0.01% respectively. At these concentrations, the

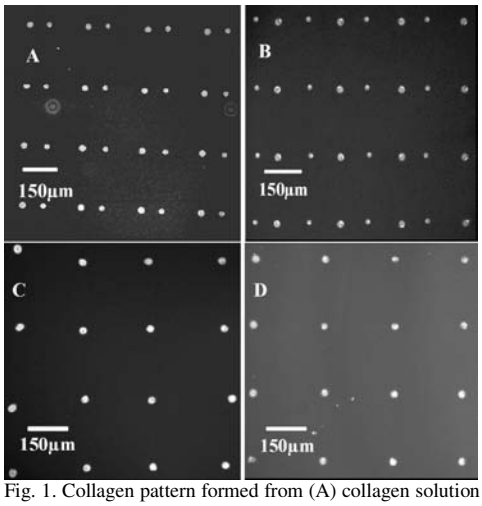

Fig. 1. Collagen pattern formed from (A) collagen solution only; Collagen solution with (B) 0.1% Pluronic F127, (C) 0.01% Tween 20 and D) 0.1% Tween 80. Collagen concentration is fixed at 0.1 mg/ml.

surfactants have no effect on cell proliferation and viability [9, 10]. It has been found that the addition of 0.01% Tween 20 or 0.1% Tween 80 but not Pluronic 127 eliminates the formation of satellite droplets, as shown in Figure 1 B, C and D. Under these conditions, uniform collagen patterns of diameters as small as 30µm have been generated.

Using optimised printing conditions, the same dimensions of collagen spots have been formed on a number of substrates, including an ultraclean glass and a glass coated with thin porous layer of agarose. This suggests a rapid drying-out of such small amounts of printing solution which limits the diffusion of the solution to the surroundings. An additional benefit of this is that multilayer printing of the solution on the same spot is highly efficient, allowing easy modulation of the density of collagen within each spot with negligible alteration of the spot dimension. Figure 2A shows a typical 30 µm collagen pattern prepared by single printing and figure 2B represent 35 µm diameter pattern prepared by the sequential printing of five layers.

Similar principles apply to the PerkinElmer® Piezorray™ spotter system. Using the minimum jet-printing volume of 330 pl, a precise 100 µm collagen spot is formed. Thus, the dimensions of individual collagen spots can be modulated by the volume of the printing solution.

VI. CONCLUSION

We present a simple and robust method to prepare highly uniform collagen micropatterns of dimensions ranging from tens to hundreds of microns with tuneable densities using

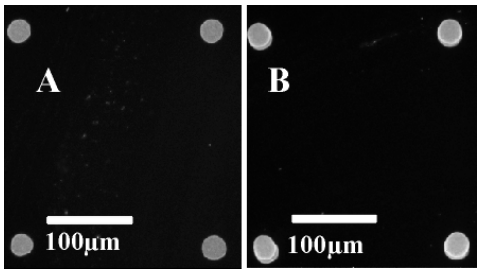

Fig. 2. Pattern formed on a thin agarose layer coated glass (A) one layer printing (B) 5 layers printing. A 0.1% agarose solution was used for coating a glass surface.

commercial inkjet systems. The collagen patterns serve as adhesive motifs to promote selective cell attachment and proliferation; cell culture tests on these patterns are currently in process.

ACKNOWLEDGEMENTS

This work has been supported by SFC, BBSRC and EPSRC through funding of the SCIMPS and RASOR projects. HY is supported by the Royal Society of Edinburgh as a Personal Research Fellow.

REFERENCES

[1] H. Zhu, M. Macal, C.N. Jones, M.D. George, S. Dandekar, A. Revzin, A miniature cytometry platform for capture and characterization of T-lymphocytes from human blood, Anal. Chim. Acta 608 (2008) 186-196.
[2] M. Alaminos, M.D. Sanchez-Quevdo, J.I. Munoz-Avila, D. Serrano, S. Medialdea, I. Carreras, A. Campos, Construction of a complete rabbit cornea substitute using a fibrin-agarose scaffold, Investigative Ophthalmology & Visual Science 47 (2006) 3311-3317.
[3] D.I. Rozkiewicz, Y. Kraan, M.W.T. Werten, F.A. de Wolf, V. Subramaniam, B.J. Ravoo, D.N. Reinhoudt, Covalent microcontact printing of proteins for cell patterning, Chem.-Eur. J. 12 (2006) 6290-6297.
[4] E.E. Hui, S.N. Bhatia, Microscale control of cell contact and spacing via three-component surface patterning, Langmuir 23 (2007) 4103-4107.
[5] M.R. Hynd, J.P. Frampton, N. Dowell-Mesfin, J.N. Turner, W. Shain, Directed cell growth on protein-functionalized hydrogel surfaces, J. Neurosci. Methods 162 (2007) 255-263.
[6] J. Fink, M. Thery, A. Azioune, R. Dupont, F. Chatelain, M. Bornens, M. Piel, Comparative study and improvement of current cell micro-patterning techniques, Lab Chip 7 (2007) 672-680.
[7] E.A. Roth, T. Xu, M. Das, C. Gregory, J.J. Hickman, T. Boland, Inkjet printing for high-throughput cell patterning, Biomaterials 25 (2004) 3707-3715.
[8] P. Dynarowicz, M. Paluch, J. Rychlicka, Surface-Properties of Aqueous-Solutions of Trifluoroacetic and Acetic-Acid Mixture, Colloid Polym. Sci. 267 (1989) 451-455.
[9] D. Dimitrijevic, A.J. Shaw, A.T. Florence, Effects of some non-ionic surfactants on transepithelial permeability in Caco-2 cells, J. Pharm. Pharmacol. 52 (2000) 157-162.
[10] S.F. Khattak, S.R. Bhatia, S.C. Roberts, Pluronic F127 as a cell encapsulation material: Utilization of membrane-stabilizing agents, Tissue Engineering 11 (2005) 974-983.

New methods for assessing the control of blood flow in the brain

H. Kouchakpour[1] Dr D.M. Simpson[1] Dr T. Birch[2] Prof R.Allen[1]

[1]ISVR, University of Southampton, Southampton, UK
[2]Department of Medical Physics and Bioengineering, NHS Hospital, Southampton, UK

hk803@soton.ac.uk, ds@isvr.soton.ac.uk, ra@isvr.soton.ac.uk, tony.birch@suht.swest.nhs.uk

Abstract - The aim of this study is to investigate different methods for estimating dCA from spontaneous variations in blood flow and pressure using time and frequency domain analysis, to compare estimates and identify the most appropriate approach. In the current preliminary study, results from four healthy adult volunteers are analysed, and parameters from time- and frequency-domain estimates are compared.

I. INTRODUCTION

Cerebral autoregulation (CA) refers to the ability of the brain's blood vessels to preserve cerebral blood flow (CBF) during fluctuations in arterial blood pressure (ABP) (Aaslid, 1989). CA attracts considerable attention as it is thought to be an important mechanism in the development of some strokes, and also in the occurrence of the secondary damage, following stroke. The physiological control system is highly complex and is not fully understood in spite of extensive research that has been carried out in this area.

Through technological advances over the last two decades cerebral autoregulation has been evaluated by measuring relative cerebral blood flow (CBF) response to a steady-state (static) change in the ABP or the response to a sudden and rapid change in the blood pressure (dynamic response). Most recent work on cerebral autoregulation has focused on the transient response, known as *dynamic cerebral autoregulation* (dCAR). It has been shown that dynamic and static autoregulation have significant correlation for healthy human subjects (Aaslid, 1989). dCA can be quantified from the relationship between ABP and cerebral blood flow (CBF) through the use of appropriate signal processing methods(Aaslid, 1989). This can even be carried out even in the presence of only spontaneous variations of blood pressure which is clearly ideal as it avoids major interference with the patient. However, none of the methods of estimating dCA have been found to be sufficiently robust to be considered a 'gold standard' nor have they been used routinely in clinical practice. Patients at risk from haemodynamic brain damage have thus not yet benefited from the extensive investment and considerable progress made in this field over the last two decades, and much clinical and physiological research has had to rely on less than optional techniques. Thus more research on reproducibility and method comparison is urgently needed in this field.

II. TECHNICAL INFORMATION

In four healthy adult volunteers blood pressure and cerebral blood flow were measured for the duration of around 50 minutes with the subjects at rest. During this time, volunteers breathed ambient air and air enriched with 5% CO2 through a face-mask. The latter provokes hypercapnia, known to temporarily impair autoregulation. The time series of spontaneous arterial blood pressure and cerebral blood flow velocity were collected with Finapres and transcranial Doppler ultrasound devices, respectively. In three subjects the recordings were repeated. Data were visually inspected to ensure good quality. Beat-averaged (mean) blood flow velocity (MCBFV) and arterial blood pressure signals (MABP) were then obtained by low-pass filtering (cut-off frequency = 0.5 Hz; zero phase filter) to remove within-beat variations. In accordance with previous work, the relationship between MABP (input) and MCBFV (output) was then modeled by a linear filter (Wiener Filter), estimated in the time and frequency domains. The important distinction between these approaches for the current work is that the former provides a causal filter, whereas the latter can include a non-causal component in the impulse response. In previous work it has been shown that autoregulation can be estimated from the gain or phase-lead in the frequency response at around 0.1 Hz. Coherence can also provide an estimate of autoregulation. High coherence is expected when flow passively follows pressure in the absence of active autoregulation.

III. RESULTS

An example of the estimated step- and frequency response (gain and phase) can be seen in Figure 2-3. As can be seen from Figure 2-3, the step response has less overshoot for hypercapnia compared to normocapnia, indicating reduced autoregulatory activity. The effect of CO2 is not very clear on the gain plot, with increased (rather than reduced) gain during hypercapnia – indicating that results are not always as clear as might be expected. The phase plot agrees with our expectations, where a larger phase-lead can be seen for normocapnia (active autoregulation). The results drawn from these experiments shows that the overall error of the estimation using time and frequency analysis are almost the same for time- and frequency domain approaches (SNR = 4.1673 and 4.3159, respectively).

Summary results for the effect of CO2 level on autoregulation estimates using both time and frequency domain estimation can be seen in Figure 5, where the phase has decreased compared to normal CO2 is evident in most cases; for gain, the distinctions between normo- and hypercapnia is less clear. The clearest distinction between normo and hypercapnia can be seen in the frequency-domain estimates of phase. Similar plots for coherence at 0.1 Hz show no clear change between experimental conditions.

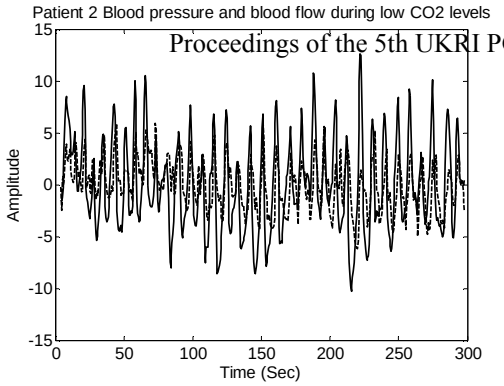

Figure 1 Patient 2 blood pressure (dashed line) and cerebral blood flow (bold line) during normocapnia

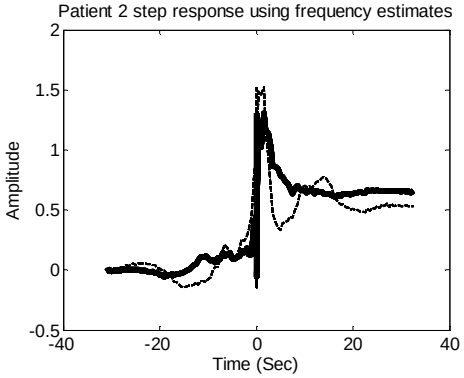

Figure 2 Step response from Frequency estimate for both normocapnia and hypercapnia. (Bold line is for High CO2 and dashed line is for normal CO2 levels).

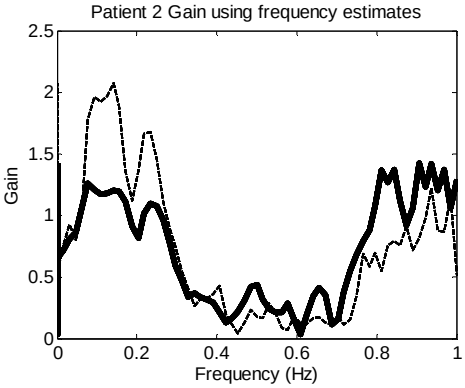

Figure 3 Gain from Frequency domain estimate

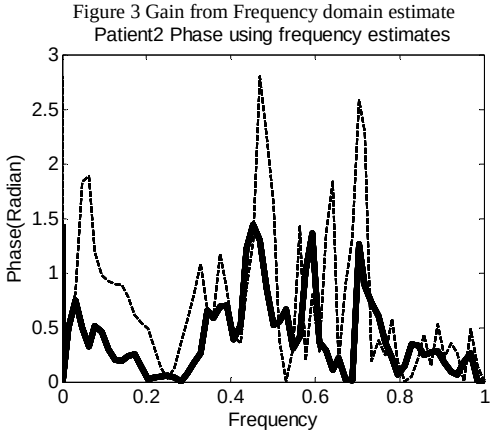

Figure 4 Step response from Frequency domain estimate

By considering the results from time and frequency domain analysis, the agreement between them is considerable with strong correlation as evident (correlation coefficient of .58 and 0.66, respectively).

IV. CONCLUSION

These preliminary results for both time and frequency domain analysis agree roughly with reports in the literature. Phase is again found to provide a stronger distinction between the experimental protocols, but large inter-individual variability makes it difficult to determine thresholds for normal/impaired autoregulation. Results for coherence were disappointing: one reason may be that the power spectrum of our signals has very narrow peaks, in which case coherence estimates can be unreliable.

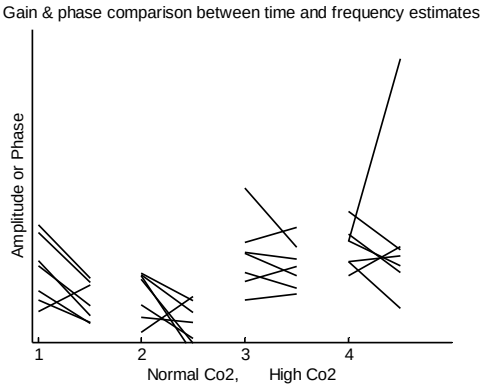

Figure 5 Autoregulation comparison for normal (left side of the lines) and high CO2 (right side of the lines) levels for volunteers 1. Phase from Frequency, 2. Phase from Time, 3. Gain from Frequency, 4. Gain from Time

It can be seen that results from time- and frequency domain methods follow the same trend but with considerable scatter; there is also clear bias in phase estimates, with time-domain results being lower.

The small size of the sample analyzed, the short segments of recordings available, and the absence of a "gold standard" measurement do not currently allow strong inferences regarding which method should be preferred. Clearly the random errors in estimates are large and require caution in the assessment of autoregulation. The ability to predict the reliability (estimation errors) of autoregulation estimates from individual recordings is clearly highly desirable. In future work, non-linear, time-varying and multivariate models (with CO2 variations as an additional input) will be investigated. New experimental protocols, in which higher variations in blood pressure are induced, will also be studied, with the aim of increasing the robustness of autoregulation estimates.

Acknowledgments: *EPSRC* are acknowledged for support of this work.

REFERENCES

[1] *Cerebral autoregulation dynamics in humans.* Aaslid, R., K.-F. Lindegaard, W. Sorteberg, and H. Nornes. s.l. : Stroke, 1989. 20:45-52.

[2] *A Parametric Approach to Measuring Cerebral Blood Flow Autoregulation from Spontaneous Variations in Blood Pressure.* DAVID M. SIMPSON, 1 RONNEY B. PANERAI,1 DAVID H. EVANS,1 and A. ROSS NAYLOR. s.l. : Annals of Biomedical Engineering, Vol. 29. 18–25, 2001..

[3] *Multivariate system identification for cerebral autoregulation.* TINGYING PENG, 1 ALEXANDER B. ROWLEY,1,2 PHILIP N. AINSLIE,3,4 MARC J. POULIN,3 and. s.l. : Annals of Biomedical Engineering, 2007, Annals of Biomedical Engineering, pp. 308-320.

[4] *Frequency-domain analysis of cerebral autoregulation from spontaneous fluctuations in arterial blood pressure.* R. B. Panerai I J, M. Rennie 2 A.W.R. Kelsall 2 D.H. Evans. 36, Leicester : Medical.& Biological Engineering & Computing, 1998.

[5] *Multiple coherence of cerebral blood flow velocity in humans.* Panerai, R. B., P. J. Eames, and J. F. Potter. s.l. : Am. J. Physiol. Heart Circ. Physiol, 2006, Vols. 291(1), July 2006.

THE SEARCH FOR POINT OF CARE ASSAYS: A MODEL SYSTEM FOR HOMOGENEOUS FRET IMMUNOASSAYS BASED ON LANTHANNIDES

Peter D. Dowd[1], Jan Karolin[2], Carol Trager-Cowan[2], David J.S. Birch[2], William H. Stimson[3]

[1]Strathclyde Institute of Medical Devices, Bioengineering Unit, Wolfson Centre, University of Strathclyde, 106 Rottenrow, Glasgow G4 0NW, United Kingdom. [2]Department of Physics, University of Strathclyde, [3]Strathclyde Institute of Pharmacy and Biomedical Sciences, University of Strathclyde

pd.dowd@strath.ac.uk,

Abstract – The purpose of this research is to discover if a method currently being developed for pathogen and toxin detection in the food and biosecurity markets can be applied to the medical 'point of care' market. A test system based on lanthanide chelates and fluorophores bound to antibodies, or antibody fragments, is proposed as a starting point for the quantifying of the energy transfer efficiency in such assays.

I. INTRODUCTION

Healthcare is currently under mounting pressure due to rising costs and society's ever-increasing expectations. As a result, these factors are driving the way care is provided. One area which has the potential to change rapidly is the service provided by diagnostic testing where there will be a shift away from centralised laboratory testing to 'point of care testing'. To aid diagnosis, the point of care test must deliver a result quickly and simply in order that an appropriate treatment can be administered immediately. In addition, instruments designed for this purpose must also be compact, robust and inexpensive [1]. The aim of this research is to discover if a method currently being developed for pathogen and toxin detection in the food and biosecurity markets using time resolved fluorescence resonance energy transfer (TR-FRET) can be applied to the medical 'point of care' market and, more specifically, as a diagnostic or prognostic tool for coronary artery disease (CAD).

The proposed method of detection is the application of the phenomenon time resolved luminescence-resonance energy transfer (TR L-RET), between lanthanides and fluorescent labelled antibodies, to a competitive homogeneous assay.

RET

RET is a distance dependent phenomenon and is used as a method to measure the distance, *R*, between a donor (D) and an acceptor (A) molecule [2]. RET works on the principle that light quanta absorbed by a donor are transferred to an acceptor molecule (where the transfer between donor and acceptor is non-radiative). The energy may be transferred to the acceptor molecule only when the donor and acceptor are within a suitable distance and furthermore, only when there is a spectral overlap between the emission of the donor and the absorption of the acceptor.

Thus by measuring the relative fluorescence intensities of the donor in the presence and absence of the acceptor the efficiency of the energy transfer can be quantified and used to calculate the distance between the donor and acceptor molecules and also the concentration of the analyte or substrate in the system.

Lanthanide Ion Chelates and L-RET

Lanthanide trivalent ions have favourable characteristics for application in RET immunoassays. For example, lanthanides exhibit a relatively long-lived luminescence with decay times typically 0.5 to 3 ms compared with the short-lived (typically nanosecond) background sample fluorescence [3].

Unfortunately lanthanide ions have the disadvantage that they have weak absorption coefficients and lanthanide luminescence is easily prohibited, or quenched, by the ligand interactions of water and hydroxide molecules. To overcome the low extinction coefficient the lanthanide ion is indirectly excited by a 'sensitiser'. This is commonly referred to as the 'antenna effect' [4]. The sensitiser is an organic chromophore which forms part of, or is attached to, the protecting chelate structure. The chelate also functions as a scaffold for the lanthanide ion and provides a reactive group for binding to biomolecules. The sensitiser absorbs the excitation light and transfers this energy to the lanthanide ion.

Homogeneous L-RET Competition Assay

Ideally, the homogeneous assay would consist of a lanthanide chelate bound to a substrate and mixed, in solution, with free antibody (which is labelled with a fluorescent marker). When the free antibody binds to the substrate at a

distance close enough, and for a long enough period of time, RET occurs. The lanthanide chelate is excited and the total donor and total acceptor emissions are measured. By adding antigen, which preferentially binds to the free antibody in solution, the RET between donor and acceptor fluorophore will be reduced, thus providing a direct competition mechanism for detecting the presence of the antigen. Therefore, quantifying the change in the ratio of donor intensity to acceptor intensity would give a measure of the amount of antigen present in the sample and provide a simple measurement method for a potential point of care device.

II. METHODS

As a starting point, we suggest adopting a 'bottom-up' approach, identifying a simple model system where the L-RET interaction can be demonstrated between two molecules in a well characterised biosystem. An ideal test system would have the donor and acceptor molecules bound to specific sites on the substrate (in this case the antibody) and separated by a unique distance *r*. However, each antibody offers two potential binding sites for each antigen and possibly multiple binding sites for the donor molecules. This may result in a range of donor-acceptor distances which, in turn, would lead to multiple contributions to both the fluorescence intensity of the donor and the fluorescence intensity of the acceptor [5].

To counter the problem of 'multiple distances' we are currently considering a system which involves the peptide [des-pGlu^1]-LH-RH (conjugated with FITC) bound to an antibody (7B10.1D10) Fab fragment. The advantage is that by making the substrate an antibody Fab fragment (and therefore setting the number of antigen binding sites to one per substrate) we reduce the number of competing donor-acceptor distances contributing to the overall energy transfer efficiency of the assay. Moreover, [des-pGlu^1]-LH-RH is a fragment of the hormone GnRH-1 with both peptides thought to have the same binding site (gly-leu-arg) for the antibody 7B10.1D10 [6]. Therefore it may be possible to detect the amount of GnRH-1 in a sample by measuring the changes in the fluorescence intensities of the donor and acceptor as the GnRH-1 competes with the [des-pGlu^1]-LH-RH.

The primary objective in this investigation is to describe the photophysical behaviour of the assay as fully as we can by quantifying the energy transfer efficiency, using well established time-resolved fluorescence spectroscopy techniques. Complementary to this, circular dichroism and tryptophan fluorescence techniques will be used to uncover information about the structure of antibody Fab fragment and both peptides. Furthermore, by sequencing the antibody Fab fragment we will be able to identify potential binding sites and, by relating this to the structure, estimate donor-acceptor distances and compare them with distances calculated from RET efficiency measurements.

III. DISCUSSION

Combining the advantages of chelated lanthanide trivalent ions with an antibody platform that will bind a single antigen may make it possible to design an L-RET immunoassay that can be comprehensively described in terms of FRET theory [7]. Yet there are likely to be limitations to the test system such as incomplete antigen and donor binding to the Fab fragment, multiple donors binding to the Fab fragment and Fab fragment interactions. Therefore the challenge is to optimise the assay, determine if the intensity ratio can be used as a meaning full detection method for a POC device and demonstrate that the general principles of the assay can be applied to the detection of other peptides.

IV. CONCLUSION

A strategy for evaluating the photophysics of lanthanide based immunoassays using fluorescence resonance energy based techniques has been identified in an effort to establish its potential as a detection method in medical diagnostics.

REFERENCES

[1]. Price C.P. 2001 Clinical Review: Point of Care Testing. *BMJ*, 322:1285-1288

[2]. Stryer L & Haugland R.P., 1967 Energy Transfer: A Spectroscopic Ruler *Proc. Natl. Acad. Sci. USA* 58, 719–726

[3]. Sabbatini N, Casnati C, Fischer R, Girardini M, Guardigli I, Manet I Sarti G and Ungaro R 1996 Luminescence of Eu 3+ and Tb 3 + complexes of new macrobicyclic… *lnorganica Chimica Acta* 252: 19-24

[4]. Weissman SI, 1942 Intramolecular Energy Transfer the Fluorescence of Complexes of Europium *J. Chem. Phys.* 10, p. 214

[5]. Lakowicz J.R. Principles of Fluorescence Spectroscopy, 3rd ed. Kluwer Academic/Plenum Publishers, New York City, New York, 2006

[6]. Kahn M.A.H., Ferro V.A., Stimson W.H. 2003 Use of a Highly Specific Monoclonal Antibody Against… *AJRI* Vol 49: 239-248

[7]. Selvin P.R. 2002 Principles and Biophysical Applications of Lanthanide-based Probes. *Annu Rev. Biophys. Biomol. Struct*., 31:275-302

AN INTRODUCTION TO THE BISPECTRUM FOR EEG ANALYSIS

D. Wong, D.A. Clifton, L. Tarassenko

Biomedical Signal Processing Group, Institute of Biomedical Engineering, University of Oxford, Oxford, UK

wong@robots.ox.ac.uk

Abstract - This paper provides a tutorial for bispectral analysis, a signal processing technique commonly used for the analysis of the Electroencephalogram (EEG). The use of this technique has been hindered by popular misconceptions deriving from existing tutorial papers.

INTRODUCTION

Analysis of EEG is typically performed using Fourier analysis, which is useful for detecting frequency components that correspond to the mental state of a patient. Typically, such information is obtained from the magnitude spectrum, as the information content of the phase spectrum can be harder to interpret.

Although use of the magnitude spectrum is sometimes sufficient, in many instances, the phase information is critically important. Bispectral analysis offers a way of gaining further phase information by detecting phase relationships between frequency components. Such relationships have been shown to exist in a medical context during periods where a patient has an impaired mental state (for example see [1]).

The rest of this paper outlines the mathematical principles behind the bispectrum, and provides simple examples that demonstrate its use. Using the knowledge gained from the tutorial, we will dispel a commonly-held misconception.

II. BISPECTRUM TUTORIAL

Bispectral analysis makes use of phase information by detecting whether the phase of signal components at frequencies f_1, f_2, and f_3 are interdependent. Furthermore, the degree of dependence is quantified so that a high bispectrum correlates to a signal with highly interdependent frequency components.

Knowing this, it makes intuitive sense that the bispectrum can be calculated from using the Fourier transform of a signal evaluated at f_1, f_2, and f_3. The bispectrum of x can be expressed mathematically as

$$B(f_1, f_2) = \frac{1}{k}\sum_{i=1}^{k} X_i(f_1)X_i(f_2)X_i^*(f_1 + f_2) \quad (1)$$

where X denotes the Fourier transform of x. In this case, the signal has been split into k time segments that we call epochs, and

$$X_i(f_1)X_i(f_2)X_i^*(f_1 + f_2) \quad (2)$$

is the triple product. Using the convolution theorem for Fourier transforms, the bispectrum of a process, x, is formally defined as:

$$B_x(f_1, f_2) = \sum\sum c_3(\tau_1, \tau_2)e^{-j2\pi(f_1\tau_1 + f_2\tau_2)} \quad (3)$$

where $c_3(\tau_1,\tau_2)=E\{x_t,x_{t+\tau 1},x_{t+\tau 2}\}$, and $E\{.\}$ is the expectation operator.

Although other methods of calculating the bispectrum are also used in practice, the examples below use equation 1 for the sake of clarity.

A. Quadratically Phase Coupled Components

Three sinusoid components, x_1,x_2 and x_3, of a signal are quadratically phase coupled (QPC) if the frequency and phase of the x_3 component is equal to the sum of the frequencies and phases of the x_1 and x_2 components. For example, for

$x_1 = \cos(f_1 + \phi_1)$, $x_2 = \cos(f_2 + \phi_2)$, $x_3 = \cos(f_3 + \phi_3)$ the components are QPC only if $f_1+f_2=f_3$ and $\phi_1 + \phi_2 = \phi_3$

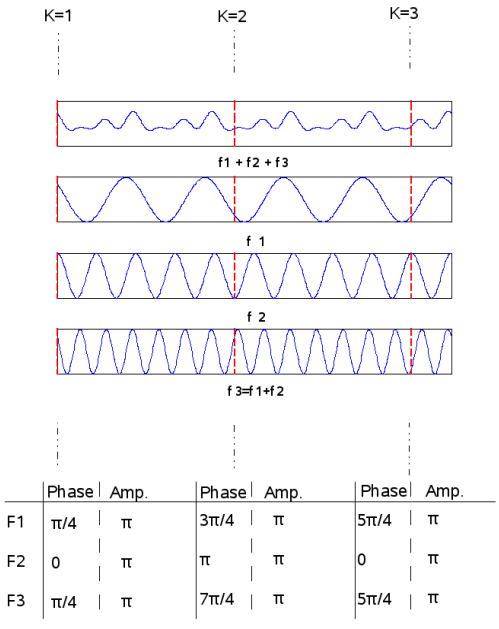

Figure 1: A graphical interpretation of the bispectrum calculation for a synthetic QPC signal. The signal is shown above its three component sinusoids.

A simple QPC signal, along with its component sinusoids, is shown in Fig. 1. The signal is split into *k=3* epochs (where the third

epoch is truncated), and the component frequencies and phases are calculated at the start of each epoch. The triple products can then be calculated using eq. 2:

$$K = 1: \ \pi e^{\frac{j\pi}{4}} \times \pi e^{j(0)} \times \pi \, e^{\frac{-j\pi}{4}} = \pi^3$$
$$K = 1: \ \pi e^{\frac{j3\pi}{4}} \times \pi e^{j\pi} \times \pi \, e^{\frac{j7\pi}{4}} = \pi^3$$
$$K = 1: \ \pi e^{\frac{j5\pi}{4}} \times \pi e^{j(0)} \times \pi \, e^{\frac{j5\pi}{4}} = \pi^3$$

The mean of the triple products gives the estimate of the bispectrum. In this case, $B(f_1,f_2)=\pi^3$

B. Non-Quadratic Coupling

Figure 2 shows a similar system, but where the components are no longer QPC, as $\phi_1 + \phi_2 \neq \phi_3$. However, the phases are *coherent*, meaning that the relative phase between any of the components does not change over time. Triple products are calculated as before, resulting in $|B(f_1,f_2)|=\pi^3$.

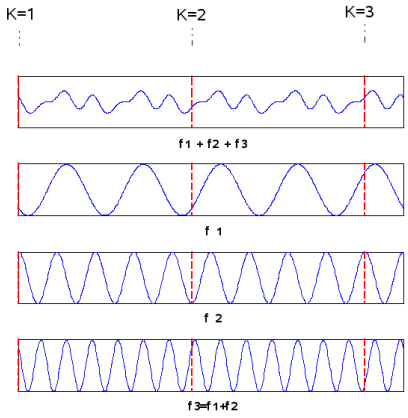

	Phase	Amp.	Phase	Amp.	Phase	Amp.
F1	3π/4	π	5π/4	π	7π/4	π
F2	0	π	π	π	0	π
F3	π/4	π	7π/4	π	5π/4	π

Figure 2: A graphical interpretation of the bispectrum calculation for a non-QPC, coherent, synthetic waveform.

C. Incoherent components

The third example, which is not pictured here for brevity, assumes a non-QPC and non-coherent set of component sinusoids. By non-coherent, it is meant that the relative phases between the sinusoids change over time, so ϕ_1, ϕ_2, ϕ_3 are time-dependent variables.

In this case, the estimate of the bispectrum is once again calculated from equation 2 to give $\frac{\pi^3}{2.08} e^{j(0.6\pi)}$. The magnitude of the bispectrum is much less than in the other examples. In fact, for incoherent signals, the bispectrum tends toward zero when a larger number of epochs are used.

III. DISCUSSION

This tutorial has demonstrated that the bispectrum can be used to identify phase coherence between any three sinusoids that are components of a signal. The coherence is detected for QPC components (example A), for coherent, but non-QPC components (example B), but not for incoherent signals where the relative phase between two fundamentals changes over time (example C).

Previous tutorial papers on the bispectrum, including those by Sigl and Chamoun [2], Nikias and Raghuveer [3], Shen [4], and Holt [5], have asserted that the technique is only valid for QPC signals. They each give a simple system such as:

$$y_1(k) = 1 + \cos(f_a k + \theta_a) + \cos(f_b k + \theta_b) + \frac{1}{2}\cos(f_c k + \theta_c) + \frac{1}{2}\cos(f_d k + \theta_d)$$

and apply the constraints $f_a = f_1 + f_2$, $f_b = f_1 - f_2$, $f_c = 2f_1$, $f_d = 2f_2$, and $\theta_a, \theta_b, \theta_c, \theta_d$ are random and independent so that the mixture is *not* QPC.

They go on to state that such a system will result in a zero bispectrum over all the frequency space. However, this assertion is incorrect and inconsistent with example B.

In both example B and the system described above, the phases are set to be random constants. Thus, the signal components are coherent as there is no relative phase drift between them, and the bispectrum will be significant.

In conclusion, we have sought to provide an intuitive guide to the bispectrum using a graphical explanation, and have proceeded to show that previous literature on the subject is confusing and misleading.

REFERENCES

[1] J Jeong. EEG dynamics in patients with Alzheimer's disease. *Clin. Neurophysiology*, 115:1490-1505, 2004

[2] JC Sigl and NG Chamoun. An introduction to bispectral analysis for the electroencephalogram. *J. Clin. Monitoring and Comp.*10(6):392-404, 1994

[3] CL Nikias and MR Raghuveer. Bispectrum estimation: a digital signal processing framework. *Proc. of IEEE*, 75(7):869-891, 1987

[4] M Shen, F Chan, L Sun, P Beadle. Parametric bispectral estimation of EEG signals in different functional states of the brain. IEE Proc. Science, measurement and tech. 147(6):374-377,2000

[5] M Holt. *The use of neural networks in the analysis of the anaesthetic EEG.* PhD thesis, U.Oxford, 1997

FREQUENCY DOMAIN ANALYSIS FOR THE STUDY OF ATRIAL ARRHYTHMIAS

Ahmad A.[1, 3], Schlindwein, F.S.[1], Tuan J.H[2], G. Andre´ Ng[2]

[1]Department of Engineering, University of Leicester, Leicester, LE1 7RH, UK

[2]Cardiology Group, Department of Cardiovascular Sciences, University of Leicester, LE3 9QP, UK

[3]Faculty of Electrical Engineering, Universiti Teknologi Malaysia,81310 Skudai Johor Malaysia

aa384@le.ac.uk, fss1@le.ac.uk, jht8@le.ac.uk, gan1@le.ac.uk

Abstract - In the United States of America, cardiac arrhythmias remain the leading cause of sudden death with more than 300,000 cases per year [1]. The majority of sustained cardiac arrhythmias are atrial fibrillation and these contribute a major cause of stroke [2-5]. Irregular electrical pulses can be determined inside the atria. Frequency analysis is used to measure changes in the dominant frequency (DF). Welch method is used here to obtain the frequency spectrum of the signals. The 3D frequency strength plotting allows us to identify the evolution of the frequency composition of the signal with time.

Keywords: Atrial Arrhythmias, Atrial fibrillation, Electrocardiograms, frequency analysis

I. INTRODUCTION

The commonest heart rhythm abnomality encountered in clinical practice is Atrial Fibrillation (AF). During AF, the atria contract very fast and irregularly. The mechanism of AF is still not fully understood but is thought to involve either multiple wavelets [6] propagating through the atria or focal high frequency re-entrant sources [7]. This results in inefficient quivering of the atria instead of coordinated contraction. Consequently, the atria do not deliver blood into the ventricles effectively. This can result in stagnation of blood in the atria, giving rise to clot formation. A clot can travel into the arterial system and occlude circulation to the brain, resulting in an embolic stroke. Cardiac autonomic ganglia are nervous tissue which can be found on the surface of the heart. They are thought to play an important role in initiation and maintenance of AF [8]. We hypothesize that stimulation of these ganglia will produce changes in the frequency spectrum of AF.

II. METHODS

For this study, we analysed intracardiac electrograms of two patients who were in AF during routine electrophysiology study. All signals were recorded from a decapolar catheter. The decapolar cathter was placed in the coronary sinus allow assessment of left atrial electrical activity. High frequency (HF) electrical stimulation at 20 Hz was delivered from the proximal poles of the coronary sinus catheter to produce slowing of the ventricular heart rate, which is an indication of stimulation of nearby autonomic ganglia. Signals recorded from the distal poles were used for frequency domain analysis.

III. FREQUENCY DOMAIN ANALYSIS

The Fourier transform is a popular technique for digital signal processing. The reason is that it will convert the complicated convolutional function in the time domain to a much simpler multiplication function in the frequency domain [9]. During AF, frequency analysis is widely used to measure changes in the dominant frequency. Welch method is used here to estimate the frequency spectrum of the signals. The Fourier transform was calculated separately for each of the segments. The analysis was performed by taking the average of the segments, each with 2000 points sampled at 1000Hz, using a 4096-point FFT and an overlap of 50% with a hamming window.

Dominant Frequency (DF) is a frequency of the signal when the power spectrum shows the maximum value. The general application of DF analysis is to estimate the atrial activation rates [10]. Researchers who apply spectral techniques show that AF has significant periodic elements with different degrees of regularity. It has also been shown that certain areas of the atria can have higher activation frequencies than other areas. This condition may be drivers that preserve AF and could be targets of ablation therapy [11-17]. DF was obtained from the FFT analysis. In general, all the DF values obtained are within the range of 6.10 – 6.84 Hz and this is in agreement with the results obtained by Ropella[18].

IV. RESULTS

The AF data have been analysed and spectra were produced for these two patients. The average spectrum and the spectrograms obtained from the first patient are shown in Figure 1.

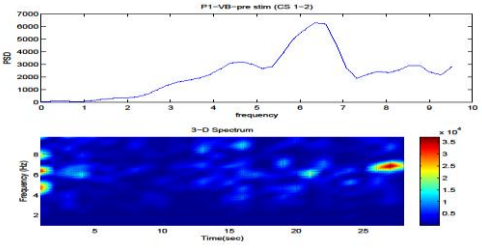

(a)

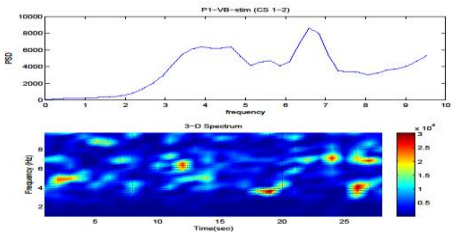

(b)

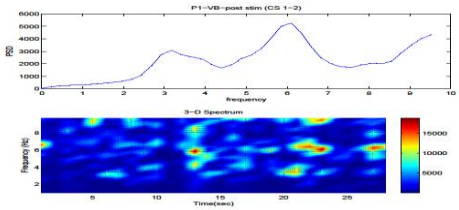

(c)

Figure 1: Power spectrum and 3D spectrogram for patient 1, (a) pre-HF stimulation (b) During HF stimulation and (c) post-HF stimulation

The DF has been recorded at coronary sinus (CS1-2) for pre-HF stimulation, during HF stimulation and post-HF stimulation. The frequencies from coronary sinus positions for patient 1 and patient 2 are shown in Table 1.

TABLE 1
DOMINANT FREQUENCY FOR PATIENT 1 AND 2

Conditions	DF (CS1-2), Hz	
	Patient 1	Patient 2
Pre-HF stimulation	6.35	6.59
During HF Stimulation	6.59	6.84
Post-HF stimulation	6.10	6.10

DF at Pre-HF Stimulation for patient 1 is 6.35 Hz and 6.59 Hz for patient 2. 3D diagram confirmed the situation based on the colour-coded spectrogram observed. There are increasing trends of DF (6.59 Hz for patient 1 and 6.84 Hz for patient 2) during stimulation stage observed for this channel comparatively to Pre-stimulation. The values of all DF for post stimulation are lower than that of pre-stimulation DF which is 6.10 Hz (for both patients).

From most human studies, the dominant frequency in AF is between 4 Hz to 10 Hz [17-18]. It is more commonly around 6 Hz to 7 Hz. An increase in the DF during HF stimulation suggests that the autonomic ganglia can influence the rate of atrial depolarization during AF, possibly by altering electrophysiological properties of the atria (e.g. shortening tissue refractory period).

V. CONCLUSION

As of this stage, using frequency domain analysis, the 3D frequency strength plotting is achieved. The plotted diagram allows us to identify the evolution of the frequency composition of the signal along time. We have shown that the DF of AF can be influenced by stimulation of autonomic ganglia, suggesting a possible role in the maintenance of AF and hence supporting the idea that these ganglia should be targets for ablation in the treatment of AF.

REFERENCES

[1] Ghanem, R.N., Ramanathan, C., Ping Jia, Rudy, Y., Heart-surface Reconstruction and ECG Electrodes Localization using Fluoroscopy, Epipolar Geometry and StereoVision: Application to Noninvasive Imaging of Cardiac Electrical Activity, IEEE Transactions on Medical Imaging, Volume 22, 2003:1307 – 1318.

[2] Kopecky Sl, Gersh Bj, Mcgoon Md, *et al*. The Natural History of Lone Atrial Fibrillation: A Population-based Study over Three Decades. N. Engl. J. Med. 1987; 317:669-674.

[3] Prystowsky En., Benson Dw. Jr, Fuster V, *et al*. Management of Patients with Atrial Fibrillation: A Statement for Healthcare Professionals: From the Subcommittee on Electrocardiography and Electrophysiology, American Heart Association. Circulation 1996, 93:1262-1277.

[4] Wellens Hjj., Atrial fibrillation: The Last Big Hurdle in Treating Supraventricular Tachycardia. N Engl J Med 1994; 331:944-945.

[5] Jose Jalifea, Omer Berenfelda, Moussa Mansourb, Mother Rotors and Fibrillatory Conduction: A Mechanism of Atrial Fibrillation, Cardiovascular Research 54, 2002, 204–216.

[6] Moe GK, Abildskov JA. Atrial Fibrillation as a Self-sustaining Arrhythmia Independent of Focal Discharge, American Heart Journal 1959; 58:59-70.

[7] Jalife J, Berenfeld O, Skanes A, Mandapati R. Mechanisms of Atrial Fibrillation: Mother Rotors or Multiple Daughter Wavelets, or both? J. Cardiovasc. Electrophysiol. 1998; 9:S2-12.

[8] Scherlag BJ, Nakagawa H, Jackman WM, Yamanashi WS, Patterson E, Po S, Lazzara R. Electrical Stimulation to Identify Neural Elements on the Heart: Their Role in Atrial fibrillation. J. Interv. Card. Electrophysiol. 2005; 13 Suppl 1:37-42.

[9] Roman Kuc, Introduction to Digital Signal Processing, McGraw-Hill International Editions. 1988.

[10] Jason Ng, Jeffrey J.Goldberger, Understanding And Interpreting Dominant Frequency Analysis Of AF Electrograms, J Cardiovasc Electrophysiol. 2007; 18(6):680-685.

[11] Skanes Ac, Mandapati R, Berenfeld O, Davidenko Jm, Jalife J: Spatiotemporal Periodicity during Atrial Fibrillation in the Isolated Sheep Heart. Circulation 1998; 98:1236-1248.

[12] Mansour M, Mandapati R, Berenfeld O, Chen J, Samie Fh, Jalife J: Left-To-Right Gradient Of Atrial Frequencies During Acute Atrial Fibrillation In The Isolated Sheep Heart. Circulation 2001; 103:2631-2636.

[13] Lazar S., Dixit S, Marchlinski Fe, Callans Dj, Gerstenfeld Ep: Presence Of Left-To-Right Atrial Frequency Gradient In Paroxysmal But Not Persistent Atrial Fibrillation In Humans. Circulation 2004; 110:3181-3186.

[14] Sahadevan J, Ryu K, Peltz L, Khrestian Cm, Stewart Rw, Markowitz Ah, Waldo Al: Epicardial Mapping of Chronic Atrial Fibrillation in Patients: Preliminary bservations. Circulation 2004; 110:3293-3299.

[15] Lin Yj, Tai Ct, Kao T, Tso Hw, Higa S, Tsao Hm, Chang Sl, Hsieh Mh, Chen Sa: Frequency Analysis in Different Types of Paroxysmal Atrial Fibrillation. J. Am. Coll. Cardiol. 2006; 47:1401-1407.

[16] Pachon Jc, Pachon Ei, Pachon Jc, Lobo Tj, Pachon Mz, Vargas Rna, Pachon Dqv, Lopez Mfj, Jatene Ad: A New Treatment for Atrial Fibrillation based on Spectral Analysis to Guide the Catheter RF-Ablation. EUROPACE 2004; 6:590-601.

[17] Sanders P, Berenfeld O, Hocini M, Jais P, Vaidyanathan R, Hsu L.F., Garrigue S, Takahashi Y, Rotter M, Sacher F, Scavee C, Ploutz-Snyder R, Jalife J, Haissaguerre M: Spectral Analysis Identifies Sites of High-frequency Activity Maintaining Atrial Fibrillation in Humans. Circulation 2005; 112:789-797.

[18] K.M Ropella, A.V Sahakian, J.M Baerman and S Swiryn, Effects of Procainamide on Intra-atrial Electrograms during Atrial Fibrillation: Implications for Detection Algorithms, Circulation 1988 Jun; 77(6):1344.

TEST CHIP FOR EVALUATING THE PACKAGING TECHNIQUES FOR BIOMEDICAL IMPLANTABLE DEVICES

N. Saeidi[1,2], J. Alderman[2], A. Demosthenous[1], N. Donaldson[1]
[1]UCL, University College London, UK
[2]Tyndall National Institute, Ireland

nsaeidi@ee.ucl.ac.uk,

Abstract – In this paper we briefly report on the development of a set of test chips that can be used to verify the sealing techniques with biomedical implants as their target application. These test chips have been designed and fabricated based on the Tyndall's in-house CMOS 1.5 micron technology. Each chip includes humidity, temperature and/or corrosion sensors. Different designs and sizes have been considered for these sensors to compare the sensors sensitivity and to select the optimum ones for the final chip. The sensors are being tested and the result obtained for one of the humidity sensors is presented.

I. INTRODUCTION

Packaging of biomedical devices is very crucial due to strict requirements posed by their target applications and differs significantly from those of conventional ICs. The performance of a biomedical device is highly depended on the reliability and quality of the packaging. Also, more challenges emerge when the size of the device decreases drastically or the device is intended to work in human body for decades [1, 2].

To verify a packaging technology which has been chosen or developed for biomedical devices, a certain mechanism is required to validate the performance of the technology. In this paper, we report design and fabrication of a series of test chips, consisting humidity sensors and corrosion detectors which will be used to evaluate the packaging technology for miniaturized biomedical implantable devices. These sensors are able to monitor moisture and corrosion levels inside the package Thus they can be used to evaluate the reliability and the performance of a packaging technology which is being developed for implantable devices.

Three test chips have been designed consisting of a number of humidity, corrosion and temperature sensors. Corrosion detectors measure the change in the resistance of the structures due to moisture penetration and the temperature sensors can be used for monitoring the device temperature. These sensors are single metal layer structures while humidity sensors are single metal layer capacitive structures covered by a layer of plain or porous polyimide. Also, structures with different line widths and line gaps have been designed to evaluate the effect of these factors on the accuracy and stability of the sensors.

II. FABRICATION

Testchip4 was designed based on three individual layouts each of which consists of various sensors to measure humidity, temperature and corrosion.

Overall size of each layout is 6 mm × 4.4 mm and three wafers were used for fabrication of the test chip. Figure 1 shows the arrangement of the layouts in the mask design. All the sensors in Testchip4 were designed based on single metal layer structures. To simplify the process and reduce the steps, for the first wafer only metal deposition and patterning steps were performed, while for the other two wafers, a layer of polyimide was also deposited which acts as a dielectric layer for the humidity sensors. Table 1 summarizes the list of Testchip4 sensors .

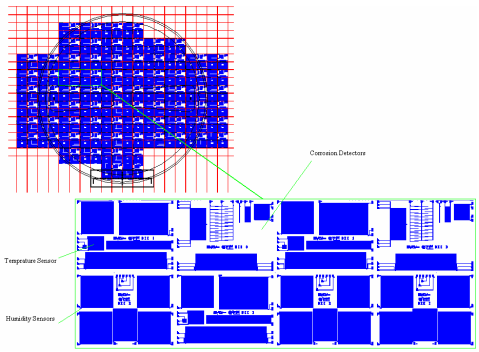

Figure 1. Testchip4 layouts

III. EXPERIMENTAL

In order to facilitate characterization of the fabricated sensors, some of the dies were wire bonded into 24-pin ceramic packages. The test setup for characterizing the structures consists of a climatic test chamber (Heraeus Votsch HC7033), a multimeter (Agilent 34410A) and a LCR meter (Agilent E4980A). The test chips were put into the climatic test chamber which provides a controlled environment for the experiments. As corrosion is a long term process the experiments for corrosion detectors are still in progress. However, the following section discusses the results obtained for one of the humidity sensors.

TABLE I
LIST OF THE FABRICATED SENSORS

Name	Description
HS-1u	Humidity Sensor (without openings)
TS1	Temperature Sensor
CR-1u	Interdigitated Corrosion Sensor
LD-1u	Ladder Corrosion Sensor
TT-1u	Triple-Track Corrosion Sensor
SP1	Spiral Corrosion Sensor
HS-3u-p	Humidity Sensor (4µm openings)
HS-3u-cover	Humidity Sensor (without openings)
HS-3u-holes	Humidity Sensor (2µm openings)
Edge-SP1	Spiral Corrosion Sensor
Edge-SP2	Spiral Corrosion Sensor
Edge-SP3	Spiral Corrosion Sensor
TripleTrack-5u	Triple-Track Corrosion Sensor
TripleTrack1	Triple-Track Corrosion Sensor
Ladder1	Ladder Corrosion Sensor
Ladder3	Ladder Corrosion Sensor
Corrosion1	Interdigitated Corrosion Sensor
Comb2	Comb Like Corrosion Sensor

A. HS-3u-p: Humidity Sensor Characterisation

The sensitivity and response time of a capacitive humidity sensor can be improved by changing the shape and dimensions of the moisture sensing layer or the electrodes [3-5]. The humidity sensors designed for these test chips are all single layer interdigitated fingers covered by a thin layer of polyimide. The humidity sensors of the test chips only differ in electrode widths, gaps and the openings in the polyimide layer.

HS-3u-p is a humidity sensor in this test chip with the overall size of 2 mm × 2 mm. The electrode width is 3 µm and the gap between two adjacent electrodes is 8 µm. To increase the surface which is in contact with the outside environment, a 4 µm width rectangular opening was made in the polyimide layer between each pair of adjacent electrodes. Figure 2 shows a three dimensional model of this sensor.

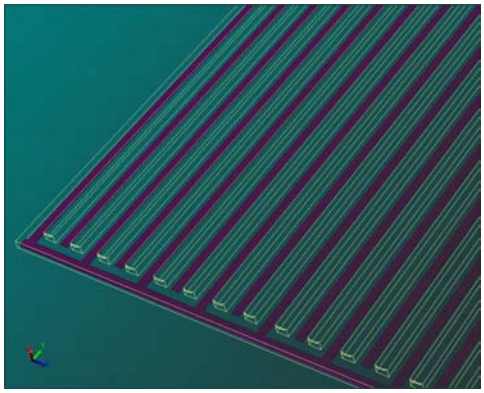

Figure 2: HS-3u-p Humidity Sensor

To investigate the sensor response, a series of experiments were carried out. Figure 3 shows the result obtained from one of these experiments, with the temperature fixed at 37 ºC and the humidity typically ramped up and down between 55 to 85 %RH.

As shown in Figure 3, when the humidity is increased by 30%, the capacitance of the sensor changes from 22.5 pF to 42.5 pF

The sensitivity HS-3u-p is calculated by equation (1)

$$S = \frac{\Delta C}{\Delta RH} \qquad (1)$$

where ΔC is the change in the capacitance of the sensor and ΔRH is the change of the relative humidity; therefore sensitivity of this sensor is 0.67 pF per % RH.

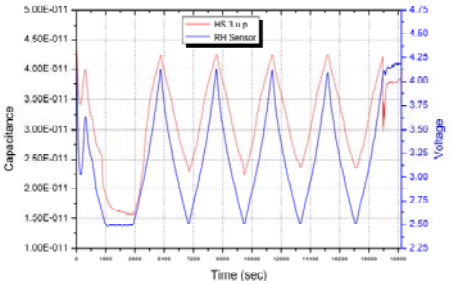

Figure 3 HS-3u-p response

IV. CONCLUSION

A set of test chip consisting of a number of humidity, temperature and corrosion sensors has been designed and fabricated. The results obtained from experiments show a high sensitive humidity sensor that can measure the level of moisture inside the package of biomedical implants.

REFERENCES

[1] R. A. M. Receveur, F. W. Lindemans, and N. F. de Rooij, "Microsystem technologies for implantable applications," *Journal of Micromechanics and Microengineering,* vol. 17, pp. R50-R80, May 2007.

[2] K. Najafi, "Packaging of implantable microsystems," *2007 Ieee Sensors, Vols 1-3,* pp. 58-63, 2007.

[3] J. Laconte, V. Wilmart, J. P. Raskin, and D. Flandre, "Capacitive humidity sensor using a polyimide sensing film," in *Symposium on Design, Test, Integratives and Packaging of MEMS/MOEMS*, Cannes, FRANCE, 2003, pp. 223-228.

[4] U. Kang and K. D. Wise, "A high-speed capacitive humidity sensor with on-chip thermal reset," *IEEE Transactions on Electron Devices,* vol. 47, pp. 702 - 710, 2000.

[5] H. H. Zeng, Z. Zhao, H. F. Dong, Z. Fang, and P. Guo, "Fabrication and test of MEMS/NEMS based polyimide integrated humidity, temperature and pressure," *2006 1st IEEE International Conference on Nano/Micro Engineered and Molecular Systems, Vols 1-3,* pp. 788-791, 2006.

A VIRTUAL REALITY WHEELCHAIR DRIVING SIMULATOR FOR USE WITH A BRAIN-COMPUTER INTERFACE

Bartłomiej Grychtol, Heba Lakany, Bernard A. Conway

Department of Bioengineering, University of Strathclyde, Glasgow, UK

bartlomiej.grychtol@strath.ac.uk

***Abstract*—For patients with extensive paralysis, autonomous control of an electric powered wheelchair (EPW) is very difficult. Recent developments in brain-computer interfaces (BCI) suggest that BCI systems could provide an effective strategy for wheelchair control. Our goal is to build a BCI-controlled EPW to provide paralysed subjects with a means of autonomous mobility. This requires a safe testbed on which trials and user training are conducted. This paper presents an extendible virtual environment simulator of an EPW to fulfil that purpose. It combines the features of simulators used in robotics with those built for training and evaluation of prospective wheelchair users.**

I. INTRODUCTION

In recent years, virtual reality (VR) has attracted much interest in the field of motor rehabilitation engineering [1]. VR has been used to provide safe and interesting training scenarios with near-realism environments for subjects to interact with, e.g. [2]. The performance of subjects within these virtual environments (VE) proved to be representative of the subjects' abilities in the real world and their real-world skills showed significant improvements following the VR training [3]-[5].

To date, VR electric powered wheelchair (EPW) simulators were mainly developed to either facilitate patient training and skill assessment [6][7] or assist in testing and development of semi-autonomous "smart" wheelchairs [8]. While in the training simulators the focus is on user interaction and immersion, the main objective of the robotics simulators is the accurate simulation of physical behaviour and various sensors.

The simulator presented here addresses the need to combine these approaches. It is an inexpensive design that provides the degree of immersion required for user training while supporting a number of sensors and ensuring physically plausible simulation as required for development of smart wheelchairs.

The simulator is a part of a larger project where we aim to use our experience in detecting and classifying wrist movement intention from the EEG signals [9] to develop a brain computer interface (BCI) to assist tetraplegic spinal cord injured (SCI) patients to control their wheelchairs.

II. DEVELOPING AN IMMERSIVE WHEELCHAIR SIMULATOR

A. Hardware

To provide a sense of immersion, the VE is projected on a spherical screen (section of a sphere with 1.5m radius) providing a 160° horizontal field of vision (FOV) using a projector fitted with a wide-angle lens (Elumens VisionStation®). Considering alternative immersive displays, we have excluded the use of head-mounted displays due to their high cost, patient preference [4], and possible interference with the BCI. Equally, we have excluded the use of multi-projector systems due to both their high cost and difficult maintenance.

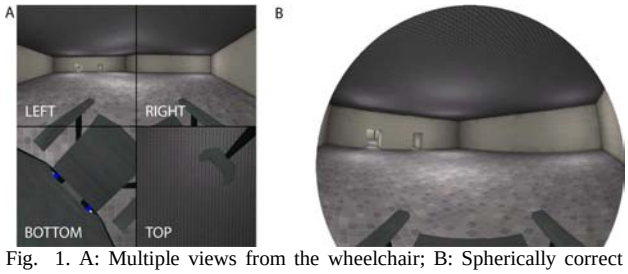

Fig. 1. A: Multiple views from the wheelchair; B: Spherically correct image ready for projection on the dome.

Fig. 2. Invacare SpectraPlus (left) and its model rendered in UT2004 (right).

The simulator runs on a dual-core PC with a gaming-standard dual-view graphics card. The system also includes a joystick (Traxsys Joystick Plus) similar to those used on wheelchairs. Other supported input devices include keyboard, mouse, mouse replacement devices and gaming joysticks.

B. Software

The simulator relies on the Unreal Engine 2.5 and the Karma physics engine – both integral to the Unreal Tournament 2004 (UT2004) game – to, respectively, maintain and render the virtual environment and model the physical behaviour of its elements. This approach was developed by the Urban Search and Rescue Simulator (USARSim) [10] open-source community. Importantly, UT2004 operates as a server, allowing physical separation of the simulator and any BCI-related hardware.

Correct immersive 3D display on the VisionStation is ensured by the SPIClops OpenGL—based API provided by the manufacturer, which requires four orthogonal views of a scene to stitch into a single frame (Fig. 1). The average frame rate is above 30 FPS at a resolution of 1024x768 pixels.

A GUI application has been developed in VisualC++ that integrates UT2004, USARSim and SPIClops. This allows the choice of map, vehicle and method of control. All communication between the application (client) and the game server, including periodic status information about the wheelchair's position and velocity, is recorded for offline analysis of users' performance.

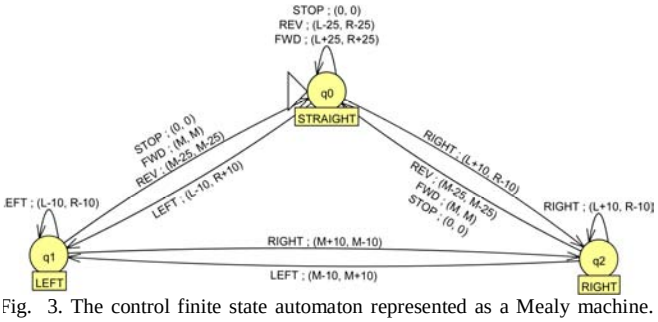

Fig. 3. The control finite state automaton represented as a Mealy machine. Arrows represent transitions between states (q0, q1,q2) and are annotated with the causing action (LEFT, RIGHT, FWD, REV or STOP) and the resultant output – a pair of normalized (-50 to 100) angular velocities of the two wheels (L and R). M = (L+R)/2. Not captured by the diagram are the constraints: $|L - R| \leq 40$, $-50 \leq L \leq 100$, and $-50 \leq R \leq 100$.

III. Wheelchair Model

The simulator features a simplified 3D model of the Invacare SpectraPlus wheelchair (see Fig. 2). The model was built in Maya 7.0 PLE based on images available from the manufacturer's website[1]. The model features fully autonomous castor wheels, a functional curb climber and four orthogonal simulated cameras. For correct physical simulation, mass-inertial properties of an occupied wheelchair were calculated using estimated masses of the different parts of the chair and literature values for average human body parameters [11][12].

IV. Control Method for BCI

Conventionally, EPWs are controlled with a joystick whose deflection is translated to two voltage signals controlling the motors. This sort of analogue control, however, is not currently feasible with BCIs, which can only generate discreet commands. A simple solution is to assign each command a fixed velocity or amount of turning, but this would lead to a very unnatural control, broken path and difficult manoeuvring. To allow for smooth path control, an alternative control mechanism was developed using a finite state automaton (Fig. 3). Using just five commands, control states equivalent to 35 different joystick positions can be achieved. With this type of control, smooth paths with varying curvature can be obtained, as demonstrated by a sample trace in Fig. 4.

V. Conclusion

The VR wheelchair simulator presented here addresses an important gap in wheelchair simulation in that it can be used for both patient training or evaluation and design and development of semi-autonomous wheelchairs.

Due to its flexibility and the long (and expanding) list of sensors inherited from the USARSim project, the current system provides a perfect testbed for development and testing of smart wheelchair systems. This was not possible with USARSim alone.

Given that the system is functional even without an immersive display system, its relatively low hardware requirements make it an easy to deploy, low-cost solution for the current lack of structured training schemes for future EPW users. In addition, the VE can later be used to simulate the subject's residence, for example, which may help in identifying their needs for re-designing or altering their accommodation to suit their EPW driving abilities and acquired skills.

[1] http://invacare.co.uk/

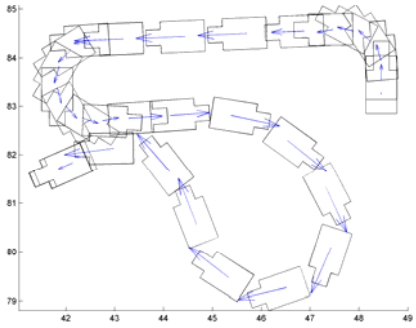

Fig. 4. Sample trace of a path taken by the simulated wheelchair in an empty space using the finite state machine control with keyboard input. Axes represent position in meters. Vectors represent velocity.

The present simulator has two major limitations. First, due to our desire to provide a plug-and-play system for wheelchair users, no motion simulation is provided. Second, nothing is projected on the floor or around the wheelchair – areas that demand most attention when manoeuvring in tight passages. This could be addressed by using a head-mounted display, but, as stated before, this would interfere with the EEG cap required for the BCI.

Acknowledgements

This work is supported by the EPSRC Doctoral Training Center in Medical Devices and the Glasgow Research Partnership in Engineering.

References

[1] M. K. Holden, "Virtual environments for motor rehabilitation: review," Cyberpsychol Behav, vol. 8, nr. 3, pp.187–211, June 2005.
[2] R. F. Boian, G. C. Burdea, J. E. Deutsch, and S.H Windter, "Street crossing using a virtual environment mobility simulator," in Proceedings of IWVR, Lausanne, Switzerland, 2004.
[3] D. P. Inman, K. Loge, and J. Leavens, "VR education and rehabilitation," Commun ACM, vol. 40, nr. 8, pp.53–58, 1997.
[4] A. Harrison, G. Derwent, A. Enticknap, F. D. Rose and E.A. Attree, "The role of virtual reality technology in the assessment and training of inexperienced powered wheelchair users," Disabil Rehabil, vol. 24, nr. 8, pp. 599-606, July 2002.
[5] I. A. Adelola, S. L. Cox, and A. Rahman. "VEMS – training wheelchair drivers," in Assistive Technology, vol. 16, IOS Press, pp. 757-761, 2005.
[6] M. Desbonnet, S. L Cox, and A. Rahman, "Development and evaluation of a virtual reality based training system for disabled children," in P. Sharkey, R. Sharkeand and J.-I. Lindström (eds), The Second European Conference on Disability, Virtual Reality and Associated Technologies, Mount Billingen, Skvde, Sweden, pp. 177-182, September 1998.
[7] H. Niniss and T. Inoue, "Electric wheelchair simulator for rehabilitation of persons with motor disability," in Symposium on Virtual Reality VIII (Proceedings), Belém (PA), 2006. Brazilian Computer Society (BSC).
[8] T. Röfer, "Strategies for using a simulation in the development of the Bremen autonomous aheelchair," in Simulation: Past, Present and Future, 12th European Simulation Multiconference 1998, ESM'98, Manchester, UK, pp. 460-464, 1998.
[9] G. Valsan, P. Worrajiran, H. Lakany, and B.A. Conway, "Predicting intention and direction of wrist movement from EEG," Advances in Medical, Signal and Information Processing, IET 3rd International Conference On, MEDSIP 2006, pp 1-4, July 2006.
[10] J. Wang and S. Balakirsky, "USARSim Manual V3.1.1", 2007.
[11] P. de Leva "Adjustments to Zatsiorsky-Seluyanov's segment inertia parameters," J Biomech, vol. 29, nr. 9, pp. 1223-1230, September 1996.
[12] R. Drillis and R. Contini, "Body segment parameters," Technical Report 1166-03, Office of Vocational Rehabilitation, New York, 1966.